Light Yield in Liquid Argon for Dark Matter Detection

Dissertation

zur

Erlangung der naturwissenschaftlichen Doktorwürde
(Dr. sc. nat.)

vorgelegt der

Mathematisch-naturwissenschaftlichen Fakultät

der

Universität Zürich

von

CREUS William

aus Frankreich

Promotionskomitee

Prof. Dr. Claude Amsler (Vorsitz)
Dr. Alfredo Ferella

Zürich, 2013

Contents

Zusammenfassung

Aus einer Vielfalt von experimentellen Beobachtungen findet man, dass ein Grossteil der Masse unseres Universums nicht aus Baryonen besteht, sondern aus “dunkler Materie” , die an Photonen nicht koppelt. Die prominentesten Kandidaten für dunkle Materie sind die schwach wechselwirkenden massiven Teilchen (die sogenannten WIMPs). Diese Teilchen müssen mehrere Anforderungen erfüllen: sie müssen elektrisch neutral und auf kosmologischen Zeitskalen stabil sein, und müssen die richtige Reliktdichte besitzen.

Während des letzten Jahrzehnts haben mehrere Experimente mit verschiedenen technischen Methoden nach dunkler Materie gesucht. Eines dieser Verfahren beruht auf dem direkten Nachweis der elastischen Stösse zwischen WIMPs und der gewöhnlichen Materie. Aufgrund des geringen Wirkungsquerschnitts müssen grosse Detektoren gebaut werden, die eine gute Diskriminierung zwischen Signal und Untergrund aufweisen. Die empfindlichsten Messungen der Spin-unabhängigen WIMP-Nukleon Wechselwirkung, die gegenwärtig die beste obere Grenze f"ur die Existenz von WIMPs liefern, wurden vom XENON-100 Experiment durchgeführt (2×10^{-45} cm^2 für WIMP-Massen im Bereich von 55 GeV/c^2).

Edelfüssigkeiten wie Argon und Xenon werden häufig für direkte Suchen nach dunkler Materie verwendet, da sie gute Szintillationseigenschaft, eine relativ niedrige Ionisierungsenergie haben, und selber als Abschirmung gegen den externen Untergrund eingesetzt werden können. Time Projection Chambers (TPC) messen mit flüssigem Argon oder Xenon als Target- und Nachweismedien gleichzeitig Licht und Ladung, sodass eine saubere Trennung zwischen Kernrückstössen aus WIMPs und Untergrund-Elektronen möglich ist. Der Wechselwirkungspunkt kann beobachtet werden und somit können Mehrfachstreuungen von Untergrund-Neutronen unterdrückt werden. Zudem kann im flüssigem Argon (LAr) die Pulsform des Szintillationslichtes für die Identifizierung von Kernrückstössen ausgenutzt werden, was zu einer noch besseren Unterdrückung des Untergrundes führt.

In diesem Zusammenhang ist eine Messung der Szintillationseffizienz von Argon unabdingbar. Damit wird die Energieskala bestimmt und die Nachweiswahrscheinlichkeit kann bei niedrigen Energien ermittelt werden. Die relative Szintillationseffizienz wird als Verhältnis der Szintillationsausbeuten durch Kernrückstösse zu der durch Compton-Elektronen induzierten Ausbeute definiert. Die Effizienz für Compton-Elektronen wird mit Hilfe einer γ-Referenzquelle gemessen. Das Ziel dieser Arbeit war, die erwartete Lichtausbeute von WIMP-induzierten Kernrückstössen bei tiefen Energien zu messen, im Hinblick auf zukünftige grosse Einrichtungen wie DARWIN. Da die WIMP-Argon-Streuung mit Neutronen simuliert werden kann, wurde die von Argonkernen erzeugte Lichtausbeute im LAr mit einem monoenergetischen Neutronengenerator gemessen (und zwar ohne elektrisches Driftfeld). Ich beschreibe in dieser Arbeit den Bau der Einrichtung, die Eichungen, das Studium der Lichtpulse und der Szintillationsausbeute, die zu einem besseren Verständnis des Szintillationsmechanismus in LAr führt, sowie die Messung der relativen Szintillationseffizienz. Die Szintillationseffizienz wurde für Kernrück-

stossenergien zwischen ∼7 keV und ∼120 keV ermittelt. Sie bleibt oberhalb von 16 keV konstant und wächst langsam bei niedrigen Energien. Dies führt zu einer Erhöhung der Nachweiswahrscheinlichkeit von WIMPs im flüssigen Argon in diesem Energiebereich.

Abstract

A wide variety observations states evidences of non-baryonic particles, called dark matter, which do not couple to photons and provide most of the mass of our universe. The most prominent dark matter candidates are the so called Weakly Interacting Massive Particles (WIMPs). Such particles have to fulfill several requirements, they have to be electrically neutral, stable on cosmological time scales and must have the right relic density.

During the last decade several attempts to detect dark matter have been realized employing different techniques. One of these methods is the direct detection based on the elastic collision between WIMPs and ordinary matter. Due to its small cross section, detectors should have a large target mass and a good discrimination background capability for successful WIMP detection. The most stringent limit on the spin-independent WIMP-nucleon interaction cross section is set by XENON 100 at 2×10^{-45} cm^2 for a WIMP mass of 55 GeV/c^2.

Noble liquids such as argon and xenon are commonly used for direct dark matter searches, providing a good scintillation property, a relatively low ionization energy and the advantage to be self-shielding against external backgrounds. Time Projection Chambers (TPCs) using liquefied noble gas as a detection medium measures simultaneously light and charge, thus allowing a background discrimination between nuclear recoils induced by WIMPs and electron recoils and the localization in 3D of the interactions for the rejection of neutrons from multiple scatterings. Moreover, in liquid argon (LAr) the pulse shape of the scintillation light can be exploited as an additional discrimination for the identification of nuclear recoils, leading to a better background rejection.

In this context the measurement of relative scintillation efficiency, defined as the ratio of the scintillation yield of nuclear recoils to that of electronic recoils from a reference γ source, is important to determine the nuclear energy scale and to quantify the WIMP detection sensitivity at low energies. The purpose of this work is to study the response of nuclear recoils induced by WIMPs for the design of future large facilities, such as DARWIN. The light yield produced by recoiling argon nuclei has been studied at zero electric field, using a monoenergetic neutron generator to mimic the scattering of WIMPs in liquid argon. I describe in this thesis the assembly of the setup, calibrations and measurements of light pulse shape and scintillation yield required for a better comprehension of the scintillation in LAr and for the determination of the relative scintillation efficiency. The relative scintillation efficiency of nuclear recoils has been measured between $\sim$7 keV and $\sim$120 keV and is found to be constant above 16 keV, slowly rising towards low energies leading to an increase of the WIMP detection sensitivity at this energy range.

Chapter 1

Dark Matter

Mankind has always been fascinated by the origin of the universe. Indeed, despite the great scientific innovation and a wide variety of experimental observations which have changed our understanding of the universe, its content remains a mystery. Only 5% of the mass of the universe is known to be the ordinary baryonic matter described by the current standard model. Most of the content of the universe is under the form of vacuum energy, called dark energy responsible for the acceleration of the expansion of the universe, and in the form of invisible matter called dark matter.

In this chapter, I will present various pieces of evidence supporting the existence of dark matter before setting out briefly some possible candidate particles, the different techniques used and the current status for direct detection dark matter searches.

1.1 Evidences for Dark Matter

"Dark" matter was first inferred from the observation of gravitational effects that the "visible" matter could not explain. This observation led the scientific community to put forward two options allowing to describe the anomalous dynamic of astrophysical objects: either the gravitational law described by the general relativity is incomplete and the Newtonian dynamics have to be modified (MOND theory [1]) or the existence of a hypothetical particle called dark matter which has the particularity to be electrically neutral since it has no electromagnetic interaction. The following sections will present the evidences for dark matter at different scales in the universe.

1.1.1 Rotational curves of galaxies

The observation of the rotation curve of a spiral galaxy prevails probably as the most obvious proof of the existence of dark matter. In 1970 Rubin realized that the circular velocity of stars remained constant after a certain distance from the galaxy center [2]. According to Eq. 1.1

$$v(r) = \sqrt{\frac{GM(r)}{r}} \quad , \tag{1.1}$$

Newtonian dynamics stipulates that the circular velocity v of a body located at a distance r from the galaxy center with a total mass $M(r)$ goes to $v(r) \propto r^{-1/2}$ where G is Newton's gravitational constant. The evaluation of the circular velocity vs. the radius of a galaxy can be obtained by measuring the redshift of the 21 cm emission of neutral hydrogen. The neutral hydrogen cloud allows a measurement of the circular velocity further beyond than the stars themselves since it extends farther beyond the visible disk of stars. Fig. 1.1 displays a measurement of the rotation curve as a function of radial distance from galactic center for a typical spiral galaxy (NGC 6503). The observed circular velocity increases from the galaxy center up to a radius of 5 kpc. Above this distance the rotation curve shows rather a flat behavior. Using the Eq. 1.1 the expected contribution of the baryonic component – which consists of interstellar gas (gas) and stellar disk (disk) – to the rotational velocity can not alone explain the measured galactic rotation curve. This discrepancy implies an additional contribution from a non luminescence dark matter halo such as $M(r) \propto r$ to keep the circular velocity constant.

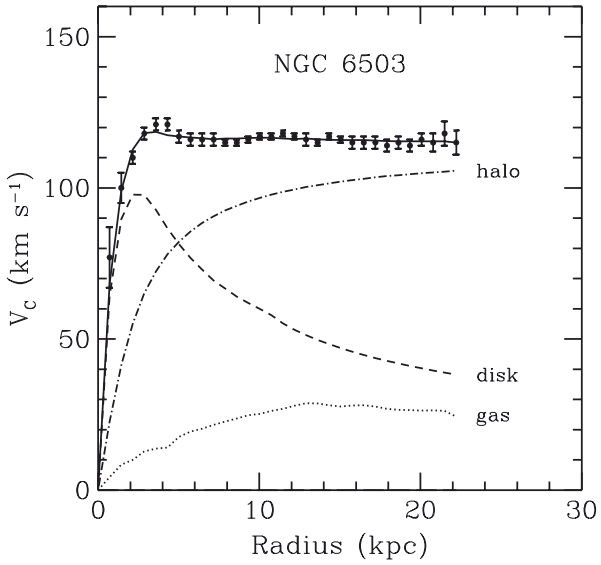

Figure 1.1: Rotation velocity as a function of radius for galaxy NGC6503, showing the expected contribution from the disk and gas. The additional contribution of the dark matter ("halo") is also shown to explain the observed velocity distribution [3].

1.1.2 Galaxy clusters

The first astrophysical evidence supporting the presence of dark matter was found in 1933 by the Swiss astronomer Fritz Zwicky [5]. While observing the velocity dispersion of galaxies in the Coma cluster Zwicky applied the virial theorem Eq. 1.2

$$2\langle T \rangle = -\langle V_{tot} \rangle \quad , \tag{1.2}$$

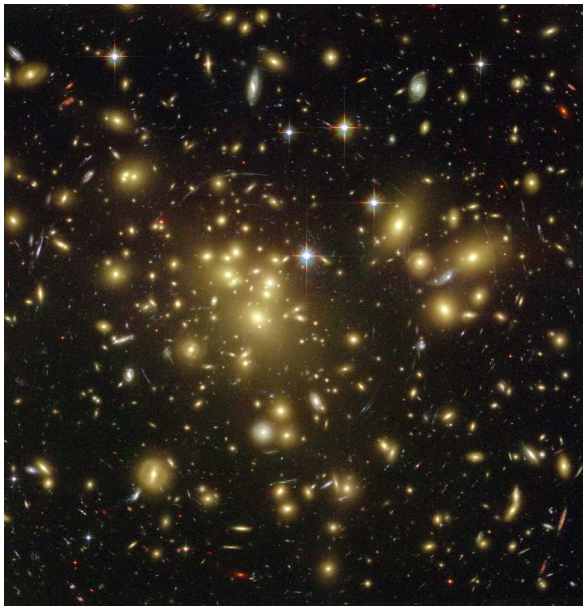

Figure 1.2: Galaxy Cluster Abell 1689. Picture taken from [4].

relating the average of kinetic energy $\langle T \rangle$ to its total gravitational potential energy $\langle V_{tot} \rangle$, and noticed that the calculated mass was much greater that the one expected from the observable luminosity. Actually the mass-to-light ratio was 2 orders of magnitude higher than the ratio of the solar neighborhood. This discrepancy therefore indicated the presence of a large amount of invisible mass halo.

Gravitational lensing is an effect predicted by Einstein's general relativity observed in 1970 by the discovery of multiple images of quasar 0957+561 [6]. This effect occurs when the light emitted from a distant astrophysical object is bent by a massive object situated between the light source and the observer. The space around the lensing object is curved because of the large gravitation potential, so that the direction of the light follows the geodesics and not the straight path before reaching different positions on the earth, creating arcs and a series of warped images or even multiple images of the same structure. Fig. 1.2 shows the dramatic example of Abell 1689. This picture was taken by Hubble Space Telescope via the Advanced Camera for Surveys (ACS) [4]. Its exceptional angular resolution allowed to identify around one hundred arcs and thirty multiple images of this large galaxy cluster.

The mass distribution of such a massive object can be obtained independently of the dynamics through the geometrical distortion. Fig. 1.3 illustrates the reconstructed distribution of matter of the galaxy cluster CL 0024+1654 [7]: here, the most dominant component of the cluster mass is the dark matter distributed smoothly while the spikes represent the individual galaxies.

Another evidence supporting the existence of dark matter comes from the observation of

the collision between two galaxy clusters as shown in Fig. 1.4 from the Bullet Cluster [8]. The extent of the cluster plasma, indicated in pink, is obtained from Chandra telescope by measuring the X-Ray emission and the mass distribution, corresponding to the blue area, which is determined using the weak lensing effects. A clear separation is observed between the hot baryon (pink) and the great majority of the matter (blue). The visible galaxy cluster is also separated from the plasma and is located towards the lensing mass. The separation results from the interaction between the intracluster plasma which are decelerated. Whereas most of the matter, which is non-baryonic matter, passes through each other during the collision without interacting.

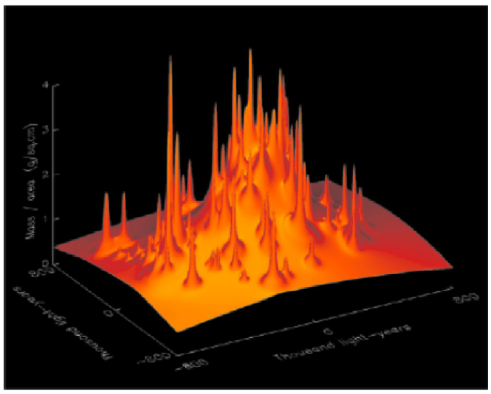

Figure 1.3: Reconstruction of the mass profile of the galaxy cluster CL 0024+1654 showing the individual galaxies represented by spikes, while the dark matter component extends between the galaxies [7].

Figure 1.4: Picture taken from the Bullet Cluster showing an example of colliding clusters. The distribution of dark matter is shown in blue while, the hot gas (intracluster plasma) is represented in pink [8].

1.1.3 Cosmological Scales

Other techniques, based on studies at the cosmological scale, permit to represent accurately the content of the universe, unlike previous methods. The cosmology is the study of the evolution of the structure and of the natural laws that govern the universe at its largest scale. The description of the universe is based on general relativity, which has changed all our understanding of it and allowed us to treat the fundamental interaction of gravity as a geometrical concept in which space and time are related. The current standard cosmological model of the universe, denoted by ΛCMD, describes a flat universe which is permanently expanding and cooling.

In cosmology, the different components of the content of the universe are defined in terms of the ratio of the relative actual densities to the critical density:

$$\Omega_i = \frac{\rho_i}{\rho_c} \quad . \tag{1.3}$$

The sum of the different densities Ω_i represents the total density of the universe. Recently Planck experiment published its first measurement of anisotropies in the cosmic microwave background (CMB) [9], demonstrating that the shared contribution of the total density of the universe is $\Omega_\Lambda = 68.3\%$ for dark energy density, $\Omega_{DM} = 26.8\%$ for non-baryonic matter density and $\Omega_B = 4.9\%$ for baryon density.

1.2 Dark matter candidates

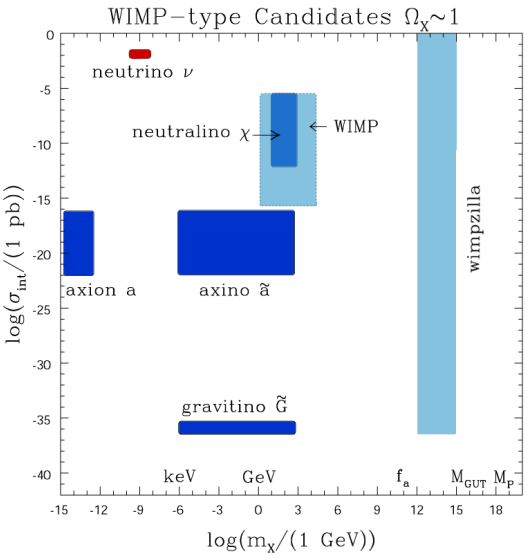

Figure 1.5: Scheme representing a summary of dark matter candidates. Cold dark matter candidates are in blue while hot dark matter is embodied in red by the neutrino from the SM [10].

If we now have many evidences supporting the presence of dark matter at different scales of the universe, its nature still remains (yet) a mystery. According to the observation discussed previously, dark matter does not have a weak electromagnetic interaction and might have a very weak interaction with baryons (it is even possible that dark matter interacts only gravitationally). Fig. 1.5 shows a set of dark matter candidates as a function of mass and the ranges interaction of cross section. In this section the most important dark matter candidates are treated briefly.

1.2.1 Neutrinos

Since the neutrino-oscillation experiments showed that neutrinos of the Standard Model (SM) have a mass [11], these particles became serious candidates as *we know they exist*. Unfortunately observation of CMB anisotropy demonstrates clearly that the total contribution of neutrino is not enough to account for dark matter [12]. Moreover an exceeding number of relativistic neutrinos (hot dark matter) would imply a different large scale structure than the one we know nowadays since at the epoch of the galaxy formation, an excess of primordial neutrinos would have washed out the structure on small scales. Studies of large scale structure formation support the view according to which the dominant fraction of dark matter is cold dark matter (CDM) [13]. However sterile neutrinos (hypothetical neutrinos with right handed) with a keV mass could account for all of dark matter [14]. Sterile neutrino can also explain pulsar kicks and other astrophysical phenomenon [15].

1.2.2 Axions

Axion is a hypothetical elementary particle introduced in 1977 by Peccei and Quinn in order to solve the strong CP problem in QCD [16]. The Standard Model cannot explain the small value of the CP violating parameter θ ($<10^{-9}$) for the strong interaction instead of being of the order of one. A solution to the strong CP problem was proposed by implementing new scalar particles beyond the Standard Model called axions.

Axions are considered as a potential CDM candidates because they are weakly interacting with ordinary matter. Some experiments try to detect axions in the dark matter halo of our galaxy using a tunable microwave cavity with a large superconductor magnet as ADMX [17]. Axions may be detectable during their conversion into microwave photons in the presence of a strong magnetic field. This mechanism is called the Primakoff effect [18]. An other technique, called light shining through the wall (LSW), consists in producing axions by converting photons from a laser beam in a magnetic field into axions while passing through the wall. On the other side of the wall, a second magnetic field is used to convert axions back into photons with the same wavelength as the original photons. Other experiment like CAST use a dipole magnet to convert axions, produced by the Primakoff effect occurring in the solar core, into detectable X-ray photons [19]. No such particle has been discovered so far and astrophysical and laboratory experiments constrain the axion

mass to be

$$10^{-6} \leq m_{axion} \leq 10^{-3}\,\mathrm{eV} \qquad . \tag{1.4}$$

1.2.3 WIMPs and thermal freeze out

The most promising candidates for cold dark matter are the so called weakly interacting massive particles (WIMPs): their masses should be in the range from 10 GeV to a few TeV. Such particles interact with ordinary matter through the weak force and gravity. This category of particles is produced thermally whereas dark matter axion is produced from non-thermal processes. At the beginning of the universe, when the temperature of the universe was higher than the mass of these particles (χ), a thermal equilibrium occurred leading to the creation of χ and to annihilation of its anti-particle $\bar{\chi}$ at the same rates. In the thermal equilibrium the density n_χ^{eq} of the particle χ is given by Eq. 1.5 [20]

$$n_\chi^{eq} = \frac{g}{(2\pi)^3} \int f(p) d^3p \tag{1.5}$$

where g is the number of degrees of freedom and $f(p)$ is either a Bose-Einstein or a Fermi-Dirac distribution. Since at the beginning of the universe $T >> m_\chi$ the dependency of the density of the particles χ on the temperature is $n_\chi^{eq} \sim T^3$. During the expansion of the universe, the temperature cooled down permanently, reaching a lower level than the temperature of the mass of the particle χ. During this phase, the equilibrium abundance dropped exponentially as far as the rate for the annihilation reaction dropped below the expansion rate of the universe. At this point, the density of the particle χ was frozen, originating a relic abundance from "the thermal freeze out". The density of WIMPS n_χ particle χ during the time evolution is described by the Boltzman equation [21]

$$\frac{dn_\chi}{dt} + 3Hn_\chi = - < \sigma v > [(n_\chi)^2 - (n_\chi^{eq})^2] \tag{1.6}$$

where H is the Hubble expansion rate and $< \sigma v >$ is the thermal average of the total annihilation cross section times the relative velocity. The second term on the left side corresponds to the expansion of the universe. On the right, the first term in brackets is related to annihilation and the second term corresponds to the creation of WIMPs.

1.2.4 Supersymmetry

Supersymmetry model (SUSY) is an extension of the SM which allows the unification of the three fundamental forces − the weak interactions, the strong interactions and electromagnetism − and provides a symmetry between boson and fermion. In the simplest supersymmetry model called minimal supersymmetry standard model (MSSM), each elementary particle from the SM has a superpartner, called sparticle, whose spin differs by a half-integer. The broken supersymmetry included in MSSM allows the mass of the sparticles to be heavier than their corresponding particles in SM and explains the reason why no superpartner has yet been discovered.

The most important candidate of weakly interacting massive particle is the lightest supersymmetric particle (LSP), which could be the neutralino, a linear combination of the superpartners of the Z boson (zino), the photon (photino) and the neutral higgs (higgsino). If the R-parity is conserved, LSP would be stable and all sparticles would eventually decay into LSP, making the neutralino a good dark matter candidate [22]. The R-parity is a quantum number which is defined as following

$$R = (-1)^{(3B+L+2s)} \quad , \tag{1.7}$$

where B is the baryon number, L is the lepton number and s is the spin. Particles from the SM have $R = 1$ and their superpartners $R = -1$.

Other extensions of the SM than SUSY also contain WIMP candidates such as Kaluza-Klein theory (KK) combining electromagnetism and gravity in a five dimensional space time [23]. In this theory a parity KK (conservation of the momentum along the extra dimension) is imposed leading to the lightest KK particle which is a viable dark matter candidate. The mass range of such a particle is from hundreds GeV to a few TeV.

"Little Higgs" models is an other example of a non-SUSY extension of the SM [24]. The Higgs bosons is a pseudo-Nambu-Goldstone boson resulting from a global spontaneously broken at a TeV scale. The introduction of the T-parity allows the existence of the lightest T-odd particle. This new stable heavy particle is weakly interacting and play the role of dark matter.

1.3 Indirect detection

Indirect detection is based on the detection of high energy particles such as neutrinos, positrons, antiprotons, and gamma rays produced by the WIMPs annihilation. Indirect signals from WIMPs annihilation depend on the annihilation products, the square of the dark matter density and their propagation effects. Three types of experiments generally aim at detecting signals from WIMPs annihilation:

- Via satellite, in order to detect primordial charged cosmic-rays like PAMELA [25] and AMS-01 [26]. PAMELA is designed for the observation of anomalous antiproton flux at energies above 10 GeV and excess of positrons, while AMS is studying a wider energy range from 0.5 to 2000 GeV. Imaging atmospheric Čerenkov telescope are also designed to study charged cosmic-rays as HESS [27] and MAGIC [28]. HESS is sensitive at 100 GeV while MAGIC at 50 GeV.

- Space telescope experiments EGRET [29] and FERMI LAT [30]. There are designed for Gamma-rays detection with energy range of 30 MeV to 30 GeV and 30 MeV to 300 GeV, respectively.

- Neutrino telescopes as ANTARES [31] and Ice Cube [32] that use, respectively, water and ice as detection medium. Neutrino flux can be enhanced by the WIMPs annihilation trapped at the center of the earth.

PAMELA observed a slight rise of positrons above 10 GeV which has been confirmed by FERMIT/LAT and HESS. Unfortunately this excess might be caused by astrophysical sources and seems unlikely that dark matter is at the origin of these excesses. Recently, FERMI LAT measured a new extended source about 130 GeV γ-ray line near the galactic center above and below the galaxy plane with a significance of 4.5σ [33] while the other point source detected at the center of our galaxy by HESS is about a TeV. The origin of both excess are also likely due to astrophysical sources. No WIMPs signal has been claimed and the observation of high energy gamma rays in the galactic halo by FERMIT/LAT were consistent with predictions based on astrophysical sources ruling out WIMPs models built to explain the measured excess of positrons.

The measurement of antiproton flux by PAMELA is in agreement with secondary production and propagation. This observation excludes WIMPs models explaining excess of positrons via annihilation into $W^{\pm}$ or Z^0 boson pairs.

The non-observation of high-energy neutrino fluxes from the galaxy center and from the center of the sun or the earth leads constraints on the DM annihilation cross section and on the scattering cross section of dark matter particles with nuclei, respectively. For a recent review of other indirect searches experiments refer to [34].

1.4 Direct detection

According to the observation of the rotation curves of galaxies, WIMPs should exist in our galaxy. Therefore, it should be possible to detect them "directly" via terrestrial detectors if the earth is evolving through a dark matter halo in our galaxy. The relative velocity of a terrestrial detector is approximated as :

$$v_D(t) = V_S + V_E \cos\psi \cos\left[\omega\,(t - t_0)\right] \tag{1.8}$$

where the velocity of the sun around the galaxy is $V_S = 230$ km s^{-1}, the orbit of the earth in the solar system is $V_E = 30$ km s^{-1}, ω is the angular velocity of the earth, ψ is the inclination of the earth's orbit relative to the motion in the dark halo, where the time of the highest relative velocity of the earth to the halo is denoted by t_0. The modulation in v_D leads to an annual modulation in the expected scattering rate of about 3% [35, 36].

WIMPs are extremely difficult to detect since they only interact throughout the weak nuclear force and gravity. However these neutral particles can be detected via the secondary products of the elastic scattering with a nucleus resulting in nuclear recoil. Many experiments use different targets to verify the A^2 dependence in the spin-independent cross section($A^2 \sim \sigma$) due to the coherent nature of the interaction. In this case the mass of the WIMP couples to the mass of the target whereas for the spin-dependent interaction the mass is coupling to the spin of the nucleons. The expected differential energy spectrum of nuclear recoils is featureless and is given by Eq. 1.9 [37]

$$\frac{dR}{dE_R} = \frac{R_0}{E_0 r} e^{-\frac{E_R}{E_0 r}} \quad , \tag{1.9}$$

where R is the event rate per unit mass, E_R is the nuclear recoil energy, E_0 is the most probable energy of WIMPs and R_0 is the total expected rate. The kinematic factor r is defined by $r = 4m_\chi m_N/(M_\chi + M_N)^2$, M_χ and M_N being the mass of WIMPs and the mass of the target nucleus respectively.

Because of this low interaction rate− which is for example ∼15 events/100kg/year in Ar at 30 keV threshold [38] −, a successful detector for direct dark matter detection must fulfill some requirements:

- High energy resolution and low energy threshold (∼10 keV) for the detection of nuclear recoils.
- Large target mass and/or long exposure time.
- Good discrimination between electron recoils and nuclear recoils in the energy range of interest for WIMP detection (0-100 keV).
- Low particle backgrounds mainly from γ rays and β decays producing electron recoils. These backgrounds are originated from different sources as: the radioactive isotopes in the surrounding material, the detector materials and the target itself. Detectors are located in deep underground laboratories to reduce cosmic rays muon-induced neutrons producing nuclear-recoils that are indistinguishable from a WIMP signal. Typically the total background event rate to perform a direct WIMPs detection is about 0.1-1 events/keV/kg/day.

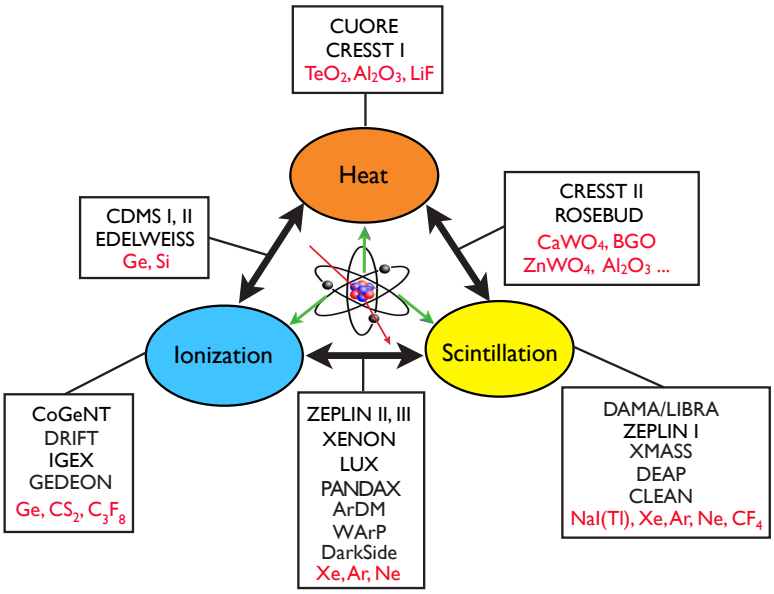

Figure 1.6: The techniques used by past and present and upcoming direct dark matter detectors.

During the collision between a WIMP and a target nucleus, the energy deposited can be transferred through three types of excitations: phonons (producing heat), ionization (producing charge) and scintillation (producing light). According to the materials detector, some experiments measure one or even two of these processes simultaneously especially in order to discriminate nuclear recoils from electron recoils. The first technique used for direct searches for dark matter and for setting the first limits were the semiconductor ionization detectors using high purity Ge and Si [39]. Ge and Si are also used for the construction of bolometers allowing the simultaneous measurement of ionization signal and phonon signal. Within the scope of WIMP searches, liquid noble gas technology such as xenon, argon and neon is the most popular technique to measure simultaneously two quantities. These material medium have good intrinsic properties: heavy mass, high ionization and scintillation efficiency, pulse shape discriminator (in LAr), self-shielding detectors and high radiopurity. Fig. 1.6 shows an overview of different direct detection techniques which can be classified as following:

- **Heat**: CRESST I [40] is the phase I of the project of the CRESST experiment located in Gran Sasso laboratory. This detector used 262 g sapphire (Al_2O_3) absorbers and tungsten (W) cryogenic thermometers (15 mK) to detect phonons. CUORE [41] will be a bolometric detector with the so-called calorimetric approach. This pure bolometer consists of 790 kg of TeO_2 crystals and and is initially designed for neutrino double beta decay measurement.

- **Heat/Ionization**: EDELWEISS [42] is a Ge bolometer measuring simultaneously the ionization signal and the phonon signal. CDMS [43] was an other experiment which belongs to this category of detector using Ge and Si.

- **Heat/Scintillation**: The second phase of CRESST [44] experiment includes the design of a detector able to measure the scintillation of the CaWO4 crystal which is read by a separate part of the phonon sensor while ROSEBUD [45] used an additional BGO crystal scintillator.

- **Ionization**: CoGenT [46] is the main experiment of this category and is located in Soudan Underground Laboratory. The 440 grammes p-type point contact (PPC) germanium detector, measuring only the ionization signal, presents the lowest noise threshold compared to any dark matter detectors and is ideal for dark matter searches involving a mass lower than 10 GeV/c^2.

- **Scintillation**: DAMA/LIBRA [47] is a solid detector measuring only the scintillation signal from a pure NaI crystal. Noble liquid like argon can also be used as a scintillator medium for a single phase detector as in DEAP/CLEAN project [48] or like xenon in ZEPLIN I [49] and XMASS [50] collaboration.

- **Scintillation/Ionization**: Several experiments designed two-phase Time Projection Chamber (TPC) detectors collecting charge and light by using liquefied noble gas. ArDM [51] and Dark Side collaboration use argon, while XENON 10,100, [52] LUX [53],ZEPLIN II,III project [54] and PandaX [55] use xenon.

1.5 Accelerator experiments

Dark matter searches at colliders such as Tevatron or at the Large Hadron Collider (LHC) can provide some complementary information to the terrestrial experiments searching directly for WIMPs through the study of kinematics variables. At the LHC dark matter which is denoted by χ is produced by the following reaction $q\bar{q} \rightarrow \gamma\chi\bar{\chi}$ where γ is irradiated from one of the quarks. The dark matter created in accelerators would escape without depositing any energy in the detector, resulting in a component of missing energy. Therefore colliders can only identify dark matter from the signal of the initial state radiation $\gamma + \not{E}_T$. The model used in this process assumes dark matter as a Dirac fermion and interaction is characterized by a contact interaction given by $\lambda = \frac{M_N}{\sqrt{g_x g_q}}$ where M_N is the heavy mediator mass and the couplings to χ and q are g_χ and g_q, respectively. The nature of the mediator will determine the form of χ-q couplings. If the effective s-channel operator is a vector moderator, the interaction is spin-dependent or if it is an axial-vector then the interaction is spin-independent. There are also many model dependencies on these analysis making difficult to draw a general conclusions. One of these extra spatial dimensions models is the Arkani-Hamed, Dimopoulos and Dvali model (ADD) [56] predicting the production of graviton G through the process $q\bar{q} \rightarrow \gamma G$.

The results of the CMS collaboration provide the most sensitive upper limits for spin-dependent χ-nucleon scattering for M_χ between 1 and 100 GeV as shown in Fig. 1.7 [57]. CMS also provides the most stringent upper limits for the independent cross section below 10 GeV [57].

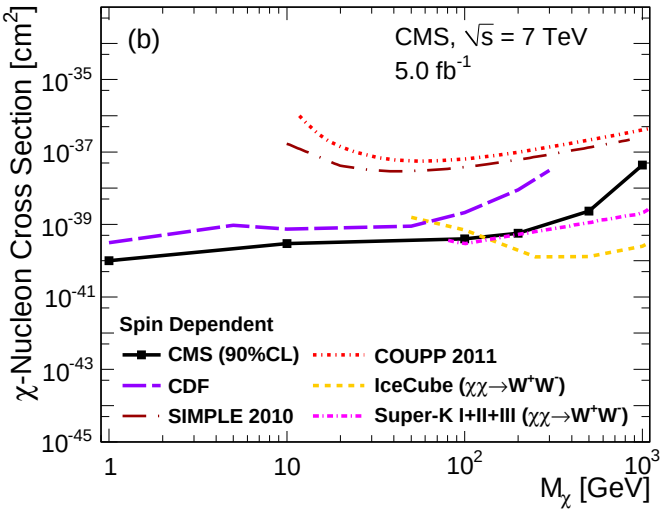

Figure 1.7: The 90% CL upper limits on the spin-dependent χ-nucleon cross section as a function of M_χ (from [57]).

1.6 Present experimental results and limits in direct detection

Lately dark matter searches have set some constraints on the spin-dependent and independent scattering cross section excluding some regions of the parameter space from SUSY model. DAMA was the first experiment claiming to have discovered dark matter in the galactic halo, observing an annual modulation with a significance of 8.9σ and a period of 0.998 ± 0.003 years between 2 and 6 keV [58]. The amplitude modulation, shown in Fig. 1.8, is 0.0131 ± 0.0016 cpd/kg/keV corresponding to 1.3% over the background rate. CoGent experiment observed as well an annual modulation with a statistical significance of $\sim 2.8\sigma$, $16 \pm 3.8\%$ modulation amplitude and a period of 347 ± 29 days [46]. CoGent collaboration interpreted the irreducible exponential background present in their data as a light WIMP signal with a mass of 7 GeV/c^2. A revised background analysis of CoGent can be found in [59].

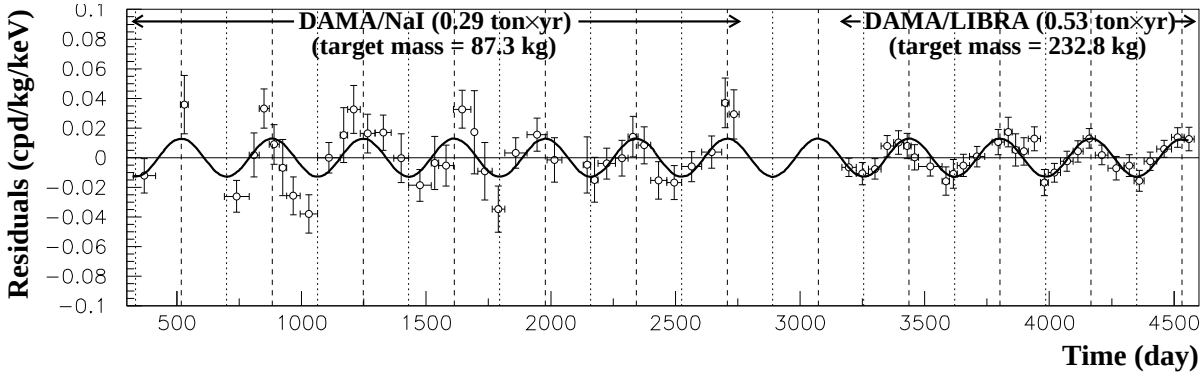

Figure 1.8: Annual modulation between 2 and 6 keV taken by DAMA collaboration [58].

The interest of low mass WIMP is reinforced by CRESST-II experiment observing a clear signal for light WIMPs $m_\chi < 10$ GeV/c^2 (in the oxygen recoils band) [60]. The experiment found 67 WIMPs candidates with a statistical significance of more than 4σ. The 2 events detected in the region of interest by CDMS with an expected background of $0.8 \pm 0.2(\text{stat.}) \pm 0.1(\text{syst.})$ were not sufficient to claim a discovery nor to reject them [61]. However CDMS collaboration using the silicon detectors (CDMS-Si) published the results from a blind analysis of 140.2 kg-days of data revealing three new WIMP events candidate with an expected total background of 0.7 events [62]. The maximum likelihood is reached for a WIMP mass of $m_\chi = 8.6$ GeV/c^2 and for a spin independent WIMP-nucleon cross section $\sigma = 1.9 \times 10^{-41}\text{cm}^2$.

XENON 100 collaboration has recently published their results of the blind analysis of 225 live days of data [63], setting the most stringent limit on the spin-independent elastic WIMP-nucleon scattering cross section for $m_\chi > 8$ GeV/c^2 with a minimum of $\sigma = 2.0 \times 10^{-45}$ cm^2 at $m_\chi = 55$ GeV/c^2 and 90% C.L. The results exclude the parameter space for light WIMPs obtained by DAMA, CoGenet and CDMS-Si. Between $6.6-43.3$

keV_{nr} of energy recoil range two candidates were observed to be consistent with the background expectation of 1.0 ± 0.2 events but were not sufficient for constituting an evidence supporting dark matter interaction. Fig. 1.9 shows the present limits of spin independent WIMP-nucleon scattering as a function of the WIMP mass obtained from different direct searches.

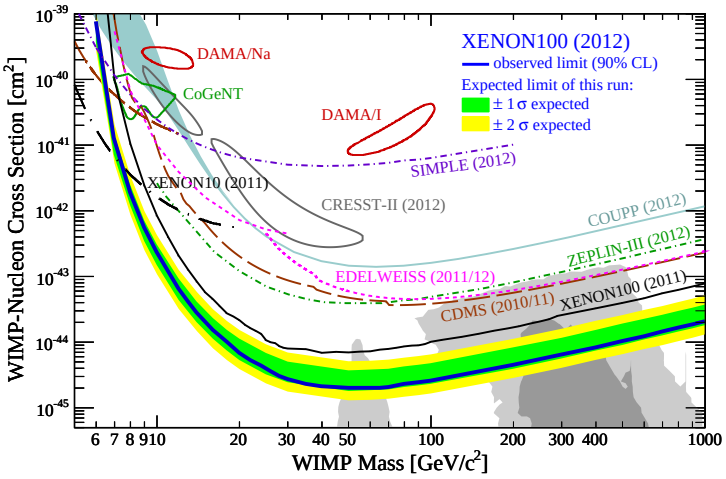

Figure 1.9: Recent limits of the spin independent cross section for different direct dark matter searches. The expected limit for XENON 100 is represented by the green/yellow band corresponding respectively to 1σ and 2σ. The blue curve shows the observed limit from XENON 100 at 90% C.L. and the grey areas are the regions with $1\sigma/2\sigma$ preferred by the supersymmetric models [63].

Chapter 2

Toward liquid argon as detection medium

As already discussed in the first chapter, a dark matter experiment measures the nuclear recoils signal in the energy below 100 keV induced by an elastic collision of elusive WIMPs. Liquefied noble gas such as xenon and argon offer advantageous features for WIMPs detection like high density, high scintillation yield and high ionization, thanks to their low ionization potential. The advantage of argon is that it is extremely cheap compared to other noble gases if it not depleted from ^{39}Ar. Ionization charge and scintillation light can be detected in order to identify different types of interactions. Moreover, the time dependence of the scintillation light provides an intrinsic discrimination between WIMPs and background signals.

This chapter describes the properties of liquid argon (LAr) and the interactions of different types of particles leading to ionization and scintillation. I will review the mechanisms responsible for the reduction of signal yields depending upon atomic motion and ionization density and present the current model describing the relative scintillation efficiency. I will define the different energy scales used in direct dark matter searches to characterize interactions occurring in noble liquid detectors. Finally I will describe how to extract WIMP-like signals from background signals.

2.1 Properties

Argon is an inert chemical element which was the first noble gas discovered at the end of the 19$^{\text{th}}$ century. It is quite abundant in the Earth's atmosphere (9300 ppm) and can be produced easily by fractional distillation of liquid air. The natural composition of argon on the earth consists of 3 stable isotopes – ^{40}Ar (99.6%), ^{36}Ar (0.34%), and ^{38}Ar (0.06%) – and one unstable isotope ^{39}Ar which is a β-emitter resulting from the interaction between cosmic rays and ^{40}Ar. The activity of ^{39}Ar in natural argon is estimated to be about 1 Bq/kg with a half-life of 269 days and produces low energy background rate of about 10^7 electronic recoils/keV/yr/100 kg [64]. As an alternative, underground sources of argon

depleted in ^{39}Ar are also being studied because ^{39}Ar production is strongly suppressed underground. Argon's boiling point is 87.293 K at atmospheric pressure. Tab. 2.1 lists the other physical properties of the LAr [65].

Due to its interesting properties, LAr medium is not only limited to WIMPs detection: indeed, LAr is used for alternative applications such as for neutrino oscillation studies conducted by ICARUS experiment [66], for $\beta\beta(0\nu)$ decay studies [67], as calorimeter for ATLAS detector in LHC [68] or as scintillation veto in GERDA experiment [69].

atomic number	18
density GAr at 1 atm (0^o)	1.782 g/l
density LAr at 1 atm	1.396 kg/l
melting point	83.8058 K
boiling point	87.293 K
ionization density	15.7596 eV
Radiation length	14 cm

Table 2.1: Physical properties of argon [65].

2.2 Neutron and γ interaction in liquid argon

The type of neutron interactions with an argon atom depends on the energy of the incident neutron. Neutrons being neutral particles, they do not interact directly with electrons but are confined to direct nuclear effects and nuclear reactions. The three types of interaction that neutrons may undergo in LAr are the following:

- Elastic scattering producing nuclear recoils
- Inelastic collision leading to γ emission and nuclear recoils
- Neutron capture with subsequent emission of a γ and Auger electrons

For fast neutrons (neutrons with energy between 1 MeV and 20 MeV), elastic collision is the most important interaction process to produce nuclear recoils. The energy E_R transferred by the projectile particle into a target nucleus with an atomic mass A can be generalized as [70]:

$$E_R = \frac{2m_n E_n}{(m_n + A)^2}\left(m_n + A - m_n \cos^2\theta - \cos\theta\sqrt{A^2 + m_n^2\cos^2\theta - m_n^2}\right) \tag{2.1}$$

where m_n is the mass of the projectile, E_n its energy and θ the scattering angle in the laboratory frame. In the case of non relativistic neutrons ($E_n << m_n c^2$) interacting with a heavy target nucleus such as argon ($A >> m_n$), the Eq. 2.1 can be approximated as

$$E_R \simeq \frac{2A}{(1+A)^2}(1 - \cos\theta)E_n \quad . \tag{2.2}$$

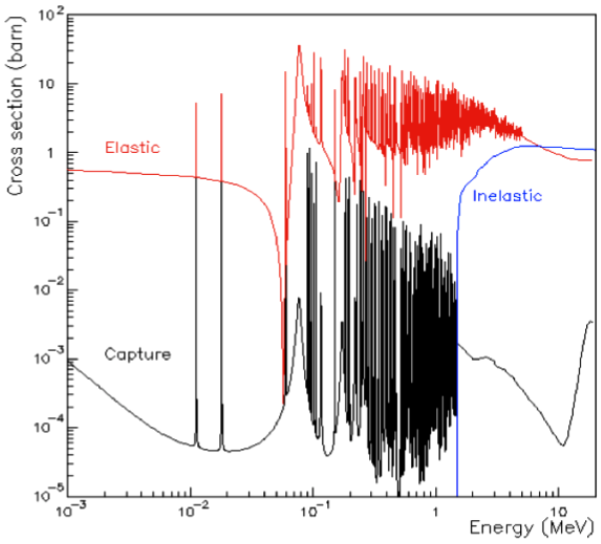

Figure 2.1: Neutron elastic scattering (red), inelastic scattering (blue) and capture (black) cross sections on LAr (from [71]).

Beyond a couple of MeV energies, the effect of the inelastic collision is not negligible anymore being of ∼1 order of magnitude lower than the elastic collision for incoming neutrons at 2.45 MeV. Inelastic scatterings produce low energy γ (∼ keV) and Auger electron of energy ∼9.4 eV. The neutron capture reaction should dominate for thermal energies (0.025 eV) and resonances are also observed at keV energies range. The $^{40}\mathrm{Ar}(n,\gamma)^{41}\mathrm{Ar}$ reaction produces keV electron and 1.3 MeV γ from the ^{41}Ar decay. Fig. 2.1 shows the cross section for neutron total elastic scattering, inelastic scattering and neutron capture in LAr as a function of the energy.

In the context of dark matter search, neutron inelastic collision doesn't present a background because the γ emission followed by the nuclear recoil shifts the energy from the event of the region of interest (30-100 keV). However, since its event topology is similar as WIMPs, neutron elastic scattering might be an issue because both particles produce a recoiling argon nucleus. A neutron event mimicking WIMP interactions is called a WIMP-like event. The WIMP cross section being very low in comparison to the neutron cross section, the information of the number scattering from WIMP-like events constitutes an important mean allowing to distinguish both particles. A WIMP should only interact once while neutrons present multiple scatterings. With an energy between 100 keV and 10 MeV, the range of the mean free path from neutron elastic scattering varies from 26 to 19 cm. A simulation has been designed in order to be able to study the scattering multiplicities in 1 ton LAr detector such as ArDM [72]. In the energy range of interest, only 10% of neutrons produced single scattering.

The interaction of a photon with the matter involves three competing processes: photoelectric effect, Compton scattering and pair production. All these processes lead to

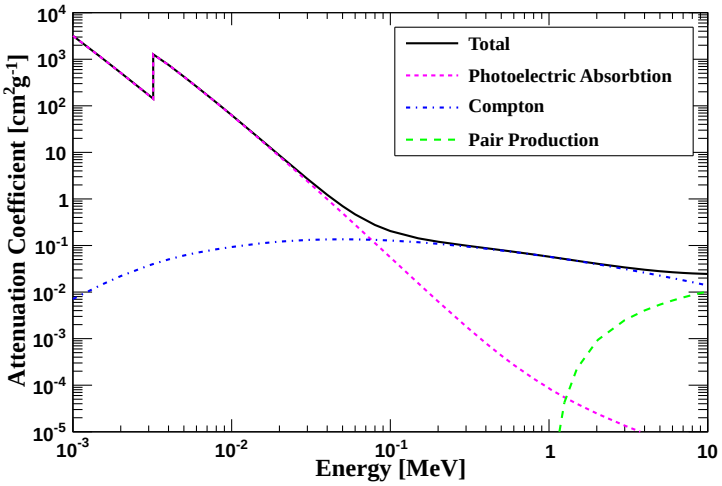

Figure 2.2: Total (black), photoelectric absorption (magenta), Compton scattering (blue) and pair production (green) attenuation coefficient for γ-rays in LAr (plot made with the data from XCOM database [73]).

the creation of electrons which lose their energy through electronic excitation and then produce excitons and electron-ion pairs. During the photoelectric interaction and the pair production mechanism, the photon is completely absorbed and an electron is emitted while in the Compton process, the photon only transfers some part of its energy to a recoiling electron. Fig. 2.2 shows the total, photoelectric absorption, Compton scattering and pair production attenuation coefficient for γ in LAr. The photoelectric absorption represents the most dominant process below 80 keV whereas the Compton scattering constitutes the dominating interaction above this energy. Assuming a density of 1.396 g/cm^3 at 1 atm, the interaction length for γ-rays at 60 keV is $\sim$1.5 cm and $\sim$12.4 cm at 1 MeV. Therefore for a 1 ton LAr detector such as ArDM, the main background causing electron recoils in the energy region of interest will be low energy Compton scatters and most of low-energy γ-rays will be absorbed outer the fiducial volume.

2.3 Scintillation mechanism

The interaction of an ionizing particle in LAr produces a scintillation light in the vacuum ultra violet region (VUV) with photon 128 nm of wavelength (FWHM$\simeq$6 nm) corresponding to an energy of 9.7 eV [74]. During the collision, the recoiling particle excites or ionizes the surrounding argon atoms, producing excimers Ar_2^* (excited molecules) which decay radiatively into VUV scintillation light. There are two processes forming Ar_2^*:

- Excitons Ar^* (excited atoms) directly interact with the neighboring argon atoms, forming excimers:

$$Ar^* + Ar \rightarrow Ar_2^* \rightarrow 2Ar + \gamma(128nm) \quad . \tag{2.3}$$

- Ionized atoms can also form excimers via a recombination between Ar_2^+ and the thermalized secondary electrons:

$$Ar^+ + Ar \rightarrow Ar_2^+ + e^- \rightarrow Ar^{**} + Ar \rightarrow Ar_2^{**} \rightarrow Ar^* + Ar + \text{heat} \quad . \tag{2.4}$$

According to Hitachi *et al.* [75], the average number of electron-hole pairs (ionization) N_{ion} produced by the absorption of energy E in LAr is determined by

$$N_i = \frac{E}{W_{ion}} \tag{2.5}$$

where the ionization energy W_{ion} has been estimated to be 23.6 eV. The ratio between the number of excitation N_{ex} and the number of ionization has been measured to be $N_{ex}/N_{ion} = 0.21$. These information allow to deduce the average energy for a scintillation photon emission:

$$W_{pho} = W_{ion}\Big(1 + \frac{N_{ex}}{N_{ion}}\Big)^{-1} = 19.5\,\text{eV} \tag{2.6}$$

which corresponds to a photon yield about 51 photons/keV in the ideal case (no quenching mechanisms and no detection efficiency are taken into account).

Excimers are produced in two singlet states, $^1\Sigma_u^-$ and $^1\Sigma_u^+$, and in a triplet state $^3\Sigma_u^+$. The singlet state $^1\Sigma_u^-$ doesn't emit photon because of the parity conservation. Therefore the scintillation light possesses two components: those stemmed from the transitions $^1\Sigma_u^+ \rightarrow^1 \Sigma_g^+$ (fast decay) and $^3\Sigma_u^+ \rightarrow^1 \Sigma_g^+$ (slow decay) where $^1\Sigma_g^+$ is the ground state. The decay of the singlet state is strongly allowed and its decay time τ_1 is of the order of ns. The triplet state has a longer lifetime because of the strong spin-orbit coupling in Ar_2 and its decay time τ_2 is measured to be $1.6\mu s \pm 0.1$ [76]. The scintillation emitted cannot be absorbed in LAr because the energy of photons is too low to be able to excite the ground state atoms. The population of the singlet and triplet state depend on the ionization density. Their lifetimes are independent on the other hand. Particle discrimination in LAr is based on the relative intensity of the singlet and triplet states which results from the ionization density.

2.4 Energy dependent light yield in LAr

It is well known that for nuclear recoils in liquid noble gas, only a fraction of the energy deposit leads to ionization and scintillation. The rest of the energy is transferred to atomic motion and lost in heat without electrically exciting or ionizing argon target. This effect is called nuclear quenching and is described by the Lindhard theory [77]. Although this theory succeeds in describing the quenching in solid state detectors [78], it is not sufficient to explain the reduced scintillation at high ionization density in noble liquid. The luminescence quenching depends upon other processes:

- A.Hitach and T.Doke [75] proposed a mechanism in which free excitons diffused and underwent a bi-excitonic collision producing an electron-ion pair :

$$Ar^* + Ar^* \rightarrow Ar + Ar^+ + e^- \quad . \tag{2.7}$$

This process occurs before the creation of excimers and becomes significant at high ionization densities.

- The penning process: a reaction between two excimers forming one ground state and one exciton [79]

$$\mathrm{Ar}_2^* + \mathrm{Ar}_2^* \rightarrow 2\mathrm{Ar} + \mathrm{Ar}_2^+ + \mathrm{e}^- \quad . \tag{2.8}$$

- Superelastic collisions quenching the singlet states to the triplet states [80].
- Influence of an external electric field on the recombination of electron-ion pair drifting the ionized ions and electrons. This reduces the recombination and therefore the scintillation light.
- Purity effects: scintillation light is reduced because of the collision between excimers and atoms generated by impurities.

2.4.1 Lindhard theory

The total average energy lost per unit path length by an ionizing particle during the nuclear recoil process can be expressed by the sum of the contribution of electronic and nuclear stopping powers:

$$\left(\frac{\mathrm{d}E}{\mathrm{d}x}\right)_{\mathrm{total}} = \left(\frac{\mathrm{d}E}{\mathrm{d}x}\right)_{\mathrm{elec}} + \left(\frac{\mathrm{d}E}{\mathrm{d}x}\right)_{\mathrm{nucl}} \quad . \tag{2.9}$$

Electronic stopping power is defined as the energy deposited per unit distance by the nuclear recoil to excite or ionize the surrounding atoms. The nuclear stopping power is the energy loss per unit length caused by atomic collision. In such a collision the energy lost is transferred kinematically and does not contribute to the production of the scintillation light (emissionless collisions). Lindhard suggested that the total energy lost E_R by the particle could be expressed in terms of electronic $\eta(E_R)$ and nuclear $\nu(E_R)$ stopping power as following [77, 81]:

$$E_R = \eta(E_R) + \nu(E_R) \quad . \tag{2.10}$$

The contribution of the energy lost in electronic excitation and leading to the creation of excitons and electron-ion pairs is represented by

$$f_n(E_R) \equiv \frac{\eta(E_R)}{E_R} = \frac{\eta(E_R)}{\eta(E_R) + \nu(E_R)} \quad , \tag{2.11}$$

using the total stopping power Eq. 2.9, f_n can be expressed by the ratio of two integrals

$$f_n(E_R) = \frac{\int_0^{E_R} (\mathrm{d}E/\mathrm{d}x)_{\mathrm{elec}}\, \mathrm{d}E}{\int_0^{E_R} (\mathrm{d}E/\mathrm{d}x)_{\mathrm{tot}}\, \mathrm{d}E} \quad . \tag{2.12}$$

The last expression needs to be evaluated for any possible recoil energies and can be approximated by

$$f_n = \frac{k \cdot g(\varepsilon)}{1 + k \cdot g(\varepsilon)} \qquad \text{with} \qquad k \simeq 0.133\ Z^{2/3} A^{-1/2} \qquad , \tag{2.13}$$

where k is a constant for a given type of atom target with its corresponding atomic number Z and mass number A, and $g(\varepsilon)$ is well fitted by ([82])

$$g(\varepsilon) \simeq 3\ \varepsilon^{0.15} + 0.7\ \varepsilon^{0.6} + \varepsilon \qquad . \tag{2.14}$$

Fig. 2.3 shows the ionization energy reduction factor as a function of recoil energy estimated by Lindhard's theory for Ar, Xe and Ne.

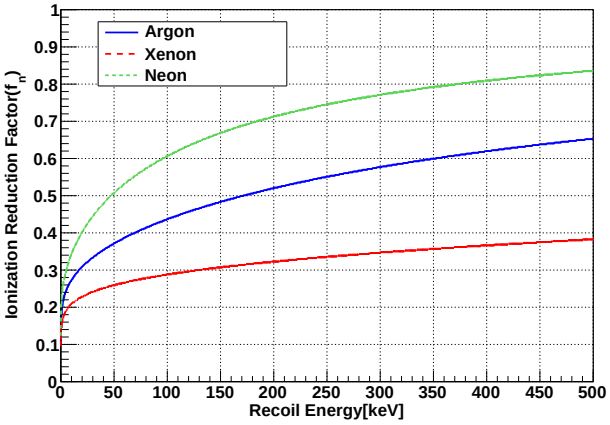

Figure 2.3: Ionization energy reduction factor (f_n) as a function of the recoil energy for argon (blue), xenon (red) and neon (green) (from Eq. 2.13).

2.4.2 Model for reduced scintillation light at high ionization density

A recoiling particle produces a track of excitons and ionized atoms which can be described in terms of core and penumbra as proposed by Hitachi and Doke. The core is the zone of the track with a high energy deposition density and the penumbra surrounding the core corresponds to a lower density zone. According to Hitachi's model, the luminescence quenching occurs exclusively in the core via bi-excitonic collisions or penning processes apart from the fission fragment.

Assuming that the density of excitons and electron-ion pairs created along the track of the particle is directly proportional to electronic energy loss $\left(\frac{\mathrm{d}E}{\mathrm{d}x}\right)_{\mathrm{elec}}$, the scintillation light yield can be written without taking into account the luminescence quenching as

$$\frac{\mathrm{d}S}{\mathrm{d}x} = A\left(\frac{\mathrm{d}E}{\mathrm{d}x}\right)_{\mathrm{elec}} \tag{2.15}$$

where A is a proportionality constant. There is also a proportionality between the local concentration of the core and the electronic stopping power which is given by $B\left(\frac{\mathrm{d}E}{\mathrm{d}x}\right)_{\mathrm{elec}}$. To take into account the probability of the quenching, the overall collision probability in the core, which is denoted by k, must be implemented in the Eq. 2.15. Thus in the presence of the luminescence quenching, the scintillation light response is described by the Birk's law saturation:

$$\frac{\mathrm{d}S}{\mathrm{d}x} = \frac{A\left(\frac{\mathrm{d}E}{\mathrm{d}x}\right)_{\mathrm{elec}}}{1 + kB\left(\frac{\mathrm{d}E}{\mathrm{d}x}\right)_{\mathrm{elec}}} \tag{2.16}$$

and therefore the reduced scintillation light at high ionization density can be expressed as

$$f_l = \frac{1}{1 + kB\left(\frac{\mathrm{d}E}{\mathrm{d}x}\right)_{\mathrm{elec}}} \tag{2.17}$$

where kB also called also Birk's constant can be obtained experimentally. For LAr $kB = 7.4 \times 10^{-4}\,\mathrm{MeV^{-1}g\,cm^{-2}}$ was determined from heavy ion measurement assuming a quenching factor of 46% [83].

2.4.3 The influence of the electric field

When an electric field is applied, free electrons drift from the ionization track, decreasing the probability of recombination and therefore affecting the scintillation signal. Therefore it is important to correct the scintillation loss for TPC detectors applying an electric field to collect ionization signal. In order to quantify the scintillation loss, measurements of the variation of scintillation light and ionization in liquid argon using relativistic heavy ions under an electric field have been performed in [84]. Results obtained are shown in Fig. 2.4, indicating that the quenching is stronger with the intensity of the applied electric field.

In the case of TPC detectors applying an electric field like ArDM or XENON experiment, two additional efficiency correction factors must be taken into account, S_e and S_n for electron recoils and nuclear recoils. In the absence of electric field, these factors become $S_e = S_n = 1$.

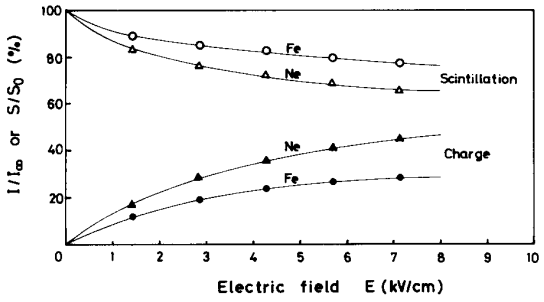

Figure 2.4: Variation of scintillation light and ionization in liquid argon as a function of applied electric field for Fe and Ne (from [84]).

2.4.4 The effect of impurities

Impurities in LAr (N_2, O_2, H_2O and $CO + CO_2$), caused by the outgassing in the detector can quench argon excimers or absorb the VUV scintillation light emitted from the argon excimers decay. The expected effect of the non-radiative collisional reaction represented in Eq. 2.18, is a decreasing of the triplet lifetime, as already observed by Himi *et al.* in [85] by increasing the concentration of N_2 during his measurement. Since triplet states have a long lifetime, they undergo various collisions with neighbors before decaying eventually, which leads to a reduction of the scintillation light intensity.

$$Ar_2^* + X \rightarrow 2Ar + X + \text{kinetic energy} \tag{2.18}$$

The WArP collaboration has recently carried out additional studies to quantify the reduction of the triplet lifetime and the quenching of the scintillation light in LAr caused by N_2 and O_2 contaminants. Details of these measurements may be found in [86, 87] and their results are summarized in [88]. The triplet state is the scintillation component that is the most affected by the impurities contamination level, whereas the singlet and the intermediate state are not affected by the impurities above 10ppm as observed in this work (Section 4.6).

2.5 Relative scintillation efficiency $\mathcal{L}_{\text{eff}}$ from Lindhard and Hitachi models

The previous section has been tackling the different processes leading to the production of the luminescence thanks to the deexcitation of the singlet state and the triplet state. The mechanisms responsible for the reduction of the scintillation have been discussed. In order to fully describe the luminescence quenching for noble liquid, Mei *et al.* [89] combined Lindhard theory, represented by the factor f_n and expressed in Eq. 2.13, and Birk's saturation law f_l using the Eq. 2.17. Since f_n and f_l are independent for each other, the result of this combination is simply the multiplication of these two reduction factors:

$$q_n = f_n \times f_l \tag{2.19}$$

where q_n is called the quenching factor or the total scintillation efficiency. Fig. 2.5 shows the total scintillation efficiency as a function of the recoil energy in for argon, xenon and neon. For liquid argon q_n becomes constant roughly at 0.27 for recoil energies above 50 keV.

Since it is difficult to determine experimentally with a good precision the "absolute" scintillation yield, the conversion of the scintillation signals to nuclear recoils energies is possible by determining the relative scintillation efficiency. The relative scintillation efficiency is usually denoted by $\mathcal{L}_{\text{eff}}$ and is defined as the ratio of the scintillation yield of nuclear recoil to the scintillation yield of electron recoil from a photoabsorbed γ-source.

$$\mathcal{L}_{\text{eff}} = \frac{L_{y,nr}(E_{nr})}{L_{y,er}(E_{er} = 59.5\,\text{keV})} \qquad \text{at zero electric field,} \tag{2.20}$$

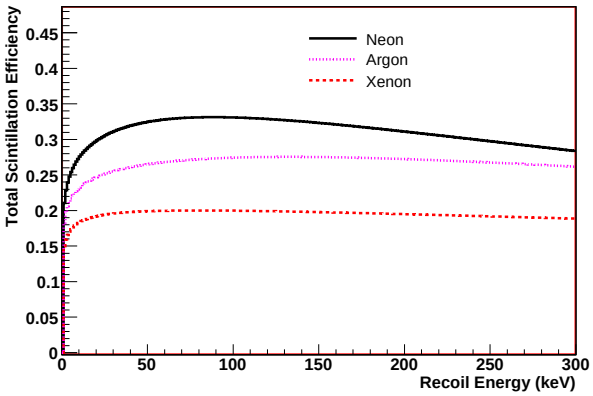

Figure 2.5: Total scintillation efficiency for nuclear recoil as a function of recoil energy in liquid argon (red dotted line), xenon (magenta dashed line) and neon (black line) (from [89]).

where the subscripts "*nr*" and "*er*" are used for nuclear recoil and electron recoil. Since $\mathcal{L}_{\text{eff}}$ is an energy dependent quantity, a standard reference for calibration is required. The common photoabsorbed γ-rays used for liquid xenon detectors and other experiment using liquid argon (micro-CLEAN,WArP) are typically from the ^{57}Co source (E_{er} = 122 keV). For convenience sake, we use the photoabsorbed 59.5 keV γ-rays in the context of this work. In LAr, measurement of the light output response to electron recoils using different radioactive sources from 59.5 keV to 1275 keV shows a linear behavior. Therefore, we can directly compare the measurement of $\mathcal{L}_{\text{eff}}$ in LAr obtained from this work with the results collected by micro-CLEAN experiment which has performed a calibration using the 122 keV γ-line.

Two techniques have been employed to measure $\mathcal{L}_{\text{eff}}$:

- **Indirect measurement**: Comparison between a continuum-energy source of neutrons with a simulated spectrum. $\mathcal{L}_{\text{eff}}$ is obtained by applying iteratively a fit procedure until the best fit with the measured spectrum is achieved [90].
- **Direct measurement**: Study of the measured response by recording at fixed angle the single elastic scattered from a monochromatic neutron source [91, 70].

My thesis will focus on the determination of $\mathcal{L}_{\text{eff}}$ at zero electric field using the direct measurement method described above. Results on $\mathcal{L}_{\text{eff}}$ performed by micro-CLEAN are shown in Fig. 2.6 with the superimposed result from WArP [92] and the $\mathcal{L}_{\text{eff}}$ model. Below 20 keV, a rise of the $\mathcal{L}_{\text{eff}}$ is observed at low energies, which is in disagreement with the model, whereas in LXe the values of $\mathcal{L}_{\text{eff}}$ decrease with the decrease of the energy.

2.6 Energy scale

As previously mentioned $\mathcal{L}_{\text{eff}}$ is used to convert the scintillation signal into nuclear recoil energies. Since the amount of the total light produced by electron recoils and nuclear

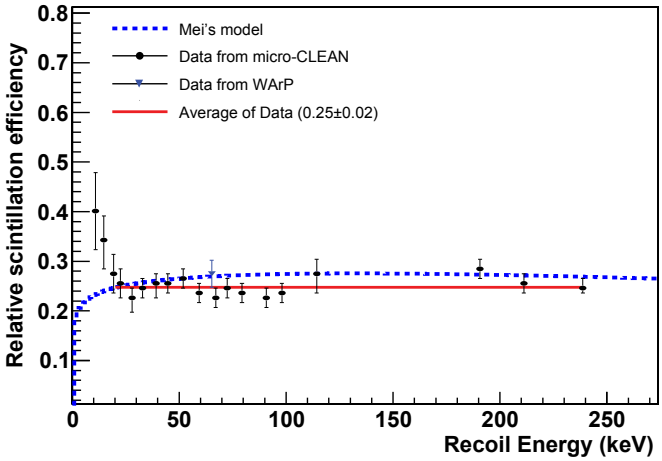

Figure 2.6: Relative scintillation efficiency $\mathcal{L}_{\text{eff}}$ as a function of recoil energy. The red line indicates the average of $\mathcal{L}_{\text{eff}}$ above 20 keV.

recoils at a given energy is different, two energy scales are defined to assign an energy to the signal detected in the detector for both types of interactions:

- **Electronic-recoil equivalent energy**: The unit of this energy scale is denoted by "keV$_{ee}$" and quantifies the amount of scintillation light S (signal measured in number of photoelectrons) in terms of energy that would be produced by a recoiling electron. E_{er} is obtained as following:

$$E_{er} = \frac{S}{L_y} \tag{2.21}$$

  where L_y is the light yield of electron recoils using the reference calibration γ-rays source and is expressed in p.e./keV$_{ee}$.

- **Nuclear-recoil equivalent energy**: Energy scale for nuclear recoils E_{nr} can be reconstructed from the scintillation light of nuclear recoil S as following

$$E_{nr} = \frac{S}{L_y}\frac{1}{\mathcal{L}_{\text{eff}}}\frac{S_{er}}{S_{nr}} \tag{2.22}$$

  S_{nr} and S_{er} are respectively the scintillation field correction factors for nuclear and electron recoils. The unit of E_n is expressed in keV$_{nr}$.

2.7 Particle identification

One of the main properties of liquid argon is its pulse shape discriminator (PSD). This capability is caused by the different time dependence of scintillation light for nuclear and

electron recoils. Since the relative intensity between the singlet and the triplet states strongly depends on the ionization density, as discussed earlier, and that their decay time are quite different from one another, a discriminant variable can be used to identify the type of the incident particle. This discriminant variable is denoted by F_p in this work and is obtained via the fraction of the prompt light over the total light [93] (Section 4.2.2.5). F_p is respectively about 1:4 and 3:4 for electron recoils and nuclear recoils. A sketch represented in Fig. 2.7 shows that the signal produced by electron recoils has more light from the decay of the triplet states compared to nuclear recoils. This technique is widely used to eliminate γ-rays induced by fast neutron detection especially in the liquid organic scintillators (Section 3.2.1).

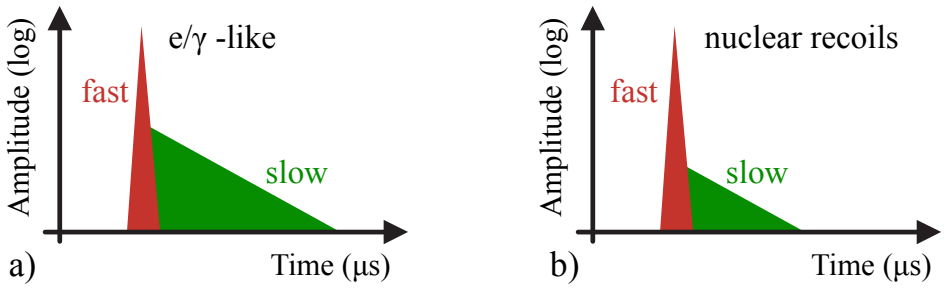

Figure 2.7: Sketch representing the scintillation time structure for electron recoil (a) and nuclear recoil (b).

Chapter 3

Description of the experimental setup

Any direct WIMP search experiment involving liquefied noble gases such as argon requires a low energy detection threshold of a few keV. XENON100 reported in their results that the largest systematic uncertainty was the uncertainty in the nuclear recoil energy scale at low energies [63]. Therefore, the determination of the relative scintillation efficiency, ($\mathcal{L}_{\text{eff}}$), turns out to be crucial for understanding nuclear recoil and quantify the WIMP detection sensitivity at this energy scale. To achieve this goal, the University of Zurich group has designed a neutron scattering facility and installed it in our laboratory at CERN. This Chapter describes the method and the devices used for measuring $\mathcal{L}_{\text{eff}}$ in LAr.

3.1 Measurement technique

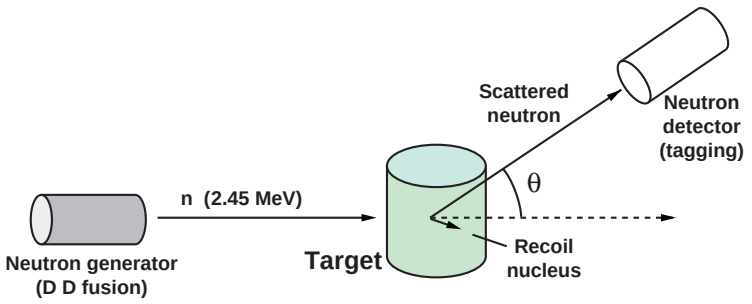

Figure 3.1: Scheme of the neutron scattering experiment.

A simple description of the method of the neutron scattering experiment is represented by the Fig. 3.1. A LAr chamber is irradiated by neutrons emitted by a monoenergetic source (DD neutron generator). The neutron energy deposited in LAr is fixed by the scattering angle θ, according to Eq. 2.2 and the scattered neutron is detected by an organic

liquid scintillator counter (LSC) placed at the same angle θ. Each event is recorded by the coincidence measurement of LAr and LSC signals. Thanks to the time of flight technique, the LSC signal tells us whether there is a candidate event. From all this information the light output produced by nuclear recoils at this energy can be compared to the reference electron recoil light yield in order to determine the $\mathcal{L}_{\text{eff}}$.

3.2 Organic liquid scintillator counter (LSC)

Organic scintillators are materials widely used in fast neutron spectroscopy and time of flight measurements due to their excellent pulse height and timing resolution. The additional features of this type of detector is the pulse shape discrimination capacity, due to excitation of different fluorescence mechanisms by particles with different ionizing power.

3.2.1 Pulse shape discriminator (PSD)

The scintillation light emission is dominated by prompt fluorescence mechanism. On the other hand, at the same time as this decay of a few ns, there is a slow component decay time of hundreds of ns. One of the main properties of the organic scintillation is that with such detectors, a PSD is made possible, which allows to identify the type of incident particle. As in LAr, this technique rests on the fact that the difference of the relative intensities of the slow component, depending on the specific energy loss of the particle ($\mathrm{d}E/\mathrm{d}x$). In contrast to LAr, the relative intensities of the slow component increase with $\mathrm{d}E/\mathrm{d}x$. When particles present a large $\mathrm{d}E/\mathrm{d}x$, the density of excitons is higher along the track of the particles (see Section 2.5) which results in increased bimolecular interactions between two excited states responsible for the delayed fluorescence. Therefore this type

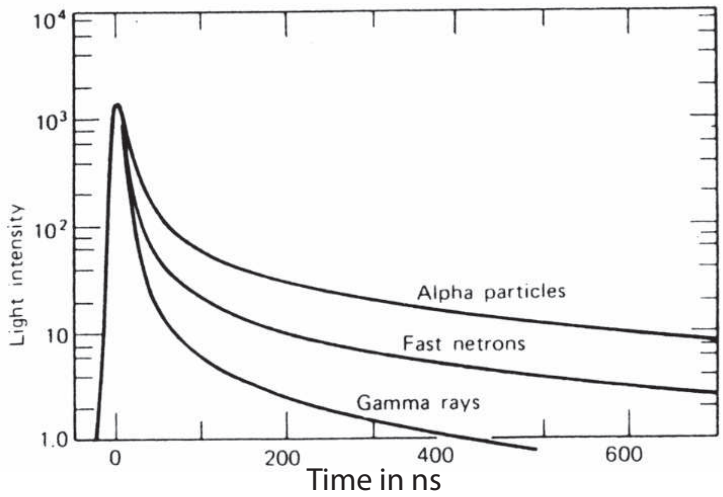

Figure 3.2: Time dependence of scintillation light produced by various projectiles (from [94]).

of interaction will increase the slow part in the scintillation light, allowing a PSD on the signal between neutron (proton recoils) and gamma (electron recoils) Fig. 3.2.

3.2.2 EJ301 LSC

The EJ-301 used in the project is a liquid scintillator manufactured by SCIONIX coupled to a 3 inch XP4312B photomultiplier with an aluminum cell filled with Anthracen ($C_6H_4(CH_3)_2$), as illustrated in Fig. 3.3. The scintillating liquid of the EJ-301 is equivalent to the one used for NE-213 or BC-501A. Tab. 3.1, shows some technical data about the scintillator. This kind of detector can be used for fast neutrons and gives information on the neutron energy since the recoiling proton is fully absorbed in the cell. In this context the term "proton recoil" used to indicate the recoiling particle in the LSC is the synonym of the nuclear recoil in LAr.

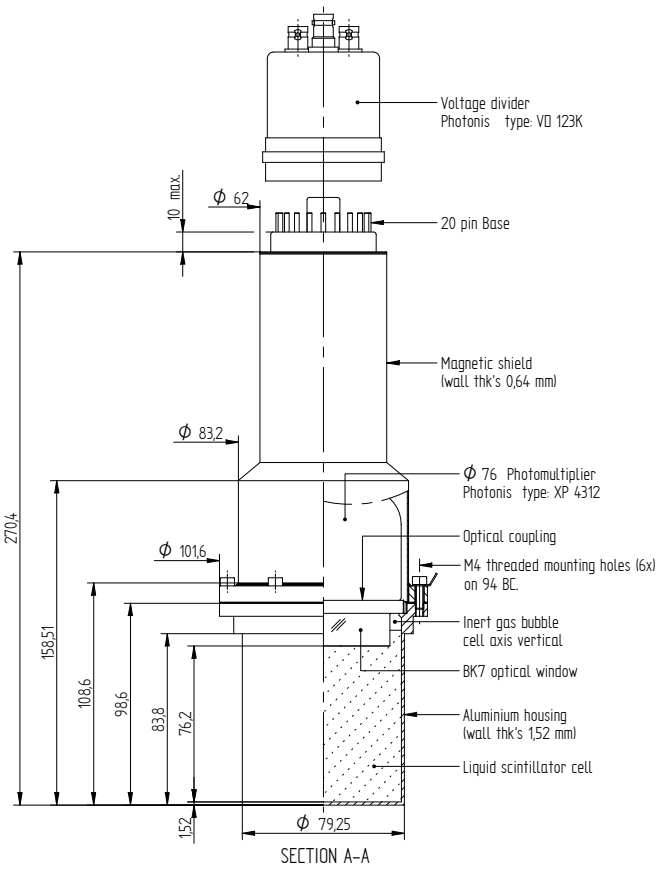

Figure 3.3: View of the 3" LSC.

Density	0.874g/cm^2
Refractive Index	1.508
Light Output(% Anthracen)	78
Decay Time (fast component)	3.7 ns
Wavelength of maximum emission	425 nm
Ratio of H to C atoms	1.213

Table 3.1: Technical data on EJ301 (from [95]).

3.2.3 Neutron interactions in LSC

The neutron elastic scattering off hydrogen represents the most common method for fast neutron detection for two reasons: because of the large cross section within the energy of interest and of the energy dependence of neutrons scattering off hydrogen, which is well known nowadays. The formula Eq. 2.1 allows to deduce that light nuclei (especially hydrogen or deuterium nuclei) are the most efficient moderators for neutron. In the context of a central collision ($\theta \simeq 0$) the maximum energy transferred by the incoming neutron into a target nucleus with an atomic number A is

$$E_R|_{max} = \frac{4A}{(1+A)^2} E_n \qquad . \tag{3.1}$$

It is obvious that the maximum energy transfer into the recoil nucleus is lower in the case of heavier target nucleus; with hydrogen, the neutron transfers all of its energy in a single interaction. The maximum fractional energy transferred in the neutron elastic collision for different target nuclei are listed in Tab. 3.2.

Target Nucleus	A	$\frac{E_R}{E_n}\|_{max} = \frac{4A}{(1+A)^2}$
$^1_1$H	1	1
$^2_1$H	2	8/9=0.889
$^3_2$He	3	3/4=0.750
$^4_2$He	4	16/25=0.750
$^{12}_6$C	12	48/169=0.284
$^{16}_8$O	16	64/289=0.221

Table 3.2: Maximum fractional energy transfer in neutron elastic scattering for different targets.

The probability of the neutron being scattered into $d\cos\theta$ about θ is given by Eq. 3.2 [96]

$$P(\theta_{cm})d\cos\theta = 2\pi \sin\theta_{cm} \frac{\sigma(\theta_{cm})}{\sigma_s} d\cos\theta_{cm} \qquad , \tag{3.2}$$

where $\sigma(\theta_{cm})$ is the differential cross section in the center of mass system and σ_s is the total scattering cross section integrated over all. Since $P(E_R)dE_R = P(\theta_{cm})d\theta_{cm}$ and

using Eq. 2.2, the probability to produce a recoil with energy E_R is expressed by

$$P(E_R) = \frac{(1+A)^2}{A} \frac{\sigma(\theta_{cm})}{\sigma_s} \frac{\pi}{E_n} \quad . \tag{3.3}$$

The differential cross section for elastic scattering in the center of mass system is isotropic, for hydrogen in the energy of interest as described in [97]. Therefore Eq. 2.2 implies that for single scattering, the expected proton recoil energy distribution has a rectangular shape.

However, some factors tend to distort the rectangular shape of the energy distribution of proton recoil:

- Carbon recoils produced by neutron elastic scattering do not directly affect the detector response, since the scintillation efficiency decreases for high $\mathrm{d}E/\mathrm{d}x$ particles and we have already seen that the maximal energy transferred is 28% of the incident neutron. However the "box shape" of the distribution of the energy deposited is affected because the neutron scattered from the carbon undergo a hydrogen scattering before escaping from the liquid scintillator. Since the incident neutron may lose from 0 and 28% of its initial energy, the corresponding effect on the detector response is a distortion of the box shape distribution from 72 to 100% of the maximum energy transferred into proton recoils.

- Multiple scattering is not negligible, especially when the liquid scintillator counter is large. Since such events occur within a time interval much shorter than the pulse shaping time, the scintillation light from all recoiling protons is summed up producing an increase of the average pulse. The summation of the multiple scattering events alters the expected response function by shifting the events towards the maximum energy deposit.

- Due to the finite resolution of the detector, the "sharp" feature of the energy distribution is smeared out.

A simplified Monte-Carlo simulation has been performed to estimate of multiple scattering in the LSC. The simulation takes into account the intrinsic efficiency of the LSC counter given by

$$\varepsilon = \frac{N_H \sigma_H}{N_H \sigma_H + N_C \sigma_C} \Big(1 - exp[-(N_H \sigma_H + N_C \sigma_C) d]\Big) \tag{3.4}$$

where all the quantities related to hydrogen and carbon are respectively denoted by H and C. The thickness of the detector is represented by d, N is the density number of the atoms and σ the corresponding scattering cross section. The neutron differential cross section in center of mass for hydrogen and carbon atoms have been retrieved from the National Nuclear Data Center [98]. The result shows that $\sim$75% neutrons do not scatter more than 3 times and that $\sim$39% neutrons interact with a hydrogen atom only once without undergoing carbon scattering.

3.3 The neutron generator

3.3.1 Reaction chamber

Figure 3.4: Picture of the neutron generator tube with its cooling fins on its outer sides (left) and the Al container (right).

Figure 3.5: Pictures of the neutron generator's "window".

The neutron generator is based on the inertial electrostatic confinement technology (IEC) which provides a linear geometry source to produce monochromatic neutrons. The concept of IEC was invented by Philo Farnsworth in the 1950s and later developed in the 60's by the physicist R.L. Hirsch to attain higher fusion rates via the DD and the DT reactions [99]. The reaction chamber produced by NSD-fusion consists of a hollow transparent grid cathode (-) surrounded by anode (+) at ground potential. By applying a very high voltage (10-100kV) and current at a low pressure gas (10^{-2} mbar), a glow discharge will be induced. The trajectory of a positive charge ion such as D^+ will be attracted and accelerated toward the central cathode in a volume of 36 mm $\times$ 25 mm. The cathode is a cage-like structure with vane elements aligned radially. This plasma

structure confines the ions at kinetic energies where fusion collision may occur with other ions or neutral deuterium provided by a getter disk. The fusion reactions shown in Eq. 3.5 and Eq. 3.6 take place isotropically, producing monochromatic neutrons at an energy of 2.45 MeV with a nearly equal probability to produce a proton. The fusion rate is controlled via the high voltage.

$$\mathrm{d} + \mathrm{d} \rightarrow {}^{3}\mathrm{He} + \mathrm{n}\ (2.45\,\mathrm{MeV}) \quad , \tag{3.5}$$

$$\mathrm{d} + \mathrm{d} \rightarrow \mathrm{t} + \mathrm{p}\ (3.02\,\mathrm{MeV}) \quad . \tag{3.6}$$

The reaction chamber assembly contains a hermetically sealed vacuum vessel and located inside an aluminum cylinder, which has cooling fins towards its outer side Fig. 3.4. Another Al cylinder about 3 mm thick directs the cooling air flow to the cooling fins. A neutron exit window, consists of a square of 45 mm side and 4.5 mm of thickness without fins, permits to minimize neutron scattering in the region where neutrons exit as it can be seen in Fig. 3.5.

3.3.2 Radiation safety and central control unit

Operation at 10^7 n/s without shielding around the neutron generator would increase the radiation dose of about 120 μS/h at a distance of 1 m from the neutron generator. The company which produced the neutron generator conducted an extensive study of the materials that could be used to shield the environment surrounding the neutron generator from the high radiation levels [100]. Water Extended Polyester (WEP) was selected for its good property to shield neutron radiation. On the other hand, WEP was found to be a poor material to shield the environment from photon radiation caused mainly by thermal neutron capture from hydrogen atoms, leading to 2.22 MeV γ-rays. X-rays from Bremsstrahlung within the neutron source electrode constitute an additional source of photon radiation. Therefore NSD-Fusion developed a Monte Carlo study using the MNCP framework (Monte Carlo N Particles). According to the results of this study, the final neutron shield was produced with a mixture of 75% of WEP and 25% of borate mineral colemanite ($CaB_3O_4(OH)_3H_2O$). A neutron shield 37 cm thick made of this mixture was provided by the company to surround the neutron generator. In addition, a 1 mm layer of lead was placed around the neutron shielding and 2 mm in front of the collimator to stop Bremsstrahlung X-rays.

For safety purposes a neutron dose rate meter, shown in Fig. 3.6, measured the equivalent ambient dose close to the safety cage in the laboratory, in order to limit the area access during the operation. This instrument has a high sensitivity of $\sim$3 counts per nSv [101] and the neutron generator has an interlock safety system that shuts it off as soon as the neutron/photon rate excesses a certain threshold. Furthermore, GEANT4 has been used to perform calculations to estimate the residual radiation present in the laboratory and its vicinity during the operation of the neutron generator at the theoretical maximum rate 10^7/s [102]. The simulation took into account the full geometry of the laboratory with its proper environment (wall, floor, window,...). The neutron shielding and a prototype of LAr chamber were both included, the latter being filled by LAr and surrounded

Figure 3.6: Neutron Probe LB6411 dose rate meter from Berthold.

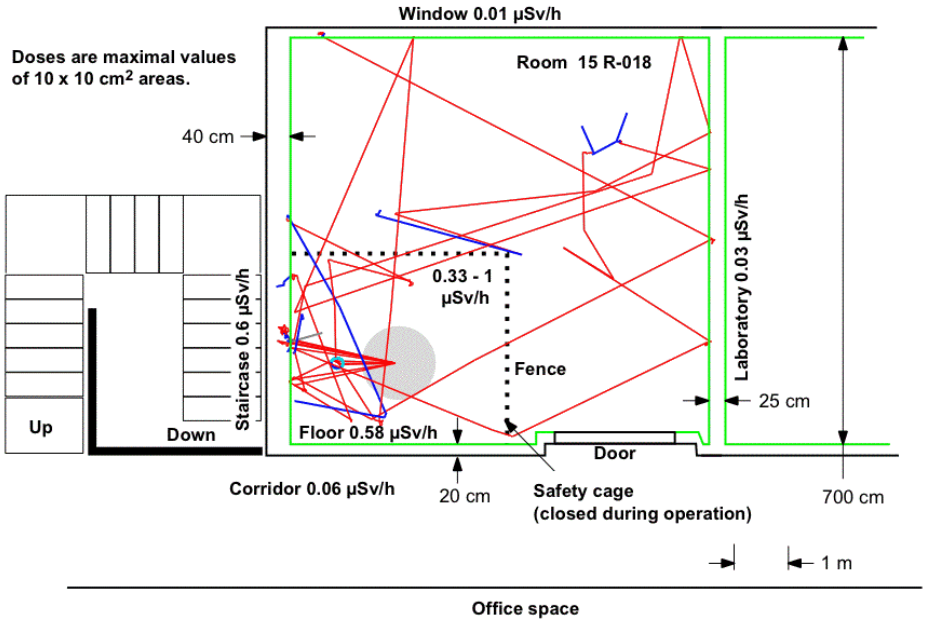

Figure 3.7: Calculated dose distribution inside and outside the laboratory. The grey circle represents the neutron generator (taken from [102]).

by a thick stainless steel container of 1 cm. The simulation results shown in Fig. 3.7, demonstrate that the residual radiation present in the laboratory and close to the safety cage was much lower than the dose authorized (2.5μSv) by the CERN's radio-protection service.

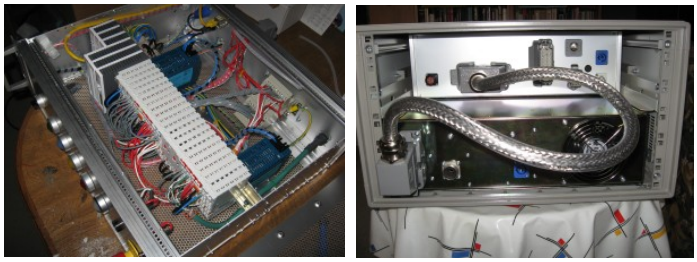

(a) (b)

Figure 3.8: Picture of the Central Control Unit. (a) Top view showing the connections to the I/O modules for the temperature, heater power, interlocks, warnings. (b) Back view showing the DC high voltage power.

A Central Control Unit (CCU) is responsible for controlling the temperature, heating power, interlocks. The CCU is an industrial PC provided with the appropriate input/output modules functions required to display the status and warning signals intended for the user, as shown in the picture Fig. 3.8. The CCU is located in the same rack as the DC high voltage in order to operate in conjunction with the DC high voltage.

A software package, based on a Proportional Derivative Controller (PID), has been developed by the company for the purpose of the running stability of the neutron generator. The software monitors the immediate plasma "ignition" and configures the system for normal regulation to achieve the preset target values of plasma voltage and current. The plasma current is regulated by the HV PSU that gets a target value from the CCU software, while the plasma voltage is regulated by the CCU software. This regulates the getter pump temperature which determines gas pressure for glow discharge.

3.3.3 Performances

Different measurements were performed in order to determine the neutron flux delivered by the neutron generator. According to the neutron generator manufacturer, the maximum voltage which can be applied to the cathode is 100 kV and 15 mA for the current, which corresponds to a flux of 10^7 n/s in 4π. The neutron flux intensity increases proportionally to $V^{2.8}$ (voltage) and to $I^{1.0}$ (current). The estimation of the rate has been done "on-line" using two different methods. The first method, a programmable Matlab routine written in the oscilloscope, is used to analyse the pulse shapes of the PMT, which is coupled to the LSC, and to count the neutron rate. The second method uses a NIM module called MPD4 which is a four channel pulse shape discriminator module to dis-

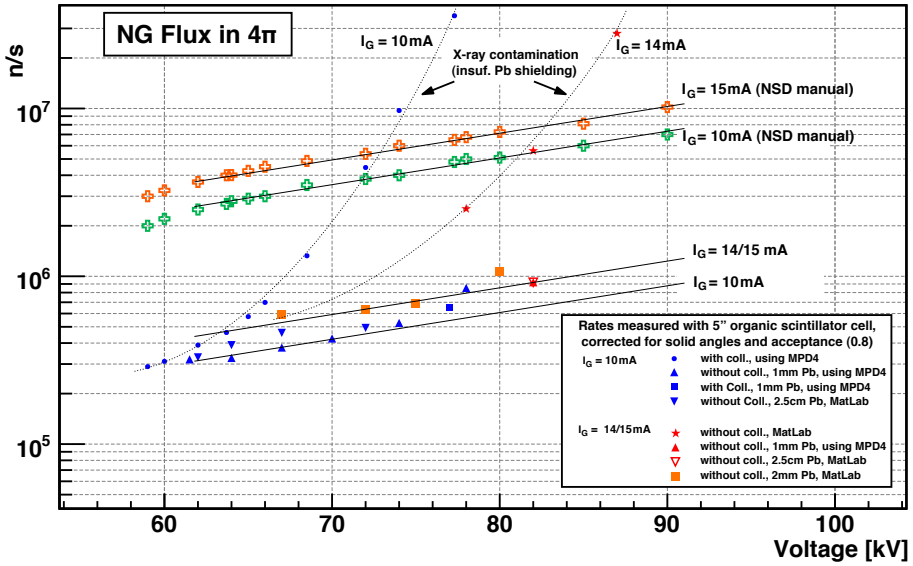

Figure 3.9: Measured neutron generator flux in 4π (bottom two lines).

criminate the neutron signal and a scaler module to count the neutron rate (see additional descriptions of MPD4 in Section 4.1).

A 5 inch LSC was used to measure the rate of the neutron generator and was placed at a distance of 45-50 cm from the neutron emission center with extra Pb shielding in order to stop X-rays from bremsstrahlung on the electrodes of the neutron generator. The neutron generator was operated at a fixed current with different voltage values. Measurements have been done with polyethylene (PE) collimator and without, and the rates obtained were corrected by the solid angles with an efficiency of about 80% of the LSC. The graphic in Fig. 3.9 shows the compilation of rate measurement to which have been added the values of the NSD-Fusion company in green (for I = 10 mA) and orange crosses (for I = 14/15 mA). We can clearly see the X-rays contamination at higher voltage, which can be easily suppressed by additional Pb shielding. The measurements showed a neutron flux lower than the expected (NSD-Fusion) values of about a factor of 7. The asymptotic aging effect and addition of certain processes might be responsible of the reduction of the measured neutron flux. The nominal flux in this measurement was measured to be $\sim 10^6$ neutrons per second in 4π.

3.4 Calibration of the LSC

When a neutron interacts with a hydrogen atoms, it generates light indirectly via elastic collision. For most organic scintillators such as anthracene or stilbene, the relative scintillation efficiency is described only by the Birk's law saturation ($\mathcal{L}_{\text{eff}} = f_l$ see Section 2.4.2), depending on the different types of incident particles and on energy as well. The aim of this section is to determine $\mathcal{L}_{\text{eff}}$ for proton recoil in order to see the feasibility of the

$\mathcal{L}_{\text{eff}}$ measurement in LAr by performing a neutron scattering experiment using the LSC as a target. In addition energy calibration for electron-recoil and detector resolution measurements were performed employing different radioactive sources.

3.4.1 Light Output Response

Several studies concluded that the light output response to γ-rays was linear above $\sim$125 keV$_{ee}$ [103], while for high ionizing particles such as hydrogen or alpha the equivalent energy (in MeV$_{ee}$) of the light output response was nonlinear as a function of the energy. In general in liquid organic, the number of scintillation photons produced by a proton recoil is about 10 times smaller than the one produced by an electron recoil for an energy

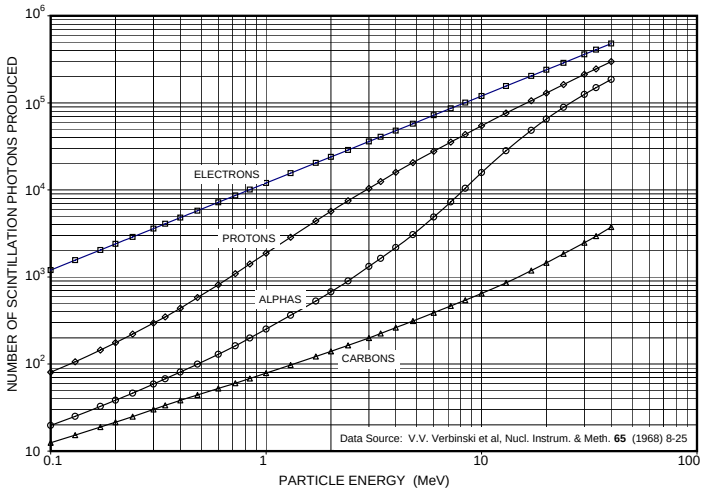

Figure 3.10: Light output from electrons, protons, carbon and α recoils as determined for the EJ301 scintillator detector.

range between 100 keV and 1 MeV as shown in Fig. 3.10 [104]. At higher energies this difference is less significant.

3.4.2 γ calibration

As mentioned in the previous section, the detector response to electrons is linear to a good approximation. It is therefore convenient to express an absolute light output in MeV$_{ee}$, which corresponds to 1 MeV for electrons and several MeV for protons. Hence the importance to calibrate the LSC using γ-rays source before performing a calibration for proton recoils.

To quantify the amount of scintillation induced by a recoiling electron in the LSC, a calibration gain of the PMT coupled with LSC has been performed. The single photo-electron (p.e.) response measurement was performed using thermal photons produced by thermionic electrons that are spontaneously emitted by the photocathode of the PMT.

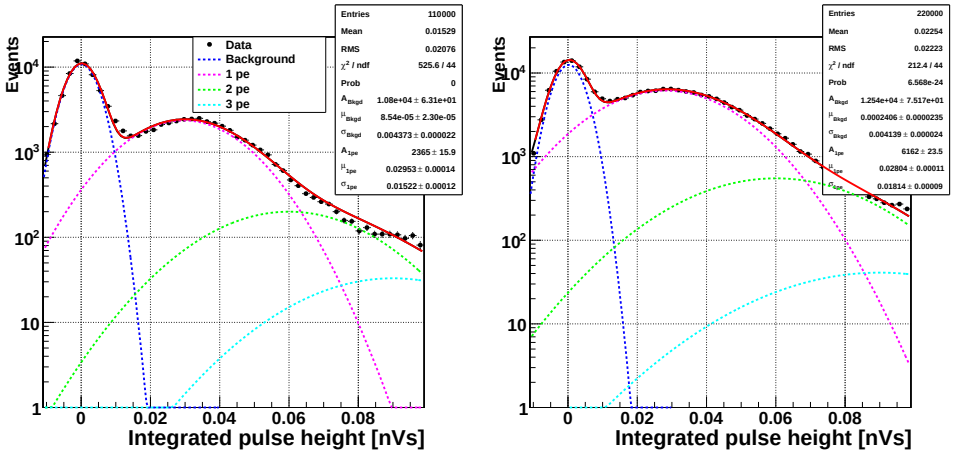

(a) (b)

Figure 3.11: Example of integrated pulse height distributions obtained with thermal photon for 3" (a) and 5" (b) LSC. The black dotes are the experimental data. The red curve is the fit from Eq. 3.4.2 and the other dashed curves represent the noise (blue), 1 p.e. (pink), 2 p.e. (green) and 3 p.e. (blue ocean).

The plots in Fig. 3.11 show the Integrated Pulse Height (IPH, see the definition in Section 4.2.2.2) of the PMT response for different sizes of LSC. They were fitted with:

$$f(x)_{respPMT} = A_0\, e^{-\frac{1}{2}(\frac{x-\mu_0}{\sigma_0})^2} + A_1\, e^{-\frac{1}{2}(\frac{x-\mu_1}{\sigma_1})^2} + A_2\, e^{-\frac{1}{2}(\frac{x-2\cdot\mu_2}{\sqrt{2}\cdot\sigma_2})^2} + A_3\, e^{-\frac{1}{2}(\frac{x-3\cdot\mu_3}{\sqrt{3}\cdot\sigma_3})^2} \quad (3.7)$$

A_i is the amplitude, μ_i is the mean value expressed in "nVs" and σ_i is the standard deviation for $i = 0, 1, 2$, and 3 corresponding to the background, single, double and triple photons. The sum of four Gaussian functions is sufficient to estimate precisely the mean value for the single photoelectron response.

Several radioactive γ-rays sources were used to calibrate the liquid scintillators for different size. Information about photon energy, decay mode, lifetime and branching ratio of all the radioactive sources used are listed in Tab. 3.3. Due to the small value of the atomic number Z of the atomic compounds contained in the LSC, the Compton scattering is the dominant interaction above ~100 keV, while below this energy, the photoelectric interaction is the main process.

The position of photopeaks in the energy deposit spectrum for the absorbed photons is determined by the mean value from the Gaussian function fit, as shown in Fig. 3.12(a). For the Compton spectra the "sharp" Compton edge is smeared out due to finite energy resolution by the energy resolution effect, making difficult to ascribe a unique point to the peak position of the Compton edge. According to A.A. Naqvi [105], the approximation of the true position of the Compton edge is assumed to be at the half-height of the smeared Compton edge in the integrated pulse height. The way of determining the true Compton edge leads to an uncertainty of 4% [106]. Fig. 3.12 (b) shows the Compton spectra for

Source	Decay mode	$T_{1/2}$	Energy [keV]	Branching ratio[%]	Compton edge[keV]
^{109}Cd	EC	461.4 d	22	84	-
^{241}Am	α	432.6 y	59.54	35.9	-
^{22}Na	Annihilation	2.6 y	511	90	341
^{137}Cs	β^-	30 y	662	85	478
^{22}Na	β^-/EC	2.6 y	1275	100	1061

Table 3.3: Details of the radioactive sources used for γ calibration.

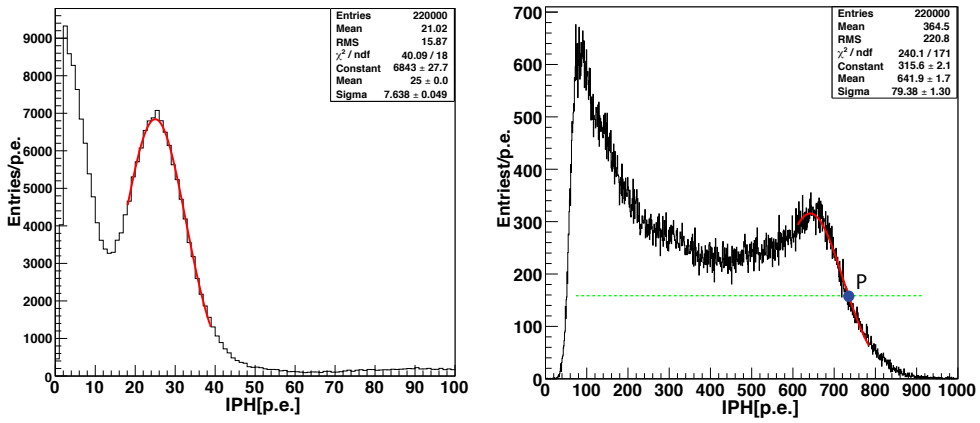

(a) (b)

Figure 3.12: Integrated pulse height of γ-rays from a 22 keV ^{109}Cd source (a) and from a 662 keV ^{137}Cs source (b) in the 3"LSC. The position of the 478 keV Compton edge is shown by the intersection between the green line (half height) and the Gauss function in red (point P).

the Cs source measurement. The intersection between the fit, performed with the half gauss distribution, and the green dashed line, representing the half height of the smeared Compton edge, indicates the position of the true Compton edge (P).

The measurement of the light output as a function of the energy using different γ-rays sources listed in Tab. 3.3 is shown in Fig. 3.13. Above ∼300 keV a linearity was observed within 0.22%, while at 22 keV and 60 keV, the mean values of the integrated pulse height decrease by about 7% and 5% respectively.

3.4.3 Energy resolution measurements

An estimation of the energy resolution of 3" and 5" LSC was performed using the γ-γ coincidence technique described in [107] for energy regions for which the Compton scattering is the dominant interaction. The γ-γ technique is based, in this work, on the detection of backscattered γ-rays coming from the LSC under study. A BaF crystal with

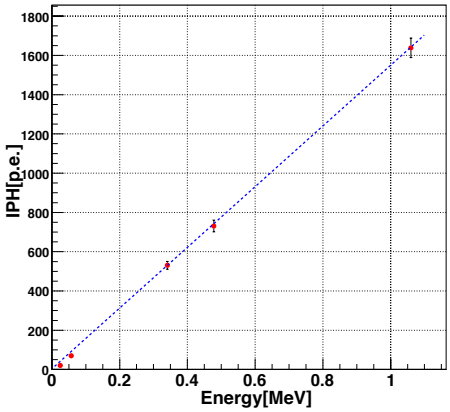

Figure 3.13: Integrated pulse height in photoelectrons (p.e.) as a function of energy. The blue dashed line is used to guide the eye.

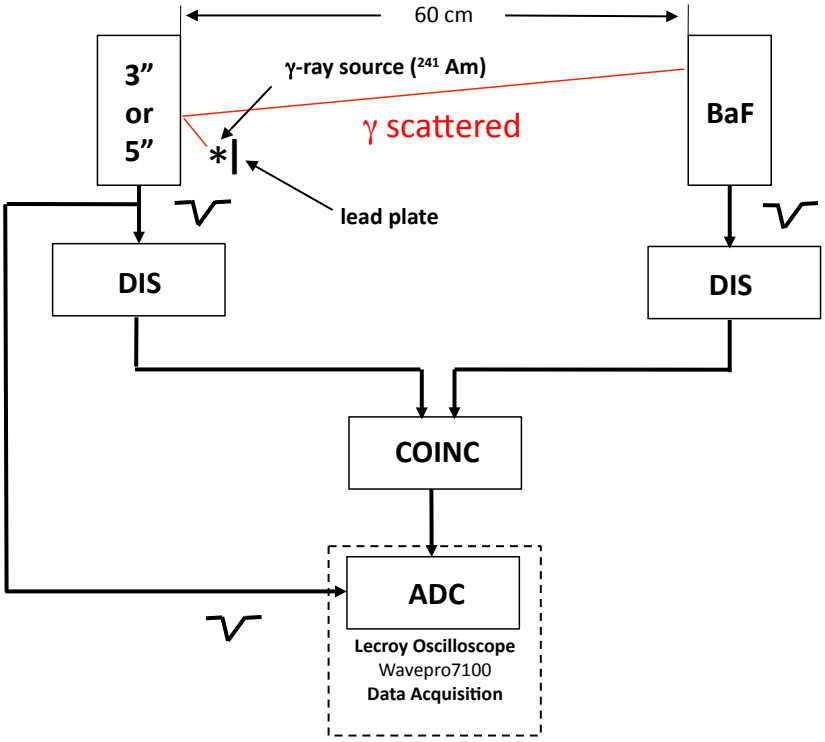

Figure 3.14: Electronics block diagram of the experimental setup to measure the energy resolution of the LSC.

a diameter of about 8 cm was used to detect backscattered γ. This crystal scintillator provides a good time resolution of the order of hundreds ps.

The experimental setup with associated electronic block diagrams is illustrated in Fig. 3.14. The monoenergetic γ sources were placed 2 cm from the LSC under study at a distance of

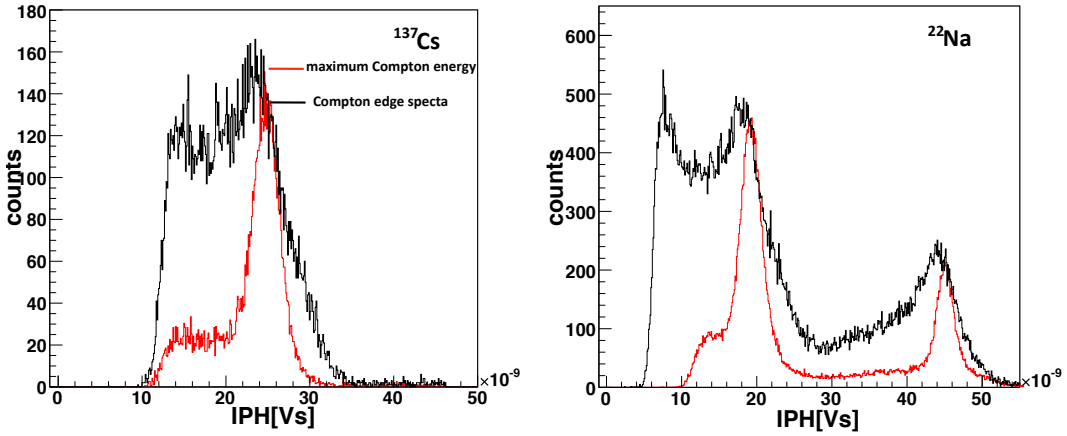

(a) (b)

Figure 3.15: Integrated pulse height of maximum Compton energy electrons (red) and the Compton spectra (black) superimposed from ^{137}Cs (a) and ^{22}Na (b) for the 5" LSC.

about 1 cm from the center of the edge of the LSC. ^{22}Na and ^{137}Cs γ-ray sources with an active area of 5 mm and 8 mm, respectively, were used to produce Compton spectra for the energy resolution measurements above 300 keV. A 2 cm thick lead plate was located just behind the source to shield γ-rays going directly to BaF crystal. The two detectors were separated by a distance of 60 cm.

For each scintillator detector, appropriate energy windows were set on the discriminator unit in order to select back scattered gamma events. Pulse height signals corresponding to the maximum energy Compton of the LSC under study are gated by the discriminator unit with coincidence condition. The data are subsequently recorded by the digital oscilloscope Lecroy Wavepro 7100. Fig. 3.15 shows the resulting histogram of the Compton maximum energy spectrum (gated), compared to the typical Compton edge spectrum (ungated). The two maximum energy Compton peaks of 341 keV and 1062 keV from the ^{22}Na radioactive source are displayed in the same histogram in Fig. 3.15 (b). A Gaussian fit was applied on the gated spectrum to estimate the position of the Compton edge E_c and to extract the Full Width at Half Maximum (FWHM) given by

$$\Delta E_c \approx 2.355 \times \sigma \quad , \tag{3.8}$$

where σ is the width of the Gauss distribution. The energy resolution of the detector is defined as the ratio

$$R_c = \frac{\Delta E_c}{E_c} \quad . \tag{3.9}$$

G. Dietze and H. Kleinn described in [108] an approximation of the energy resolution for the smeared Compton spectrum given by the relation

$$R_{sc} \approx 1.5(E_h - E_m)/E_h \quad , \tag{3.10}$$

E_m is the energy corresponding to the maximum amplitude of the smeared Compton edge and E_h the position of the half height. Tab. 3.5 shows the result of the energy resolution measurement for the 3" and 5" LSC. The energy resolution R_c of the 3" determined via the gated spectrum varies from 24.6% to 7.2% over the energy range of 0.34 MeV to 1.06 MeV. At lower energy range − between 22 keV to 60 keV where the photoabsorption is dominant − the energy resolution decreases from 72% to 53.1%. E_h is always higher than E_c and the difference between these two parameters reduces as the energy increases. At 0.31 MeV, E_h is 11.2% higher than E_c and at 1.06 MeV it is only 4.7% higher. The position of E_h with respect to E_c does not only depend on the detector resolution but can differ according to the phototubes and electronics used for the same type of LSC.

For the 5" LSC, the values of the energy resolution are slightly higher than for the 3" detector and vary from 25.4% to 7.9% between 0.34 MeV and 1.06 MeV. It is well known that the energy resolution of the detector deteriorates as the detector volume increases. On the other hand, the deviation of E_h compared to E_c is higher than that of the 3" detector. This effect increases as well with the detector volume and can be explained by multiple scattering affecting on the deviation of E_h from E_c. Over this same energy range, E_h deviates from 13,8% to 5%.

Electron energy [MeV]	$\Delta E_c/E_c$ [%]	$1.5(E_h - E_m)/E_h$ [%]	$(E_h - E_c)/E_c$ [%]	Detector size
0.022	72.0±3.2	-	-	3"
0.060	53.1±2.4	-	-	3"
0.341	24.6±1.7	20.8±2.5	11.2±1.7	3"
0.478	16.2±1.0	18.2±1.8	6.9±1.2	3"
1.062	7.2±0.5	7.0±0.8	4.7±0.7	3"
0.022	74.7±3.4	-	-	5"
0.060	55.8±2.6	-	-	5"
0.341	25.4±1.5	27.0±2.8	13.8±1.6	5"
0.478	16.8±1.2	22.7±2.3	7.0±1.4	5"
1.062	7.9±0.7	8.6±1.0	5.0±0.8	5"

Table 3.4: Energy resolutions for the 3" and 5" LSC EJ-301.

In Fig. 3.16 values of the energy resolution $\Delta E_c/E_c$ as a function of the energy of the 5" LSC are displayed and are fitted with an empirical approximation Eq. 3.11 [109]

$$\frac{\Delta E_c}{E_c} = \sqrt{\alpha^2 + \frac{\beta^2}{E_c} + \frac{\gamma^2}{E_c^2}} \quad , \tag{3.11}$$

where α corresponds to the locus dependent light transmission from the scintillator to the photocathode (geometrical influences) and β is the statistical fluctuation of the light production and amplification. All the noise contribution due to the photo-multiplier (dark current) and electronics amplifiers are defined by γ. The parameter β, which is

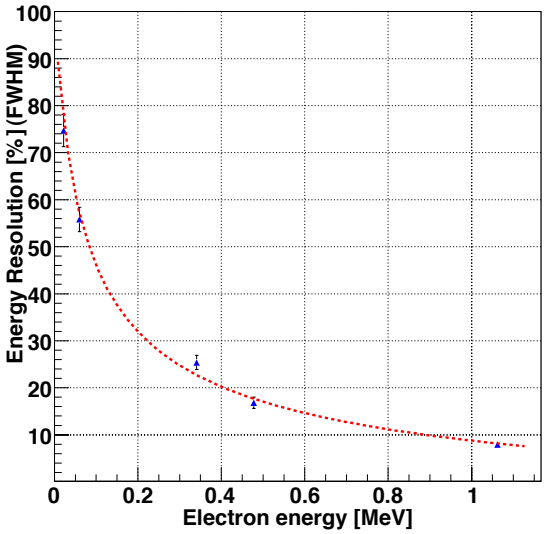

Figure 3.16: Energy resolution vs. electron energy for the 5" detector.

very sensitive to the scintillator light output, mainly determines the energy resolution of the LSC. The parameter γ was set at 0.2 for a better stability of the fit, as observed in several results [105, 108, 110]. The values of the resolution parameters obtained for both detectors are listed in Tab. 3.5 with other measurements performed by A.A. Naqvi *et al.* [110] and G. Dietze and H. Klein [108] with NE-213 scintillators which are the same type of EJ-301 LSC. The value of β is 6% higher for the 3" scintillator compared to Dietze

Detector size	Present work			A.A Naqvi et al			Dietze and Klein		
diameter [inch]	α	β	γ	α	β	γ	α	β	γ
3	1.2	10.6	0.2	1.5	11.0	0.2	1.2	10.0	0.2
5	1.4	11.6	0.2	1.5	13.5	0.2	-	-	-
10	-	-	-	-	-	-	5.6	18.0	0.2

Table 3.5: Resolution parameters of 3", 5" and 10" LSCs.

and Klein's data but lower of about 4 % than that of A.A. Naqvi *et al.*, showing a better energy resolution.

3.4.4 Calibration of the proton recoil energy

A measurement has been performed with neutron sources to study the light output for proton-recoils in the scintillator counter. The method employed rests on the neutron scattering experiment with the time of flight (TOF) technique, and uses a neutron generator (NG) producing monochromatic energy neutrons as described in Section 3.1. The NG irradiates the detector 3" LSC, inducing nuclear recoils. The 3" LSC detector under

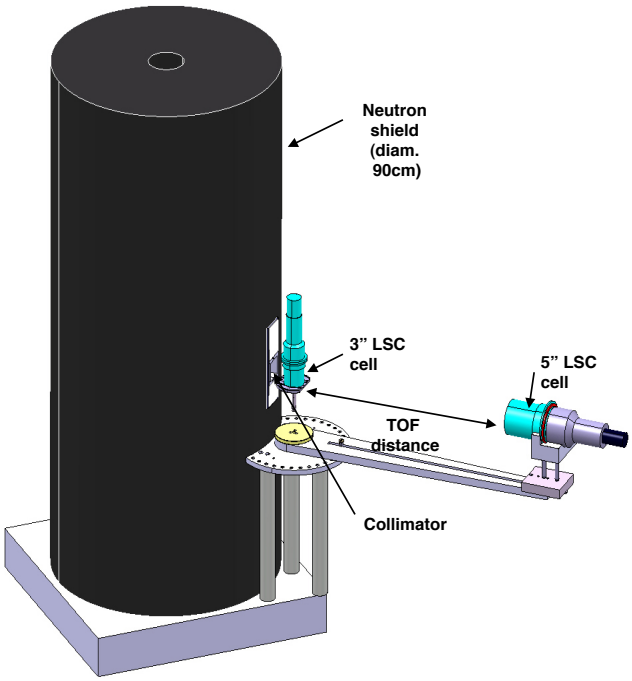

Figure 3.17: Sketch of the neutron scattering experiment for proton-recoil calibration in LSC.

investigation, is located at a distance of 50 cm from the source. Scattered neutrons are detected by a 5" LSC placed at a distance of 69 cm. The neutron TOF measurement between the 3" and the 5" LSC provides information about the energy of the outgoing neutrons. A sketch Fig. 3.17 shows the experimental setup for the proton recoils calibration.

A coincidence is required between signals in 3" and 5" LSC within a time window of 350 ns. With a time resolution of 200 ps, it is possible to use ^{22}Na or cosmic muons to calibrate the absolute time t_0 (where TOF = 0 ns) for a neutron TOF measurement. Cosmic muons are close to the speed of light passing through both detectors with a traveling time about 2.5 ns. To avoid a calibration time run with the ^{22}Na source, the trigger setting was such that cosmic muons could be recorded if they arrived to opposite direction with respect to neutron beam during the neutron scattering measurement. Even if horizontal cosmic muons are quite rare ($\sim$0.5 events/min), a data tacking of 1 day is sufficient to perform such a calibration. The TOF distribution for the cosmic muon sample is therefore a combination of two Gaussians, one for each traveling direction. The center of the two-Gaussian structure provides a good estimation of the t_0 parameter.

Neutron scattering data were acquired at 3 different angles, 30°, 40° and 60° which respectively correspond to recoil energies of $612.5 \pm 18.5, 1012.3 \pm 30.6, 1837.5 \pm 55.6$ keV. The uncertainty on the recoil energy values are estimated by propagating the uncertainty in the angle (half a degree) and is mostly due to mechanical alignment and to the detector size. Thanks to their excellent n/γ pulse shape properties, an offline discrimination tech-

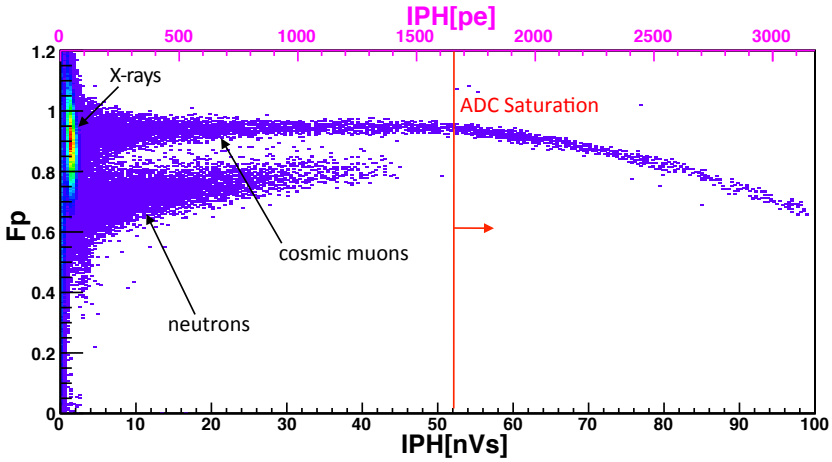

Figure 3.18: Two dimensional histogram of F_p vs integrated pulse height in units of nVs (bottom x-axis) and converted into photo-electrons (upper axis) for the LSC. The upper band and the lower band correspond to proton recoils from neutron scattering, and electronic recoils from X-rays (Bremstrahlung generated by the NG) and cosmic muons, respectively. The energy of X-rays is typically 50 keV$_{ee}$. The decrease in F_p for the electronic recoils band at higher energy is caused by ADC saturation.

nique based on the charge integration is adopted to identify neutron events [111]. The parameter F_p (see Section 4.2.2.5) used to identify the type of interaction is calculated via the ratio of the integration of fast component (∼20 ns) over the total integration of the signal (130 ns). The scatter plot of F_p as a function of the charge integration in units of nVs, reported in Fig. 3.18, shows two separated components: electron recoil events populating the region above $F_p = 0.8$, and proton recoil events mostly, concentrated at $F_p < 0.8$. Also the contamination by X-ray Bremstrahlung is observed around 50 p.e. (∼30 keV$_{ee}$). This source of background labeled "accidental" coincidence is due to a photon interacting in the 5" LSC detector in coincidence with an unrelated neutron detected by the 3" target cell. This accidental contamination by the Bremsstrahlung radiation close to the cathode of the NG chamber contributes to half of the data taking, but can be suppressed by applying a F_p cut on the 5" LSC, supposed to detect the scattered neutron. TOF distributions are displayed in Fig. 3.19 for neutron-like events and accidental X-rays background after selection of the type of interaction in the 5" LSC using $F_p \leq 0.75$. The typical characteristic of the flat TOF distribution of the accidental background is readily identifiable in the data (b). On the left part of this distribution, situated near TOF = 0 ns, is the peak from cosmic muons used for the absolute time calibration. In (a) for neutron-like events, the tail of the TOF peak, which is overlapping the remaining accidental background, is due to the multiple scattering inside detectors and to the interactions outside of the detectors.

An acceptance time window of about 10 ns (4 ns on the left and 6 ns on the right around the peak) is chosen to select proton recoil events. According to a simplified MC simula-

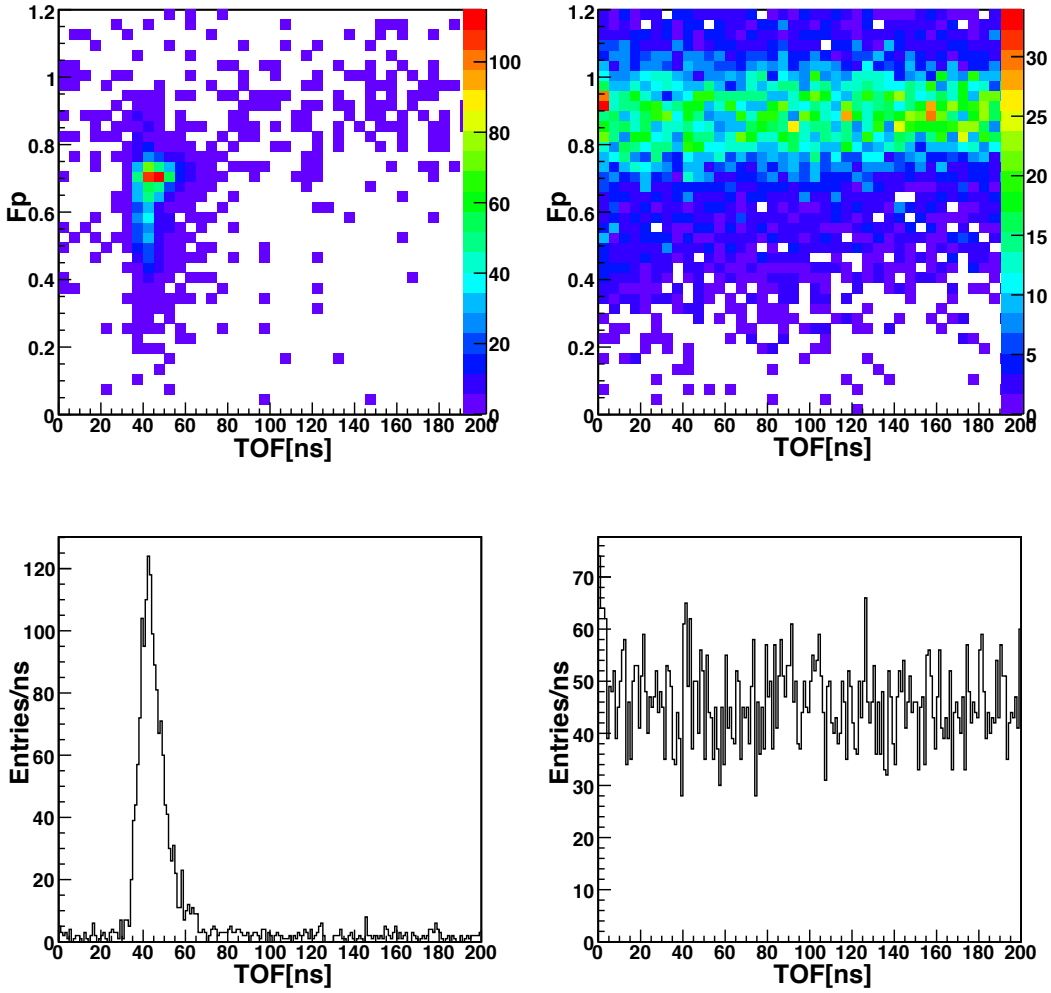

(a) (b)

Figure 3.19: Ratio F_p vs. time of flight (TOF) in the 3" LSC and its corresponding TOF projection after applying the F_p cut in the 5" cell at 40°. A typical neutron TOF is displayed in (a) for $F_p < 0.75$, while (b) shows the TOF distribution after selecting the electronic recoils band in the 5" cell.

tion, the TOF cut used leads to a contamination of multiple scattering of about 5%. After applying the cuts mentioned previously (F_p and TOF) to this simplified analysis, only 2-4% of events are selected. Single-scatter neutrons spectra are fitted with a Gauss distribution in order to extract $\mathcal{L}_{\text{eff}}$ for proton recoils ($\mathcal{L}^{\text{p}}_{\text{eff}}$) in LSC, as shown in Fig. 3.20(a), for the angle 40°. Results of each angle are listed in Tab. 3.6. The uncertainties are the combination of statistical and systematic errors mentioned previously.

Results of $\mathcal{L}^{\text{p}}_{\text{eff}}$ for proton recoils determined in this work are plotted in Fig. 3.20(b) with the superimposed measurement of J.Hong *et al.* [112] exploring recoil energies from 50

θ[°]	E_r [keV]	$\mathcal{L}_{eff}^{p}$
30	612.5±18.5	0.079±0.010
40	1012.3.5±30.6	0.139±0.012
60	1837.5±55.6	0.207±0.008

Table 3.6: Values of $\mathcal{L}_{eff}^{p}$ obtained for this measurement.

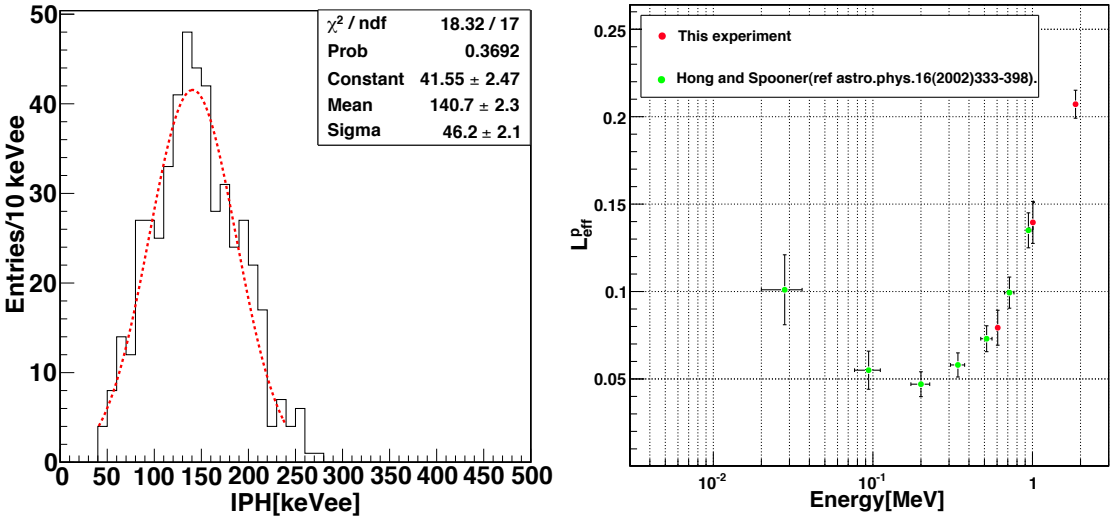

(a) (b)

Figure 3.20: (a) p-recoil energy distribution at 40°. The x-axis is already converted into keV_{ee}; (b) $\mathcal{L}_{eff}^{p}$ results.

keV to ∼1 MeV. The results obtained in this work confirm the tendency that $\mathcal{L}_{eff}^{p}$ increases above hundreds of keV as already observed by J.Hong *et al.* .

Despite the "simple" trigger settings preventing from measuring $\mathcal{L}_{eff}$ at lower energy (about tens of keV), a reconstructed neutron generator spectrum was made possible by adding the deposited energy in the target cell calibrated with the data from Verbinsky *et al.* [104], and the energy from the TOF information $E_{rec} = E_{3"} + E_{TOF}$. A 5th polynomial function was used to parametrize the data from Verbinsky in order to retrieve the energy deposited in the 3" LSC from the light output. The systematic uncertainties from the estimation of the energy deposited in the 3" LSC and the energy measured from the TOF are ∼3% and and ∼4%. Fig. 3.21 illustrates the reconstructed neutron generator spectrum with an uncertainty of 5% and a FWHM of about 30%. The tail below the peak at 2.47 MeV corresponds to lower incoming neutrons which have interacted with the collimator.

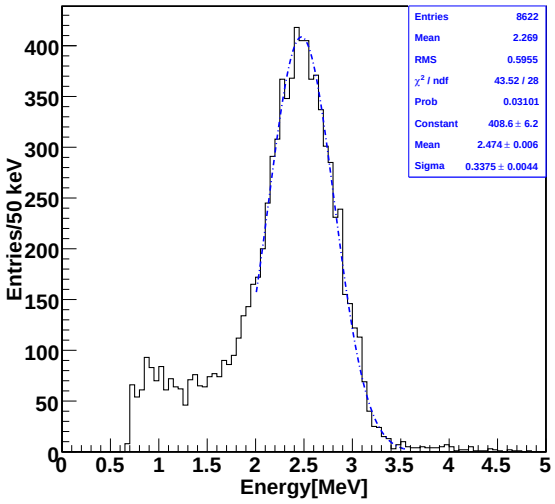

Figure 3.21: Reconstructed neutron generator spectrum.

3.5 Liquid argon cell

Measuring the $\mathcal{L}_{\text{eff}}$ in LAr at low energy is quite a challenge. The designing of the LAr cell detector for the neutron scattering experiment has to take into account several factors :

- High light detection efficiency to measure nuclear recoil at low energy thresholds.
- The volume of the detector should be large enough to collect a reasonable amount of statistic in a proper timescale for this measurement.
- Minimizing the multiple scattering in the LAr active volume.
- Minimizing the interaction before and after that neutrons scattering in the active volume. The neutrons scattered by the non-active LAr volume or the surrounding materials, between the NG and the LAr cell and between the LAr cell and the LSC, are a source of systematic uncertainty affecting the $\mathcal{L}_{\text{eff}}$ measurement.

The LAr cell is shown in Fig. 3.22. The scheme consists of two PMTs separated by a distance of 47 mm forming a cylindrical sensitive volume of approximately 0.2 ℓ. The two PMTs Hamamatsu R6091-01 have 12 dynodes and a quantum efficiency of ∼15% (see Appendix C for the technical datasheet paper). To decrease the resistivity of the biakali photocathodes for operation at LAr temperature (∼86 K), the PMTs contain platinum underlay. The surface of the PMTs was coated with a TPB[1]/Paraloid mixture. The stainless steel cylinder surrounding the PMTs has an inner diameter of 133 mm and a

[1]tetra-phenyl-butadiene

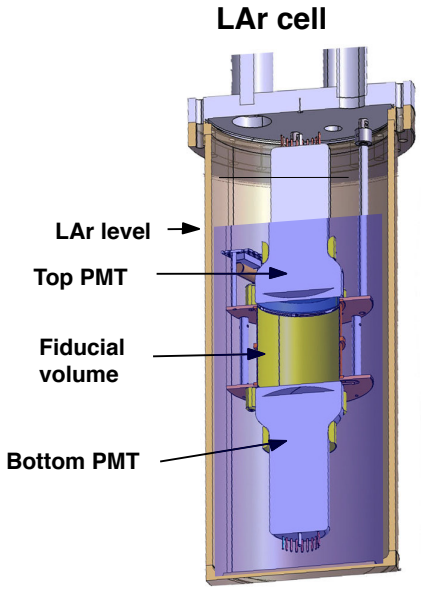

Figure 3.22: Sketch of the LAr cell.

thickness of 1.5 mm. Between the PMTs, the active area is defined by a thin Al cylinder holding a reflector coated with a wavelength shifting (WLS) made of Tetratex to shift the VUV scintillation light to a longer wavelength. The Tetratex foil has been chosen to be used as a reflector according to the measurement in [113]. The surface density of TPB covering the reflector is $1.0 \pm 0.1 \mathrm{mg/cm^2}$. In order to perform measurement at zero electric field, the Al cylinder is polarized at the same voltage as the photocathode of the PMTs. The detector is filled with condensed pure argon gas (GAr) 6.0 containing less than 0.5 ppm of H_2O, 0.1 ppm of O_2, 0.1 ppm of H_2, 0.1 ppm of CO_2, and 0.1 ppm of CO. Before filling the LAr cell, several days were necessary to pump its volume in order to clean the surface from impurities which may contaminate pure GAr. The typical vacuum reached in the chamber was of about 5×10^{-6} mbar using a 60 ℓ/s turbopump. The condensation of GAr and the recirculation system will be explained in the following section. Platinum resistors (PTs) sensors were connected along the detector side to monitor the LAr level inside the cell, while vacuum and gas pressure of the system were read out by different pressure sensors. A slow control program written in Labview was used to monitor and record the thermodynamical parameters of the system during the operation. A blue LED ($\lambda = 390$nm) connected to an optical fiber was put in the inner vessel for the gain calibration. The optical fiber is used to transport the light toward the active area of the LAr cell. A $^{210}_{82}$Pb source of $\sim$40 Bq activity is used to analyse the pulse shape for α recoils in LAr. This source was placed in the center of the active volume and emits α with 5.3 MeV and β with a Q-value of 1.16 MeV as described in [114] and represented by the decay chain in Fig. 3.23. A thin thread made of copper, soldered to the spherical source with a diameter of 1mm, is screwed to the support of the reflector on the other extremity. The

source was coated with a few tens of μm plastic (Paraloid B-72) to spread the energies of αs over a broad range.

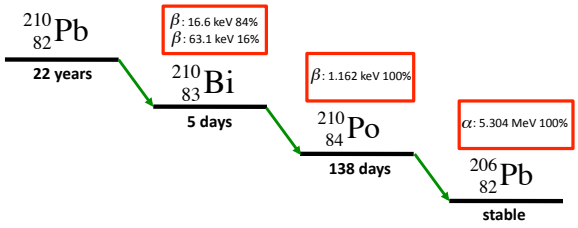

Figure 3.23: Decay diagram of the internal $^{210}_{82}$Pb source.

3.6 Cryostat and gas system

For continuous operation, a cryogenic system and gas system have been connected to the detector. The gas is condensed on the top of the chamber at the cold head of a Sumitomo CH210 cryocooler with a nominally cooling power of about 80 W (Fig. 3.24(a)), driven by a Sumitomo F-70H helium compressor [115] which is designed to provide high pressure helium gas to cryogenic refrigerators of about 13 bars. The cryocooler is a two-stage

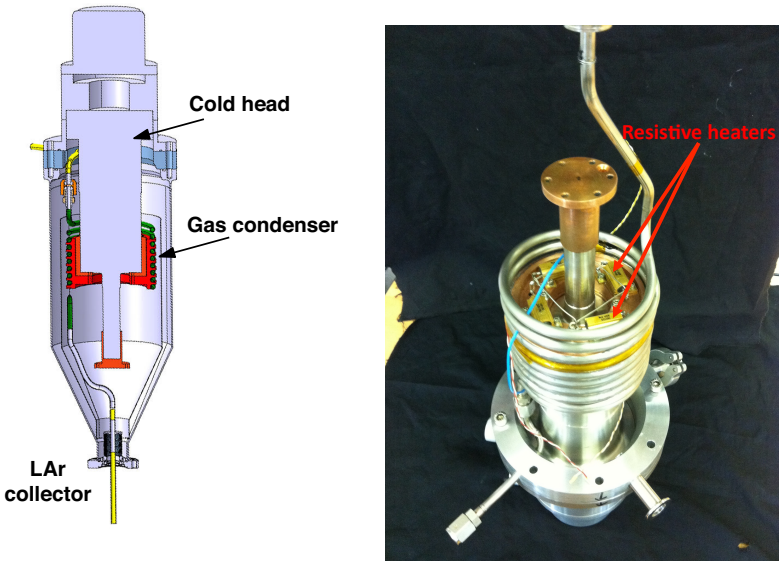

(a) (b)

Figure 3.24: (a) side view sketch of the cryocooler; (b) view of the first stage heating station with connected resistive heaters.

cryogenic refrigerator that operates on the Gifford-McMahom (GM) refrigeration cycle

and supplies 110 Watts at 77 K on the first stage heat station and 6 Watts at 20 K on the second one. A copper cylinder surrounding the first stage heat station is implemented in order to facilitate the thermal exchange with the coil pipe where GAr is condensed (gas condenser). This tube is made of stainless steal to avoid impurities such as water or oxygen.

In order to maintain permanently the temperature between the solidification and the boiling point of argon (respectively 85 K and 87 K at 1 atm), four resistive heaters were placed on the first stage heat station of the cryocooler and PT sensors were connected along the coil pipe for cooling power monitoring as it can be seen in Fig. 3.24(b). A temperature controller using a PID system released by a LabView program reads out and regulates the temperature of the coldhead at a desired value by controlling the heaters. The precision of the temperature controller is of about 10 mK. The current provided to the heaters is ensured by a TTi TSX 35 10 programmable PSU based on the GPID interface. The typical power produced by the heaters to maintain the temperature window required for the liquefaction, is about 50 W as illustrated in Fig. 3.25. The cryostat provides a good stability of cooling power for continuous operation. Fig. 3.26 shows the temperature evolution in the coldhead and in the LAr detector. An Outer Vacuum Chamber (OVC) is used to isolate the cryogenic refrigerator from the room temperature and the vacuum in OVC is kept at about 1×10^{-5} mbar.

The cooldown is generally a delicate step, the GAr flux during this step needing to be adjusted in such a way as to obtain a pressure in the detector between 1000-1250 mbar in order to avoid the LAr collector gets frozen at the end of the stainless steal tube where LAr comes out. Usually, the filling phase lasts about 6 hours and the amount of LAr used for this step is of about 3.5 ℓ assuming a constant pressure of 1080 mbar and a constant

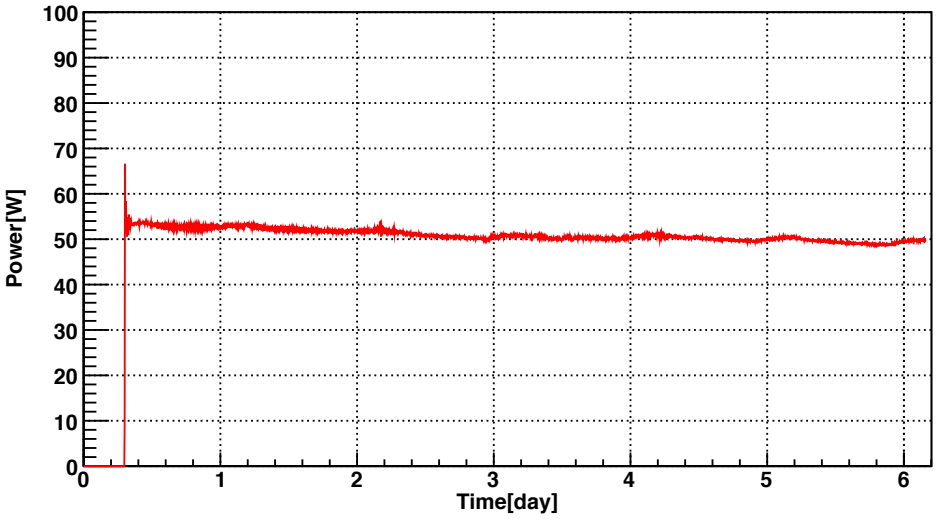

Figure 3.25: Power delivered by the heaters during the recirculation phase lasting roughly over 6 days. The resistive heaters were turned off during the filling phase.

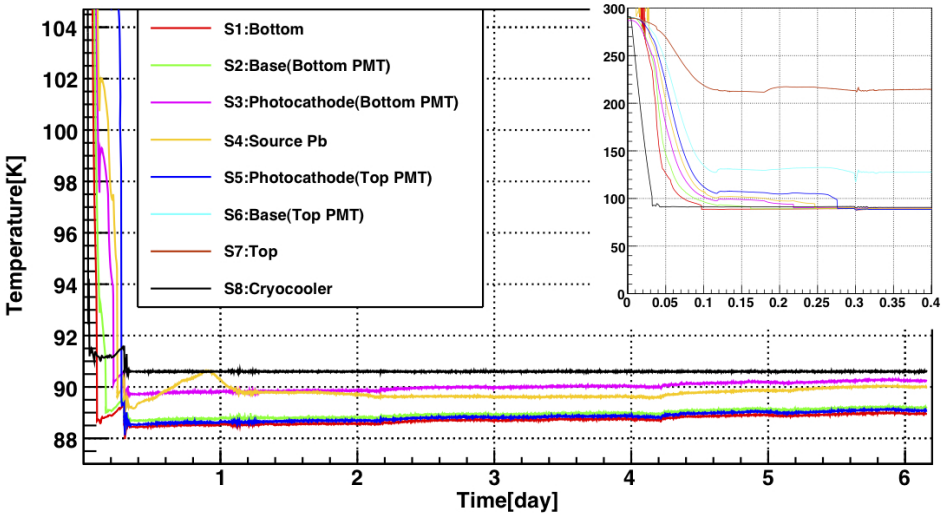

Figure 3.26: Temperature evolution over days of the different sensors as a function of time when filling with LAr (inset plot) and during the recirculation phase.

temperature of 88 K. The evolution of the PT sensors during the filling phase shows a clear drop when they are completely immersed in LAr. The GAr condensation stops 30 min after that LAr level reaches the temperature sensor S5 (just above the photocathode of the Top PMT).

The frame of the gas system has been machined in the CERN's machine workshop and uses Swagelok for gas line connections. A picture of the gas system along with its schematic diagram are shown in Fig. 3.27. During the cool down phase, GAr is transferred from the GAr 6.0 bottle to the LAr chamber through the pressure regulator R2 used to regulate the GAr flux. The path of the GAr during the filling phase is represented by red arrows. Once the LAr filling is completed, the pressure regulator of the gas system is closed, and the GAr starts being recirculated through the system via a recirculation pump and by closing the valve V5. The GAr recirculation through the gas system is represented by black arrows. The GAr purification is insured by two purification cartridges OXISORB-W which reduce the O_2 and H_2O levels to respectively < 5 and < 30 ppb respectively, according to the manufacturer MEISSEIR [116]. The cartridges are mounted in parallel in order to avoid high resistivity. The gas system includes also a coil tube (Converter LAr/GAr) which is used to warm the LAr to convert it into GAr. Additional valves are used to isolate the ^{83}Rb source (V8 and V9) and to isolate the volume detector from the gas system (V3 and V4).

Measurements of the evolution of LAr purity are plotted in Fig. 3.28 showing a decrease of the purity as a function of time. This behavior is explained by the fact that the pipe connected in the detector volume and supposed to suck out GAr, does not entirely remove impurities which remain at the bottom in the liquid phase of the LAr cell. The degradation of the purity can be solved by the implementation of a tube to suck out

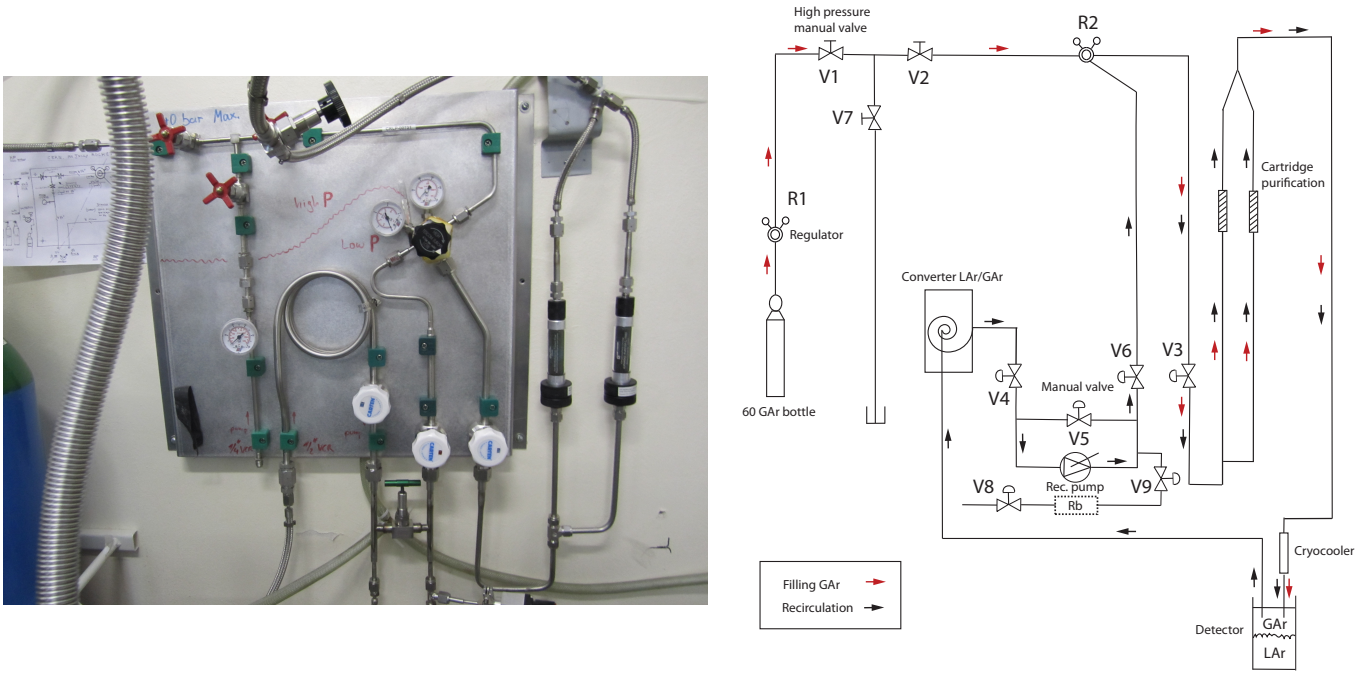

Figure 3.27: The gas system responsible for Ar filling, recirculation and purification. The arrows show the direction of Ar during filling in red, and during recirculation in black.

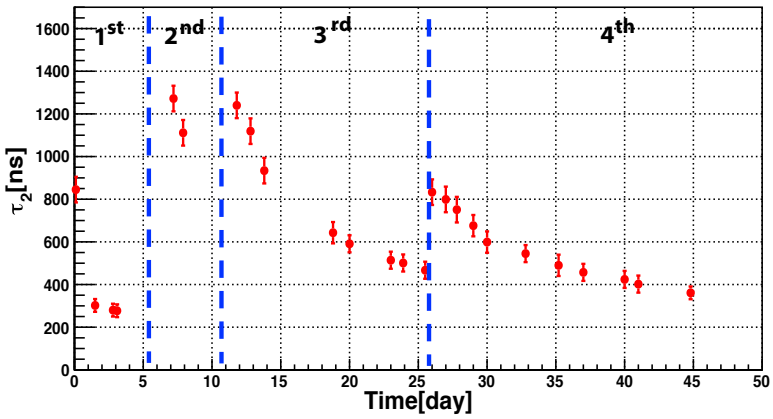

Figure 3.28: Lifetime of the triplet state τ_2 as a function of time. The blue dashed lines correspond to repeated cooldowns.

impurities in the liquid phase rather than in the gas phase.

Conclusions

A neutron scattering experiment was designed to study $\mathcal{L}_{\text{eff}}$ in LAr. A monochromatic neutron generator was used to induce nuclear recoils, delivering a maximal intensity flux of about 10^7 n/s in 4π. The neutron scattered are detected by EJ-301 organic liquid scintillators which has been calibrated for electron and proton recoils. A LAr detector consisting of two PMTs with an active volume of 0.2 ℓ has been built according to the requirement needed to conduct a precise $\mathcal{L}_{\text{eff}}$ measurement at low energy.

Chapter 4

Data Reconstruction

In this chapter I will present the methods employed for the data reconstruction in order to measure $\mathcal{L}_{\text{eff}}$. Studies on the scintillation pulse shape necessary for a background discrimination in LAr dark matter detectors are also treated.

4.1 Data acquisition system

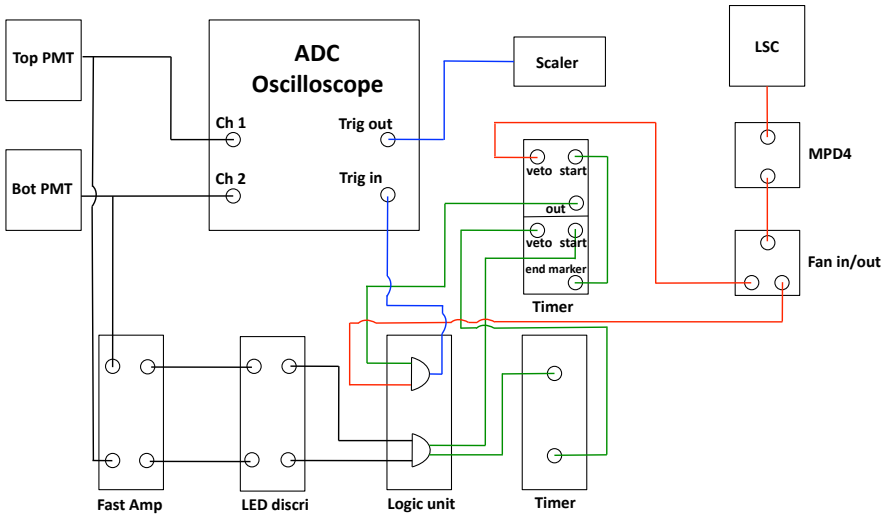

Figure 4.1: Schematic of the DAQ system.

The PMTs read the signal produced in the LAr cell. The analog signal from both PMTs is split into two inputs, low and high gain signals of a 10-bit digitizer LeCroy Oscilloscope WavePro 735Zi DSO. The low and the high gain signals are then matched offline. This procedure allows to increase the dynamic range to fully reconstruct α-particles without FADC saturation [117] and to measure the single photoelectrons with high sensitivity. In order to avoid artifact due a mismatch in the high and low gain

channels, a cross check is performed by comparing the integrated pulse height vs. the pulse height obtained from this method and using a suitable dynamic range for several γ sources. In general the accuracy of the signal matching between the high and low gain is $\sim$2%. The data are collected with 5000 points at 1GS/ns with 500 ns pre-sample for pedestal subtraction. Data are stored into a hard disk and then analyzed offline. Fig. 4.1 shows a schematic of the DAQ system. The two signals from the PMTs are fed into a CAEN N979 $\times$10 amplifier before being fed into a leading edge discriminator CAEN N840 where the threshold has been set at -7 mV, corresponding to 0,5 photoelectrons. The logic signals are then connected to a CAEN N405 coincidence unit which is set to "AND" for the coincidence between the two signals of the PMT channels. N93B timing units are used for time coincidence of about 30 ns between the two signals. Neutron signals detected in the LSC are selected using an analog pulse shape discriminator module Mesytec MPD4 [118]. This module, also designed for BC-501 and NE-213 LSC, determines the ratio of fast to slow component of the scintillation light output and was set to accept the neutron band during the neutron scattering experiment. The MPD4 module is suitable for a precise TOF measurement in the context of our experiment. Time jitter of the trigger signal of this module was investigated since it could induce an error in the TOF measurement. The FWHM of the trigger signal distribution was estimated to be $\sim$0.2 ns lower than a couple ns corresponding to the transition time in the EJ-301 LSC. The selected EJ-301 signal are fed into a linear fan in/out module which has two identical outputs necessary to feed to the timer and logic units. Events are accepted with a time delay of 200 ns between the signal in LAr detector trigger and the signal in LSC. This trigger setting was used during the data taking in December 2011. Instead, in June 2011 a programmable trigger logic in the oscilloscope was used for the trigger in coincidence between the signals from the LAr detector and the LSC.

4.2 Framework and analysis technique

4.2.1 Reconstruction software

A dedicated Framework written in C++ is designed for the neutron scattering experiment in LAr. Fig. 4.2 shows the structure of the framework in which the data production and subsequent processing is divided into three steps:

- In the first step, the signals from the PMTs are stored by the LeCroy oscilloscope in binary files with 1000 events. Each data set of files is grouped in a Run number.

- A program written in C++ using the ROOT analysis package [119] converts the binary files into ROOT files in which low and high gain traces are combined for each PMT channel. A configuration file (.chcfg file) containing all the information of the Run is created (number of files, time stamp, events per file, number of samples per event, etc.).

- In another workspace (Analysis directory), a software developed for the data processing (data production) reads the ROOT files and the configuration in order to produce an output ROOT file containing relevant variables necessary for the analysis (pulse height, integrated pulse height, time of the maximum pulse, etc.).

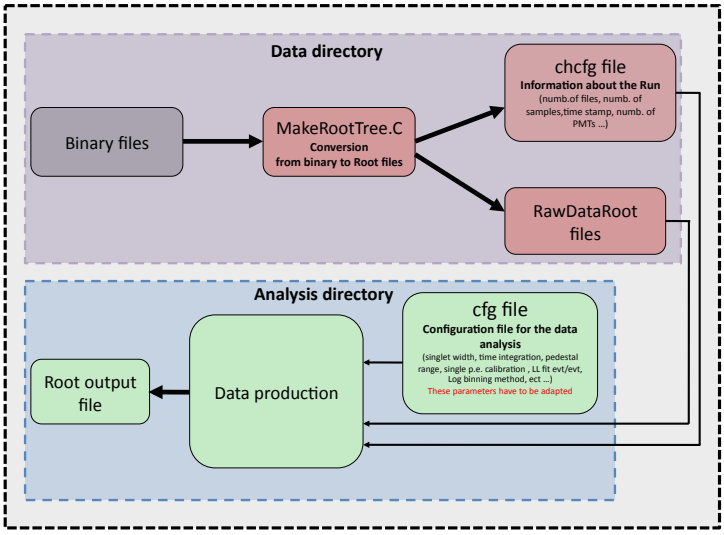

Figure 4.2: Raw diagram of the analysis software.

The user can set different options in a configuration file (.cfg file) in order to choose the method for the analysis (integration time, single photoelectron calibration, likelihood fit event by event, logarithmic binning method, etc.) and to set other parameters.

4.2.2 Description of techniques and variables for data analysis

4.2.2.1 Cluster finding algorithm

Offset or low frequency noise can affect the signal reconstruction. As mentioned earlier, 500 ns before the occurrence of the trigger are recorded to define the pedestal to be subtracted, in general calculated as the average value of all the sample in the pre-trigger region. However, this method is limited by the single photoelectron contamination leading to a wrong evaluation of the pedestal. To avoid single photoelectron contamination during the pedestal calculation, an algorithm for cluster finding is developed and based on an iterative method, as illustrated in Fig. 4.3. This method can be explained in three steps:

- **1.** The mean of the pedestal $\overline{m}_{ped}$ and the standard deviation σ_{ped} in the pre-trigger range of the signal trace are calculated according to Eq. 4.1, where U_{i} is the amplitude of the signal at a given sample i (or at a given time in ns since the

recording speed is 1 Gs/s) and N is the number of samples:

$$\overline{m}_{ped} = \frac{\sum_{\mathrm{i}}^{N} U_{\mathrm{i}}}{N} \text{ and } \sigma_{ped} = \sqrt{\frac{1}{N}\left(\sum_{\mathrm{i}}^{N} U_{\mathrm{i}}^2\right) - (\overline{m}_{ped})^2} \quad . \tag{4.1}$$

- **2.** Samples with an amplitude higher than $\overline{m}_{ped} \pm 3 \cdot \sigma_{ped}$ are accounted as a cluster and those within 10 ns before and after the cluster are added to the cluster in order to insure that all the samples from the photoelectron signal are taken into account.
- **3.** A new $\overline{m}_{ped}$ and σ_{ped} are calculated with samples that are not considered as a cluster. The loop is repeated from the step number 2 until the time interval does not need to be reduced by 1% compared to the one from the previous loop.

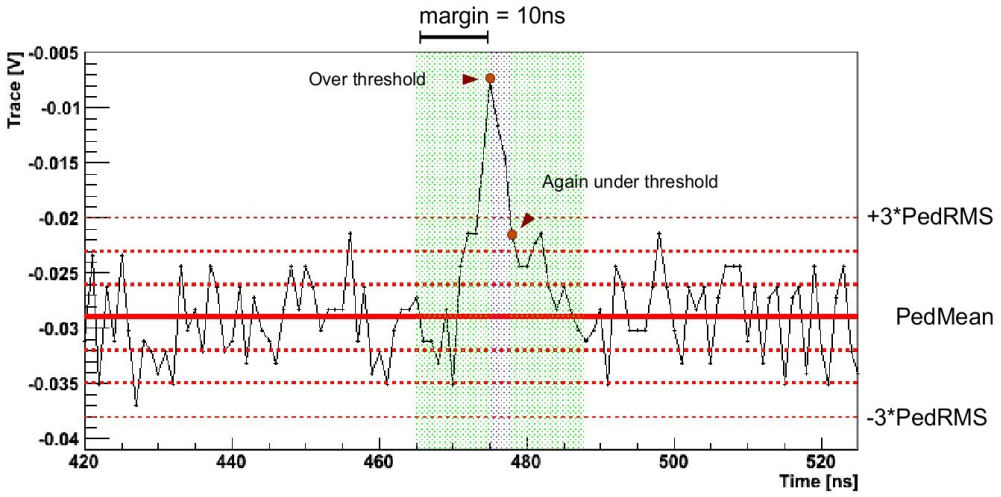

Figure 4.3: Illustration of the cluster finder algorithm.

Fig. 4.4 shows the histograms displaying the distribution of the standard deviation of the pedestal σ_{ped} in logarithmic scale, calculated by a simple mean without the cluster finding algorithm (a) and using the cluster finder algorithm event by event (b). The distortion in the tail of the distribution in (a) is caused by the contamination generated by photoelectrons in the pedestal region. The contamination in the pedestal region represents, here, 1.5% of the data. The distortion gets reduced when applying the cluster finder in (b), resulting in a decreased contamination of about 2 orders of magnitude.

4.2.2.2 Integrated pulse height

The software looks for the time position of the highest amplitude of the signal denoted by t_{peak}. The integration of the digitized signal called integral pulse height (IPH) is

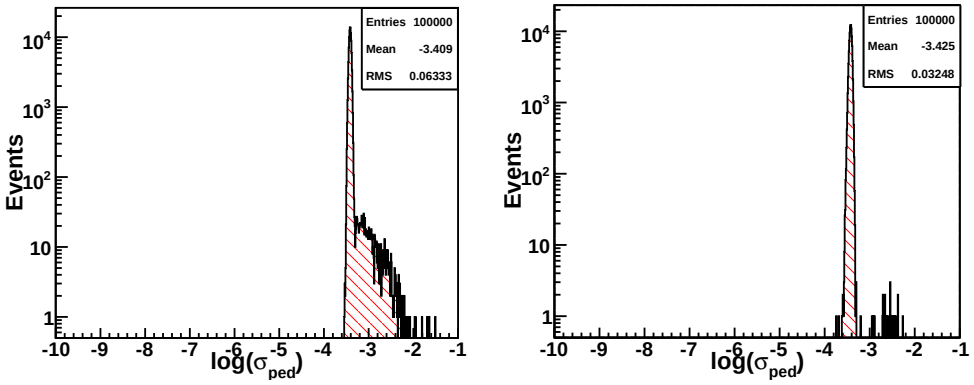

(a) (b)

Figure 4.4: (a) distribution of the event by event standard deviation in logarithmic scale obtained without the cluster finder algorithm; (b) same distribution applying the cluster finder algorithm for the photoelectron suppression in the pedestal region.

defined as:

$$IPH = IPHA + IPHB = \sum_{t_{peak}-20ns}^{t_{peak}+30ns} U(t) \cdot \Delta t + \sum_{t_{peak}+31ns}^{t_{peak}+3\cdot\tau_2} U(t) \cdot \Delta t \tag{4.2}$$

where $U(t)$ is the amplitude of the signal, τ_2 is the decay time of the triplet state and Δt is the sampling timing ($\Delta t = 1$ ns according to the sampling speed). The integration of the first 50 ns of signal is sufficient to integrate the prompt signal and is denoted by $IPHA$. The time integration for the slow part of the signal is chosen at $3{\cdot}\tau_2$ which contains most of the part of the triplet state ($IPHB$). All these parameters are expressed in nVs. Since the accumulation of the charge collected on the anode of the photomultiplier (Q_{anode}) is proportional to the amount of photoelectrons detected ($N_{p.e}$), the latter quantity can be determined from the value of the calibration of the photomultipliers according to the following formula:

$$N_{p.e} = Q_{anode} \cdot \frac{R_{int}}{k_{cal}} = \int_{t_{peak}-20ns}^{t_{peak}+3\cdot\tau_2} \frac{Udt}{R_{int}} \cdot \left(\frac{R_{int}}{k_{cal}}\right) = \frac{\sum_{t_{peak}-20ns}^{t_{peak}+3.\tau_2} U(t) \cdot \Delta t}{k_{cal}} = \frac{IPH}{k_{cal}} \tag{4.3}$$

where k_{cal} is the integrated pulse height in nVs per photoelectron. Therefore the conversion of IPH from nVs into p.e. is made possible if k_{cal} is known by performing the gain calibration of the photomultipliers.

4.2.2.3 Gain calibration

PMT calibration can be performed in two ways. The first way is to generate single photoelectron pulses using a LED (Light-emitting diode) and the second one is to extract isolated single photoelectron pulses from the tail of the slow component of the scintillation light distribution as shown in Fig. 4.5. The last method makes the calibration significantly easier and faster, especially for the neutron scattering experiment in which the expected event rate is rather low. For each single peak found, information about the integration, pulse height, peak time and the width of the peak are recorded. A comparison of the gain calibration has been carried out with a LED powered by 10 ns pulses of 2.05 V with a rise/fall time of 3 ns in order to produce a mean value of numbers of photons of about 0.87.

It is well known in the case of pulsed source of light that the number of photons interacting in the photocathode is distributed as a Poisson variable. However, only a part of the photons is converted into electrons (quantum efficiency) through a random binary process. The convolution of these two processes gives a Poisson distribution:

$$P(\mu; n) = \frac{\mu^n \mathrm{e}^{-\mu}}{n!} \tag{4.4}$$

which describes the probability that n photoelectrons will be observed with μ, the mean number of photoelectrons. Moreover, if the amplification factor of the first dynode is large enough (> 4) compared to the following ones, the response of the multiplicative dynode system can be approximated by a Gauss distribution [120]:

$$G_1(x) = \frac{1}{\sigma_1 \sqrt{2\pi n}} \exp\left(- \frac{(x - Q_1)^2}{2\sigma_1^2} \right) \tag{4.5}$$

where x is the charge, Q_1 is the mean value of the charge at the PMT output for one

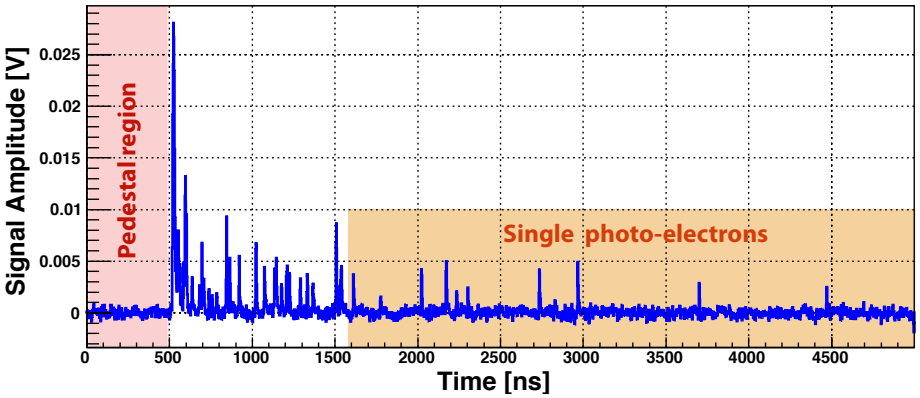

Figure 4.5: Signal induced by an electronic recoil on the bottom PMT. The red area shows the pedestal region used to correct the offset and the region in orange contains single photoelectrons in the tail of the signal used to calibrate the PMTs.

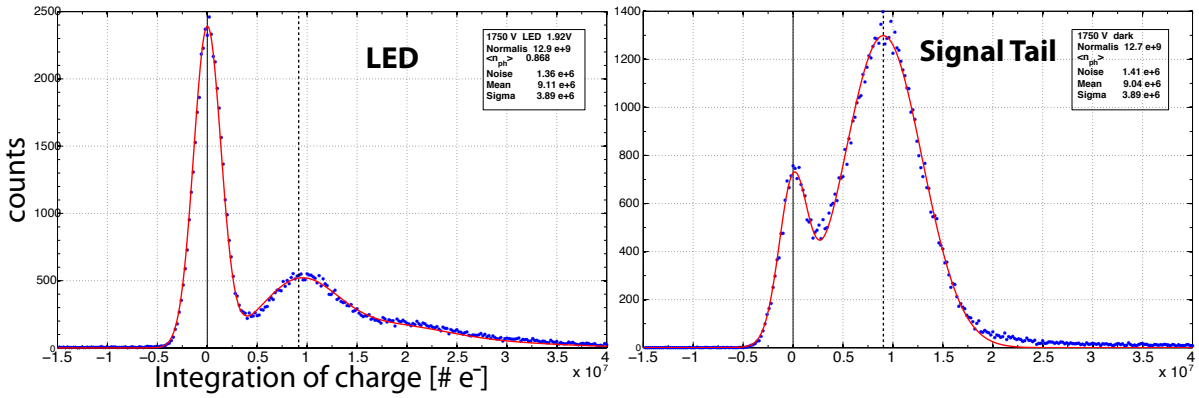

Figure 4.6: Distribution of integration of charge from LED data (left) and the same distribution using photoelectron pulses from the tail of the signal (right).

electron collected by the first dynode and the corresponding standard deviation of the charge distribution is denoted by σ_1. When more than one photoelectron is collected at the first dynode, the charge distribution expressed in Eq. 4.5 can be generalized by a convolution for n one-electron case:

$$G_n(x) = \frac{1}{\sigma_1\sqrt{2\pi}}\exp\left(-\frac{(x-Q_1)^2}{2n\sigma_1^2}\right) \quad . \tag{4.6}$$

For an ideal noiseless PMT, the response is described by the convolution of Eq. 4.4 and Eq. 4.6:

$$\begin{aligned} S_{ideal}(x) &= P(n;\mu) \otimes G_n(x) \\ &= \sum_{n=0}^{\infty} \frac{\mu^n \mathrm{e}^{-\mu}}{n!} \frac{1}{\sigma_1\sqrt{2\pi n}}\exp\left(-\frac{(x-nQ_1)^2}{2n\sigma_1^2}\right) \quad . \end{aligned} \tag{4.7}$$

Fig. 4.6 shows the integrated pulse height of the photoelectrons distribution taken from the LED (left side) and the tail of signal (right side). The fit on the spectrum obtained from the LED is the sum of a Gauss function allowing to describe the pedestal and the Eq. 4.7. Whereas only the Gauss function from the Eq. 4.5 is used to fit the photoelectron spectrum from the tail of the signal because the probability to detect a double photoelectron is negligible. The vertical black dashed line shows the mean value of the charge Q_1 collected by the last dynode. Due to the contamination of the double photoelectron, the mean value of the charge obtained by the spectrum with the LED for a single photoelectron is higher though it is consistent within 1% compared with the one obtained from the tail of the signal.

Calibration of PMTs has been performed run by run and results of calibration factors k_{cal} as a function of time are displayed in Fig. 4.7. In Season01 a temperature colder on the photocathode of the PMTs might be responsible for the step observed on the values of k_{cal} between 15 and 20 days after the first cooling down. The difference between the

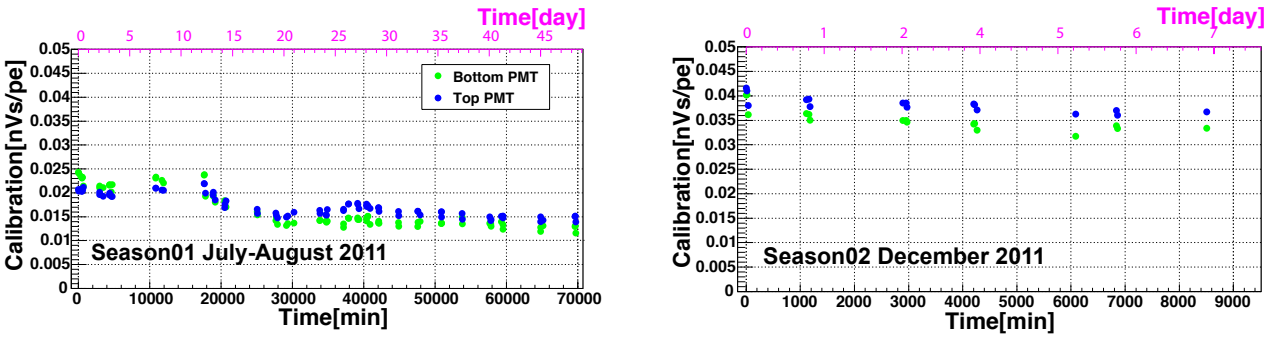

Figure 4.7: Values of calibration factors k_{cal} for both PMTs as a function of time for two running periods.

mean values of k_{cal} before and after this step is ∼37% and ∼23% for bottom and top PMT respectively. In Season02, values of k_{cal} are larger because the high voltage applied on the PMTs was higher in order to improve signal over noise.

4.2.2.4 Signal combination of top and bottom PMT

Within the framework of pulse shape study, it is important to sum the signal of both PMTs. The combination of both traces must take into account any time shift due to the different cable lengths inducing delay between the recorded signals of the PMTs. This time correction is applied by performing a measurement of the peak time of signals generated by a synchronous LED. The distribution of the peak time shown in Fig. 4.8 is compared between both PMTs. The average of the mean value obtained by fitting with a Gauss function the peak time distribution of both PMTs is taken as a reference time. Therefore the signals are combined according to the time correction t_{corr}, which is the difference in time between the reference time and the value from the Gaussian fit on the peak time distribution. Typically the values of t_{corr} is 1 ns for the bottom PMT and −1 ns for top PMT.

The calibration factor has to be taken into account in order to scale the signals according to the light collected by the PMT for a precise combination of the signals. The signals $s_{top}[t]$ and $s_{bot}[t]$ are then combined as following:

$$S_{comb}[t] = \frac{s_{top}[t + t_{corr}]}{k_{top}} + \frac{s_{bot}[t + t_{corr}]}{k_{bot}} \tag{4.8}$$

where $S_{comb}[t]$ represents the resulting combined signal (expressed in p.e./ns) of the gain calibrated signals of both PMTs , namely k_{top} and k_{bot}.

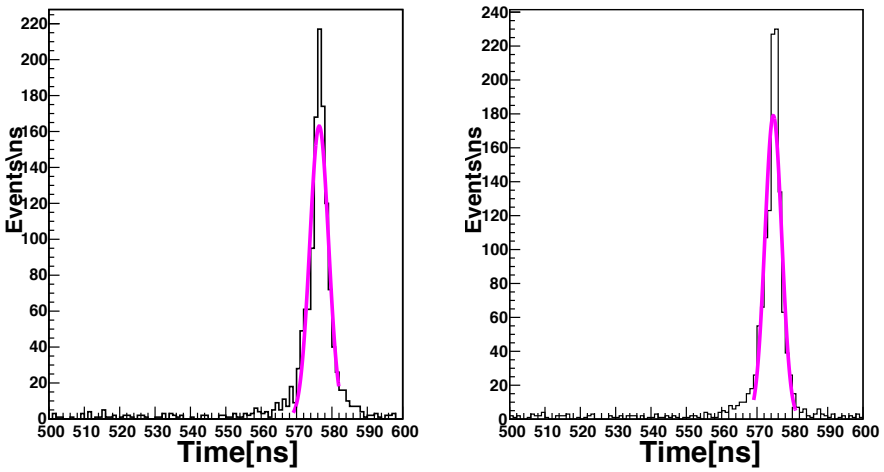

Figure 4.8: Peak time distributions from LED pulser for bottom PMT (left) and top PMT (right).

4.2.2.5 Pulse shape discriminator parameter: Prompt fraction and component ratio

Due to the properties of the LAr, a discriminant variable called prompt fraction (F_p), can be defined as the ratio $IPHA$ over IPH where an integration threshold is applied. This simple technique is sufficient to perform a particle identification as shown in Fig. 4.9.

The general shape of the signal recorded by the DAQ can be described as:

$$\mathcal{F} = \mathcal{G}(t,\sigma) \otimes \left[\mathcal{H}(t-t_0) \cdot \left(\frac{A}{\tau_1} \cdot e^{\frac{t-t_0}{\tau_1}} + \frac{B}{\tau_2} \cdot e^{\frac{t-t_0}{\tau_2}} \right) \right] \tag{4.9}$$

where A, B are the contribution of the singlet ($\sim IPHA$) and triplet state ($\sim IPHB$), τ_1 and τ_2 being their corresponding lifetime. The reference time or trigger time is defined by t_0 and σ corresponds to the experimental time resolution. $\mathcal{H}(\mathrm{t}-\mathrm{t}_0)$ is the Heaviside function with the condition 0 for $t < t_0$ and 1 otherwise. The relative contribution of the singlet state decays to the total scintillation light is defined as the component ratio (CR). The advantage of this method for an event by event particle identification is that it includes the correct exponential behavior of the time distribution of the singlet and the triplet states without any threshold dependence. On the other hand, the disadvantage of this method is the increase of the computation time and the complexity of the analysis, which requires a preliminary step to determine the values of the starting parameters for the likelihood fit and the lack of statistics in the low energy regime.

Values of CR obtained by using Eq. 4.9 on the average pulse shape (Fig. 4.10) and mean values of F_p are listed for different types of particles in Tab. 4.1 at the same range selection. The data were taken with the monochromatic 2.45 MeV neutron source and the internal source of ^{210}Po.

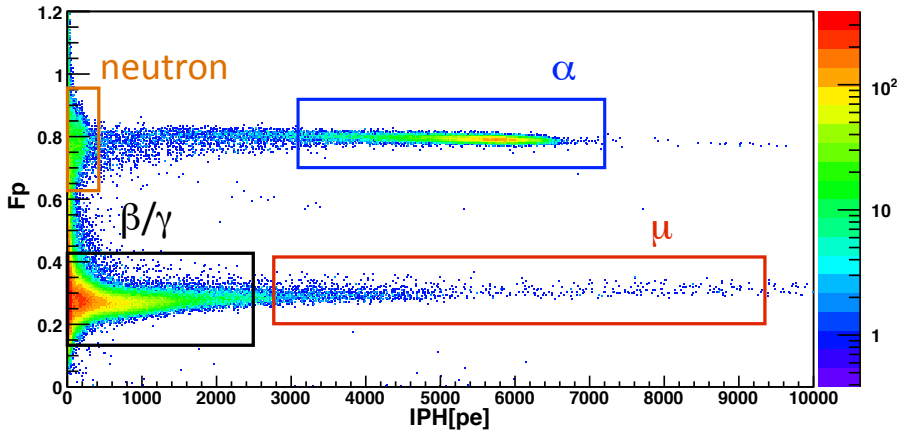

Figure 4.9: F_p as a function of the scintillation light for different types of particles.

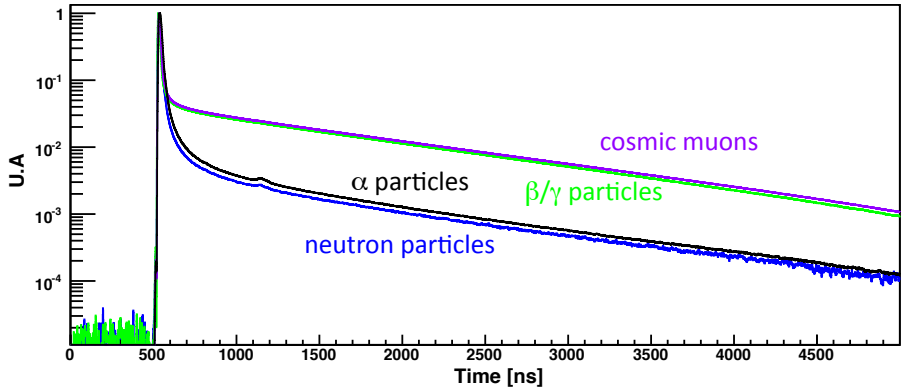

Figure 4.10: Average pulse shape for different particles. The afterpulse on the signals at 700 ns is due the ions from the first dynode drifting towards the photo cathode and hit out new electrons, which are seen as the afterpulse. For the average pulse of neutron and α , the after pulse is more visible since their slow component is much lower that the one for β/γ and μ particles.

Particle	Range selection [p.e.]	F_p	CR
$\gamma\backslash\beta$	[100;800]	0.276±0.010	0.233±0.005
μ	[2000;4500]	0.264±0.008	0.221±0.004
n	[100;300]	0.754±0.007	0.736±0.006
α	[4500;7500]	0.774±0.007	0.747±0.005

Table 4.1: Values of CR and F_p for different types of interactions.

The exponential decay model, used to extract the CR, relies on the assumption that the time scale of the production and modification of excimer is shorter than the measured

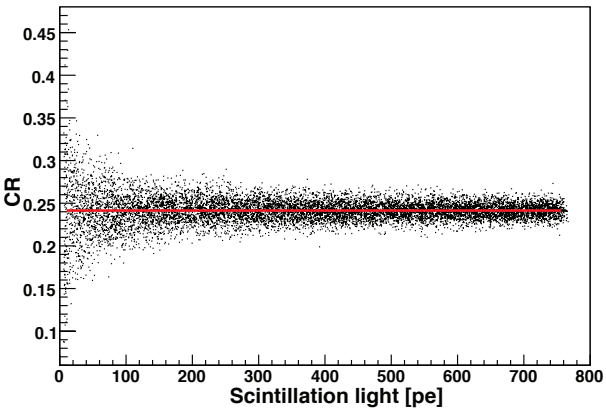

Figure 4.11: Reconstruction of simulated pulses with fixed component ratio. The red straight line at constant CR is an eyeball fit.

decay constants.

To the measure the component ratios at low energies using event-wise likelihood fits for recoiling Ar nuclei, α-particles and electrons, three different sets of data have been taken. One with the external ^{22}Na inducing electron recoils by 511 keV photons, the second induces nuclear recoil from the 2.45 MeV neutron from the NG and the last one induced with α recoils from the built-in ^{210}Po source. As mentioned previously the ^{210}Po source was coated with a thin layer of plastic in order to degrade and spread the energy of the emitted α-particles. For each type of interaction, the average pulse was fitted for several energy bins in order to extract the parameters t_0, σ, τ_1 and τ_2 and to fix them for the event by event likelihood fit. A and B are the only free parameters allowing a stable event by event likelihood fit. To exclude bias in the reconstruction of pulse shapes in respect to small signal heights, the software framework was tested with simulated pulses of fixed CR in the energy range of interest and analysed for flatness of CR. The component ratio after the reconstruction is shown in Fig. 4.11 as a function of the amplitude of the scintillation of the signal. Polynomials with orders between 1 and 10 were fitted to the scatter plot Fig. 4.11 and a Student test was then applied to the obtained parameters indicating clearly that no bias has been added to the CR by the reconstruction software with a confidence level higher than 99%.

The study of the pulse shape is crucial for a background discrimination in LAr dark matter detectors. The results of the pulse shape analysis to light yield studies in region at low and high ionization are in shown in Fig. 4.12.

The plot in Fig. 4.12(a) shows the values of CR estimated from the event by event likelihood fit vs. the total amount of scintillation light produced by these particles. For energies below $\sim$10 keV$_{ee}$, the two bands from electrons (green triangles) and nuclear recoils (blue triangles) start merging. The 1-σ width of the distributions obtained from Gaussian fits of vertical slices is illustrated by grey zones behind the data. The systematic uncertainties induced by the analysis method are the main errors on the determination

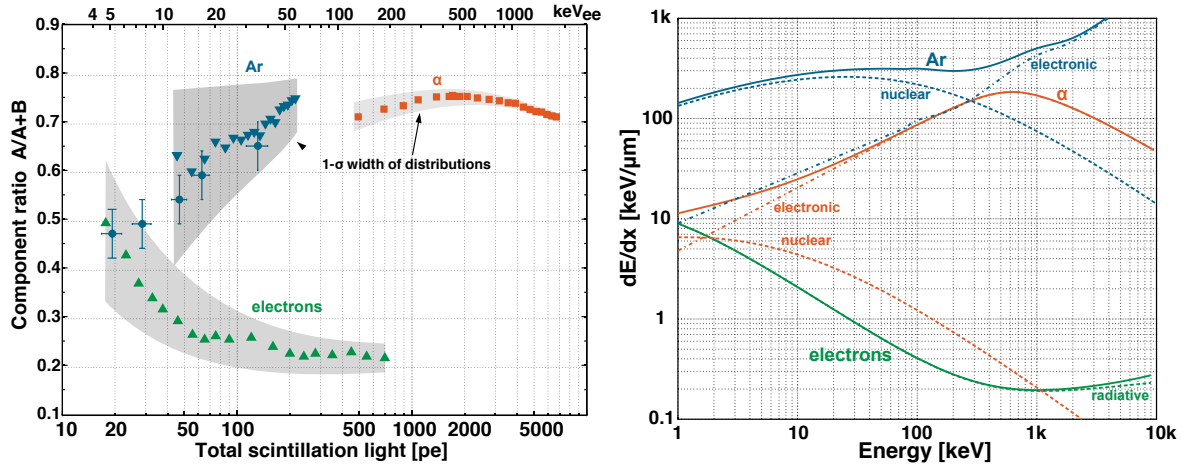

(a) (b)

Figure 4.12: Left: CR vs. light yield for Ar, α and e^- recoils. The grey zones indicate the 1-σ spread. Right: total stopping power (solid) and contributions (dashed) from SRIM, ASTAR and ESTAR [121].

of CR and are estimated to be roughly 0.25 of the distribution widths. The blue circles correspond to the data taken with the neutron scattering experiment (Data Season01 see Chapter 5) and results are derived from fits to mean traces. For the same particles the total stopping power and the nuclear and electronic contributions to it, are shown in the right plot. This data was obtained from SRIM, ASTAR and ESTAR's websites [121], respectively.

The correlation between both plots is easily observed, larger ionization densities generally lead to larger fraction of singlet states in the scintillation light. This trend is also true for the region towards smaller kinetic energies as well as for the maxima in the curves for α-particles. It is also remarkable the apparent value of the CR close to 0.25 for lowest ionization densities, corresponding to an uncorrelated production of triplet and singlet states. According to their statistical weights, a factor of 1:3 is expected for the relative ratio among their populations. If (luminescence) quenching effects are neglected, deviations from the minimal value of 0.25 imply either the enhanced production of singlet states on the exciton level or the transfer from triplet to singlet states shortly after their production in the area of high ionization density. Quenching effects among excimer states are excluded for the above mentioned arguments of lifetime invariance. The physical relation between the specific production of excimer states and the prevailing specific energy deposit can be unfolded from these data only if the integrated nature of the measurement is taken into account. In the next section, we apply this method to α-particles by using a simpler linear function for the relation between component ratio and linear energy transfer (LET).

4.3 Scintillation yield of alpha particles in LAr

In this section, we extract the value for the relative scintillation efficiency $\mathcal{L}_{\text{eff}}^{\alpha}$ of α-particles by comparing the shapes of the CR with the LET [122]. According to a good approximation, the latter is assumed to be identical to the electronic stopping power $\mathrm{d}E/\mathrm{d}x(E)$. For the fit function we use a 10^{th} degree polynomial parametrisation of the ASTAR curve from Fig. 4.12. The integrated nature is taken into account in a linear relation to the $\mathrm{d}E/\mathrm{d}x$ curve by the following formula:

$$CR(E) = \int_0^{x_{E=0}} \frac{\mathrm{d}CR(E)}{\mathrm{d}E} \cdot \mathrm{d}E/\mathrm{d}x\,(E)\,\mathrm{d}x \tag{4.10}$$

with

$$\frac{\mathrm{d}CR(E)}{\mathrm{d}E} = p_1 \cdot \mathrm{d}E/\mathrm{d}x\,(p_2 \cdot E) + p_3 \tag{4.11}$$

where E is energy, x the path length of the α-particle and p_i, i = 1..3 are the three free fit parameters defining the convolution of LET and CR. While p_3 describes an empiric vertical offset, p_2 is the parameter of interest introducing a scale for the energy dependent yield (quenching). The calculation approach is defined in [89]. The simple comparison between the maxima of both curves already gives a first estimate of the value for $\mathcal{L}_{\text{eff}}^{\alpha}$, being roughly 0.75. The measurements for CR obtained by event-wise likelihood fits of the signal shape from α-particles are shown in Fig. 4.13. The 1-σ spread is illustrated again by the grey band. In general, the fit (solid line) describes well the data except at low energies. The observed deviation might be due to our simple linear model. The curve of the electronic stopping power for α-particles in LAr from ASTAR (dotted line) is shown as well, deviating less than 2% from the total stopping over this energy range.

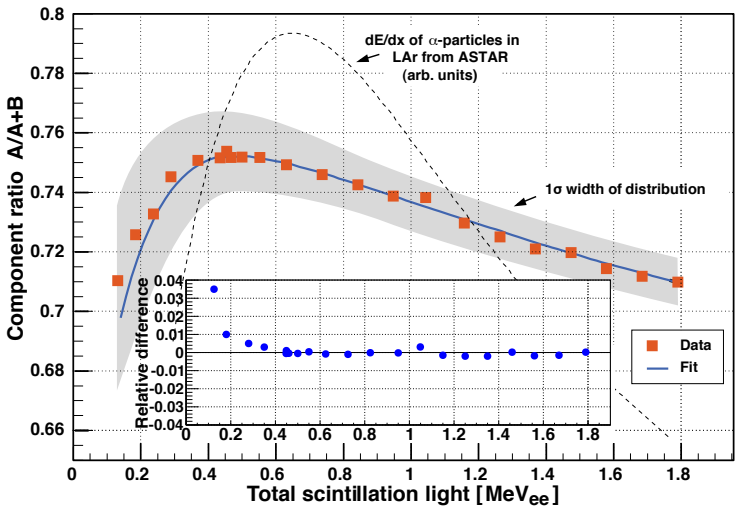

Figure 4.13: Component ratio of α-particles in LAr and fit vs. total scintillation light in units of MeV$_{ee}$. The inset shows the relative difference between the data and the fit.

The parameter p_2 was found to be at 0.74 ± 0.04 from the best fit. The result obtained corresponds to an estimate for the mean relative scintillation efficiency for α-particles in LAr in a range of 0.18-2.5 MeV$_{nr}$. Assuming a nuclear quenching of $f_n = 0.98$, the measured value of $q_n = 0.71$ obtained in [89] for 5.4 MeV α-particles matches within the errors with our result. A similar value was also obtained in [75]. In this energy range α-particles are scarcely affected by effects of nuclear quenching due to their relatively small mass. The light loss of roughly 25% is hence entirely due to luminescence quenching effects.

4.4 Light yield measurement with $\gamma-$sources

Energy calibration for electron recoils in LAr was estimated mainly by using the external ^{241}Am source producing the 59.5 keV photo-absorption peak. The light yield of the detector is defined as the ratio of the collected light to the deposited energy in the detector. The source was placed about at 10 cm to reduce the probability of pile-up events. Fig. 4.14 shows the Gaussian fit to the IPH distribution, performed for the light yield estimation. The fitted resolution, of about 16%, corresponds to $2.11 \times \sqrt{N_{p.e.}}$. The light yield was corrected for the finite integration time and by losses due to impurities in the liquid argon (see next section). Light yield calibrations were performed periodically during the data taking period. The average light yield has been obtained at 3.75 ± 0.8 p.e./keV$_{ee}$ and 3.39 ± 0.7 p.e./keV$_{ee}$ at zero electric-field for Season01 and Season02, respectively. The two light yields were different because the TPB layers were not exactly identical on the surface of the PMTs. Light yield as a function of time during the whole Season01 is shown

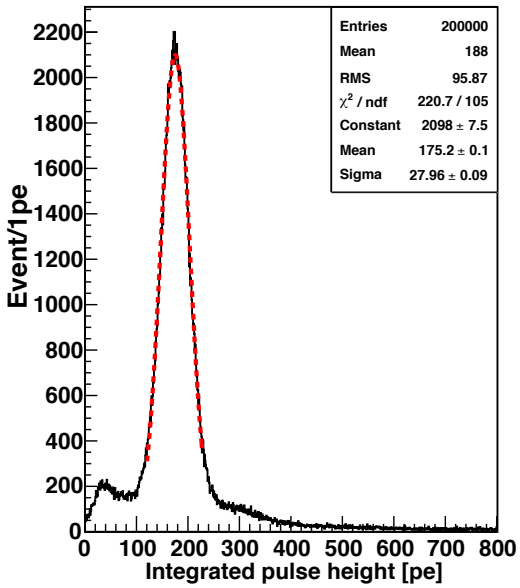

Figure 4.14: 59.5 keV line from the raw signals of the ^{241}Am data.

in Fig. 4.15. The uncertainty on the light yield is obtained from different contributions between the statistical and systematic uncertainties from the fits, fluctuations of the light yield measurements during the time and purity corrections for each ^{241}Am data set.

Other external sources were employed to cover a wide energy in order to check the linearity of the system as proceeded in the Section 3.4.2 with the ^{57}Co (122 keV), ^{22}Na (511 and 1275 keV Compton spectrum), as well as ^{137}Cs (662 keV Compton spectrum). No deviation from the measured light yield of the 59.5 keV γ-rays has been observed over the full range of energy. Fig. 4.16 shows a linear fit to the raw measurements taken under similar conditions.

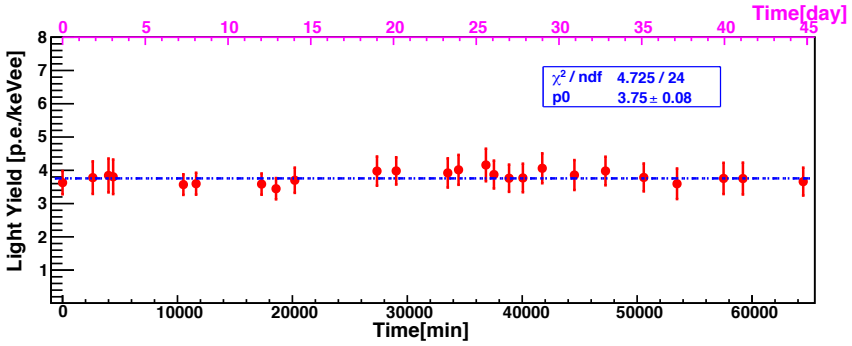

Figure 4.15: Light yield as a function of time from the Season01 run.

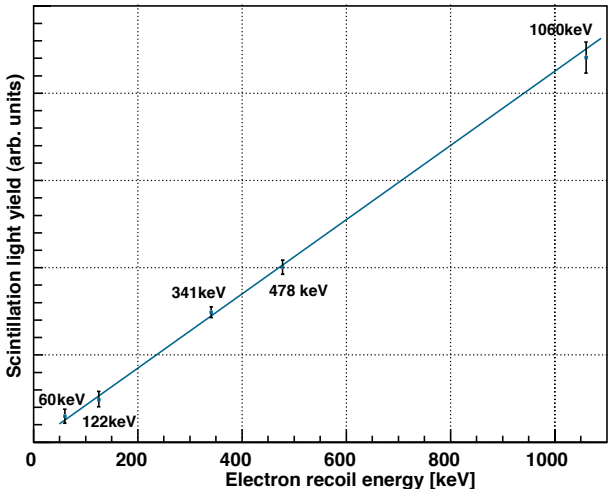

Figure 4.16: Scintillation light of various photon sources.

4.5 Analysis of the ^{83m}Kr source

Since dark matter detectors search WIMP signals at energy of tens of keV, a low energy calibration is required to quantify both the energy threshold and the WIMP sensitivity. The 59.5 keV line from the ^{241}Am source was employed to calibrate the detector. However, the disadvantage of using this external radioactive source is that the energy deposition is strongly localized in the active volume because the interaction length for the 59.5 keV γ-rays is $\sim$1.5 cm in LAr. For energies lower than 59.5 keV the energy deposition is even more localized, because the attenuation length of γ-rays gets smaller as their energy decreases.

The metastable ^{83m}Kr source, resulting from the decay ^{83}Rb with a half life of 86.2 days, is an alternative to illuminate the central part of the detector and to diffuse uniformly photons. This method has been first proposed in the KATRIN experiment dedicated to the measurement of the electron neutrino absolute mass [123]. ^{83m}Kr decays with a half life of 1.8 h via two electromagnetic transitions of 9.4 keV and 32.1 keV corresponding to the energy range of interest for dark matter detection (Fig. 4.17) [124]. The ^{83}Rb

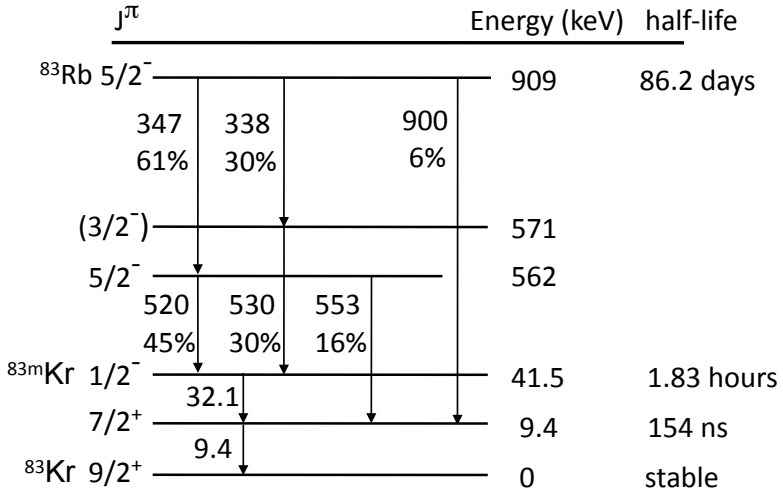

Figure 4.17: Energy level diagram in keV for the ^{83}Rb decay with the corresponding branching ratio and the half life [124].

source has an activity of about 177 kBq and has been introduced in the detector without affecting the purity level. The ^{83}Rb trap is directly connected to the gas system such as the radioactive gas fills the detector through the purity cartridge and the cryocooler by opening the valve V9 (see Fig. 3.27). During the ^{83m}Kr filling into the detector, the increased event rate was observed at about 50 Hz.

The emission of the 32.1 keV transition from the ^{83m}Kr decay, with a half life of 154 ns, is always followed by the 9.4 keV transition. Hence the double peak structure in the waveform from a typical ^{83m}Kr event: the first peak represents the prompt light from the 32.1 keV transition and the second one is the 9.4 keV transition as shown in Fig. 4.18.

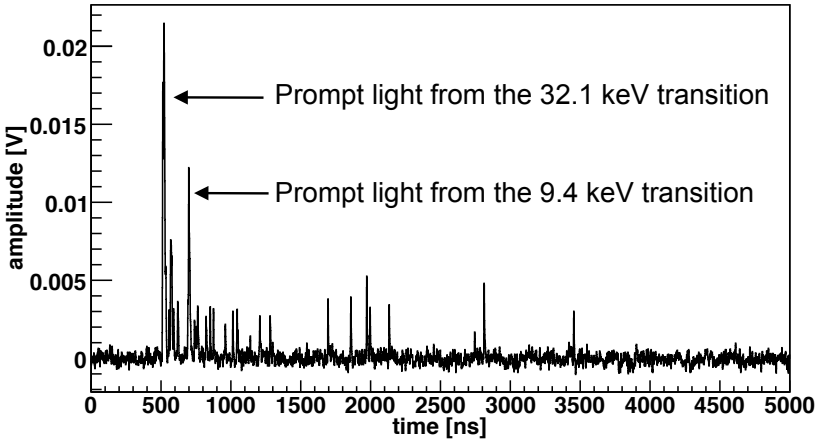

Figure 4.18: Example of a ^{83m}Kr signal in liquid argon from a single PMT.

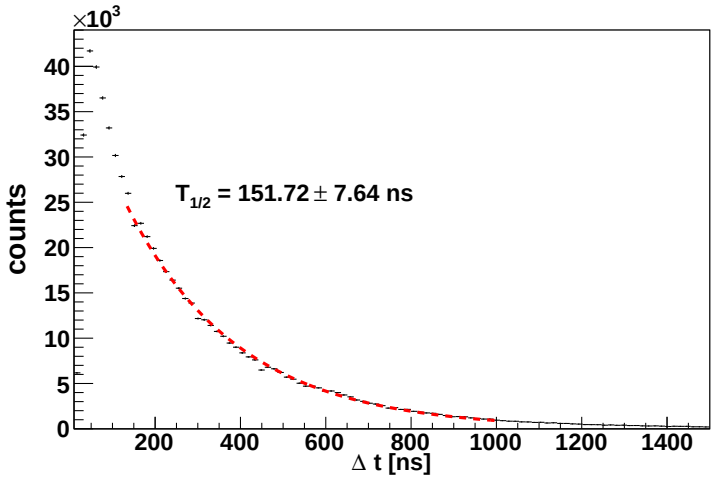

Figure 4.19: Measurement of the half-life of ^{83m}Kr $\frac{7}{2}+$ by computing the time difference between the first and the second highest peak.

The time difference between the first and the second highest peak Δt is reported by the Fig. 4.19 where the half-life of the exponential function is also shown. The half-life of ^{83m}Kr $\frac{7}{2}+$ was measured to be 151.72 ± 7.64 ns which is in agreement to the literature value [124]. In order to measure properly the light yield using the ^{83m}Kr source, the two pulses have to be treated separately because the light output response for the 9.4 keV and 32.1 keV scintillation light can be different. Therefore, the sum of the two transitions by integrating the whole waveform does not really correspond to a measured light yield for γ-rays at 41.5 keV. The measured light yield at 32.1 keV is estimated by calculation from the total scintillation light using the relation between $IPHA$ and CR shown in

Eq. 4.18. The corresponding value of the CR for electron recoils at this energy is chosen according to Fig. 4.12(a). The value obtained for $IPHA$ is 31.15 p.e. and the amount of the population of the singlet state is found at 25.5 p.e. by subtracting the contribution of the triplet state in the integration of the prompt light. Therefore with a CR ∼0.22 the total scintillation light is obtained at 118 p.e. which corresponds to a light yield of 3.68 ± 0.15 p.e./keV$_{ee}$.

A cross check has been done using the peak finding algorithm which looks for the position in time of the two highest peaks in the signal. The integration of the first signal (32.1 keV transition) is defined as the sum of all the clusters between the time at which the amplitude of the prompt light from the 32.1 keV transition is above $3\times\sigma_{ped}$ and the time at which the amplitude of the next peak is $3\times\sigma_{ped}$. Fig. 4.20(a) shows the integrated pulse of the first pulse (red histogram) with an integration width of 950 ± 50 ns and the second pulse (blue histogram) with a smaller integration width of 250 ± 50 ns since the amplitude of the signal of the 9.4 keV transition is lower and the fact there is also a part of the signal of the 32.1 keV transition. The corresponding 2D histogram displayed in Fig. 4.20(b), first pulse vs. second pulse, shows the correlation at $\rho = 0.4$ where a fit of an elliptical Gauss function is applied Eq. 4.12:

$$f(x,y) = A\exp\left[-\left(a(x-\mu_2)^2 + 2b(x-\mu_2)(y-\mu_1) + c(y-\mu_1)^2\right)\right] \tag{4.12}$$

with

$$a = \frac{\cos^2\theta}{2\sigma_x^2} + \frac{\sin^2\theta}{2\sigma_y^2} \quad , \tag{4.13}$$

$$b = -\frac{\sin(2\theta)}{4\sigma_x^2} + \frac{\sin(2\theta)}{4\sigma_y^2} \quad , \tag{4.14}$$

$$c = \frac{\sin^2\theta}{2\sigma_x^2} + \frac{\cos^2\theta}{2\sigma_y^2} \tag{4.15}$$

and where μ_1, μ_2 are the average pulse height of first and second peak respectively. The energy resolution of the peak of the 32.1 keV transition in terms of photoelectrons is $2.31\times\sqrt{N_{p.e.}}$ which is 9.5% higher than the one estimated from the 59.5 keV γ-rays.

In this method the measured light yield at 32.1 keV was obtained by comparing the integration pulse height of the 59.5 keV γ-rays with the ^{241}Am data, using the same integration width of the 32.1 keV transition and the same purity level as the one of the ^{83m}Kr data. The measured light yield with the 32.1 keV transition was found to be 3.95 ± 0.20 p.e./keV$_{ee}$. The determination of the light yield with the 9.4 keV is not trivial because the integration of the second pulse contains a part of the slow component from the 32.1 keV transition. The problem could be solved by defining a function to fit event by event the double peak structure of the waveform, but this method was not implemented within the framework of this work for the ^{83m}Kr data analysis.

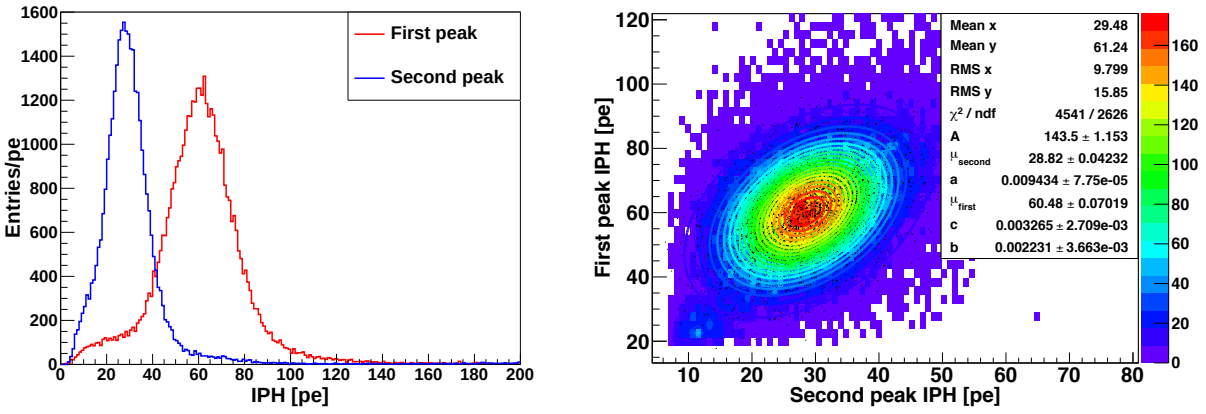

(a) (b)

Figure 4.20: Left: the integrated pulse height of the first peak (red) and the second peak (blue) using the peak finding algorithm. Right: a 2D histogram of the integrated pulse height of the two peaks showing the correlation.

4.6 Impurity effects - Light yield correction

The correction of the losses of the scintillation light in LAr requires to put into relation the total light scintillation corrected, denoted by $L_{S,cor}$, and the lifetime of the triplet state τ_2. Average signals from the 59.5 keV γ-ray data under different purity conditions, are fitted by the sum of two exponential functions convoluted with a Gaussian function, as given by Eq. 4.9. The relative amplitude of the singlet and triplet states, denoted by A and B, respectively are extracted from the fit. The measurement in LAr, illustrated by the Fig. 4.21, shows a linear relation between the density of the triplet state and their lifetime. The linearity between the measured total scintillation light, defined by the sum $L_S = A + B$, and the decay time of the slow component has already been observed in GAr according to [125]. Since the impurity quenching is a slower process than the one of the lifetime of the singlet state, only the triplet state B is affected, resulting in a reduction of its population, as illustrated. Whereas, the amount of the singlet state A remains constant for an impurity level $\tau_2 \geq 400\,\text{ns}$. In the first approximation, and taking into account the normalization factor for the exponential PDF, the corrected total scintillation light is estimated from the relation Eq. 4.16

$$L_{S,cor} = A + B_{cor} = A + \frac{B}{\tau_2} \cdot \tau_2^{max} \quad . \tag{4.16}$$

In this equation B_{cor} is the extrapolated yield of the triplet component and τ_2^{max} and the unchanged lifetime of triplet states in LAr (at maximum purity). The value of the corrected component ratio is determined by the relation Eq. 4.17. Therefore, the corrected

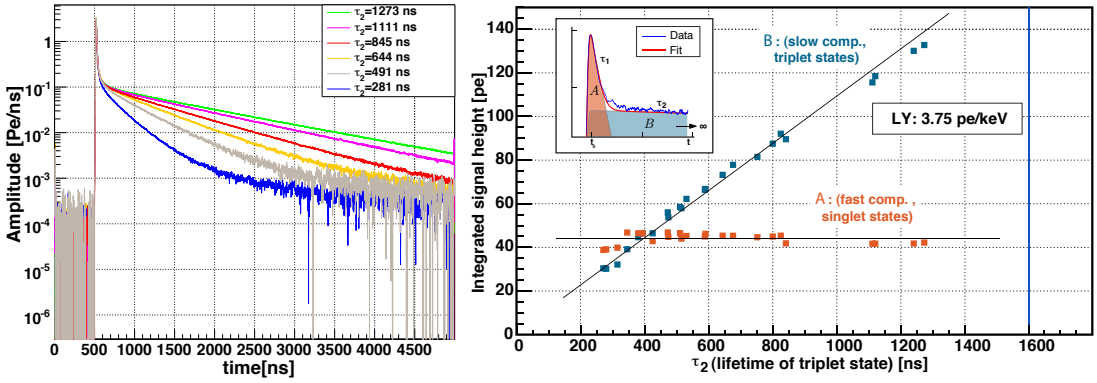

(a) (b)

Figure 4.21: (a) average traces from the 59.5 keV γ-rays under different purity conditions; (b) the graphic on the right corresponds to the decomposition of the scintillation light components for the same data.

light yields are calculated by the formula Eq. 4.18

$$CR_{cor} = \frac{A}{A + B_{cor}} = \frac{A}{(A + \frac{B}{\tau_2} \cdot \tau_2^{max})} \tag{4.17}$$

$$L_{S,cor} = \frac{A}{CR_{cor}} \tag{4.18}$$

According to these results, other quenching mechanisms, such as VUV absorption by impurities, are not affecting light yields under the present geometrical conditions and purity levels. The parameter CR is determined by fitting average traces but other methods can be used to calculate CR event by event. The next paragraph is dedicated to the development of this technique.

4.7 Purity correction event-wise

The impurity correction set out previously was performed by averaging out pulse shapes for one data set. Each data set contains a certain number of files, each of them containing 1000 events recorded. In the case of the data taking with ^{241}Am source (59.5 keVγ-line), the event rate recorded by the DAQ was estimated to be of 236.4 Hz, which means 4 minutes are necessary to produce a data set of 50 files from this source. Whereas for the neutron scattering data, the event rate was measured at 0.12 Hz and one day was necessary to complete 10 files. Since the value of the triplet state lifetime can decrease of about 10% after one day of data taking for the same data set, an event by event or file by file correction has to be adopted. The two following subsections describe the development of methods for impurity correction for a better reconstruction of the nuclear recoils events.

4.7.1 Event by event likelihood fit

A method using a likelihood fit on the waveform event by event was investigated. For convenience, the likelihood fit technique was first tested on the 59.5 keV γ-rays data because the tail of these signals is much larger and therefore easier to fit than the nuclear recoils signals. The fit consists of two steps. In the first step, the integration of the first

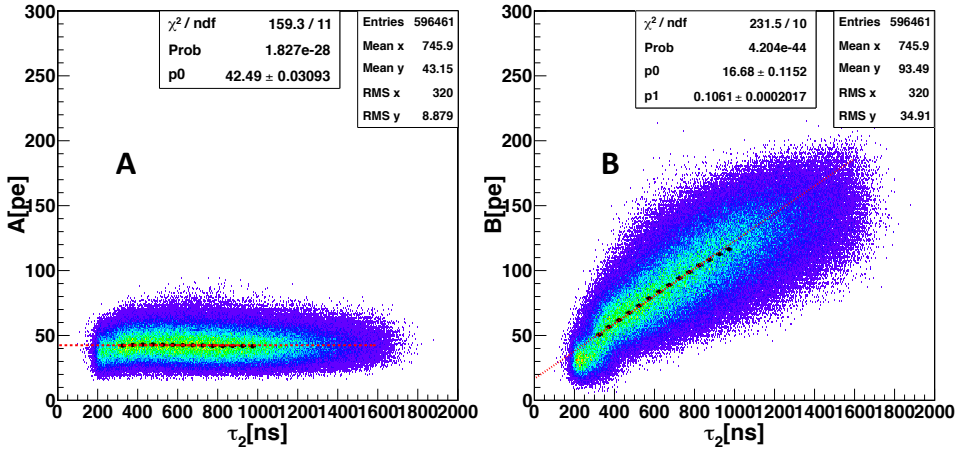

Figure 4.22: Results for the population densities of A (left) and B (right) under different purity conditions, obtained from the results of the event by event likelihood fit on the pulse shape for the 59.5 keV γ-rays data.

50 ns of the prompt signal is calculated to give a starting value of the parameter A. The parameters τ_2, τ_1 and σ are fixed and were previously determined from an average pulse of the 59.5 keV γ-rays, while the parameters A, B and t_0 are left floated. In the second step, a second likelihood fit is applied on the signal where the parameters A and t_0 are fixed, their values having been estimated during the first step. The parameters τ_2 and B are free to float, with a starting value $IPH - A$. The fit range on the signal was fixed at 2500 ns after the maximum height of the pulse and errors on samples from the waveform were set at $3 \times \sigma_{ped}$ of the noise distribution. The most significant source of systematic errors was found on the choice of the fitted window. The systematic uncertainty associated with the fit range was estimated to be 10-15% of the value of τ_2 by varying the fit within a time window from 700 to 3000 ns for a purity condition between 800 ns and 1300 ns. This systematic uncertainty increases with the increasing of the impurities due to a lower statistics of photoelectrons on the slow part of the scintillation light.

Results from the event by event likelihood fit on the waveform for the 59.5 keV data under different purity conditions are shown in Fig. 4.22. Black dots on the plots correspond to the mean value of the population density A and B, expressed in p.e., for each selected range of the value of τ_2. The mean values of A and B for each range of τ_2 were fitted with a linear function. The corrected light yield for impurities determined by this method is 3% higher than the one deduced from the fit on the average pulse. The increase of the

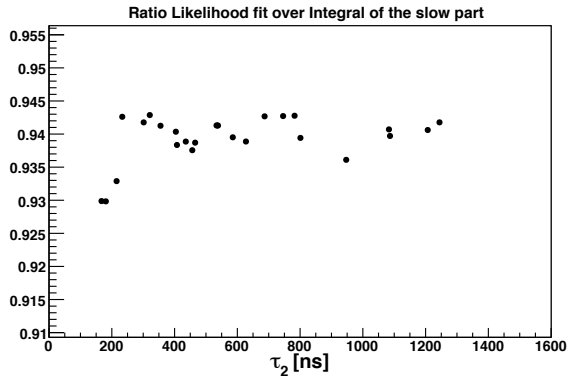

Figure 4.23: Ratio of the average B to the average $IPHB$ obtained from the event by event likelihood fit.

corrected light yield can be explained by the fact that τ_2 is systematically under estimated due to a low photoelectron statistics. Fig. 4.23 corresponds to the ratio of the mean of the population density B, obtained from the result of the event by event likelihood fit to the mean of $IPHB$ (the integration of the slow part of the signal) under different purity conditions. The results obtained from the likelihood fit are $\sim$6% lower than the ones obtained via the integration. The difference between the two methods is even larger for $\tau_2 < 350$ ns. Since nuclear recoils produce less scintillation light than electron recoils in the slow part of the signal, this method is not appropriate to reconstruct nuclear recoils events at very low energy and at low purity. To avoid this systematic effect, a new method has been developed using logarithmic binning on the pulse shape.

4.7.2 Logarithmic binning method

A different approach is used to compute the corrected integral pulse height from impurities in LAr in order to avoid systematic effects due to impurities and the low scintillation light in the slow part of the signal, especially at low energy for nuclear recoils. The pulse shape is divided into three regions as illustrated in Fig. 4.24. The first part called I_1, is the first 40 ns of the integration signal, starting $3\times\sigma_{ped}$ above the noise distribution (t_A) and corresponding to $4\times\tau_1$. The intermediate state C is taken into account between the fast and the slow part of the signal by integrating the signal over a reasonable time window between 40 ns and 150 ns, corresponding to three times the decay time of the intermediate state. This area is called I_2. The rest of the pulse shape is divided into several time binning, denoted by L_i for i = 1,..5, using a logarithmic function to calculate the width of time bins Eq. 4.19:

$$t_\mathrm{i} = \tau_2 \times \ln\left(\frac{N+1}{N+1-\mathrm{i}}\right) + t_0 \qquad . \tag{4.19}$$

The function depends on three parameters: N the total number of bins, t_0 the integration starting time and τ_2. The advantage of applying this technique is that one should

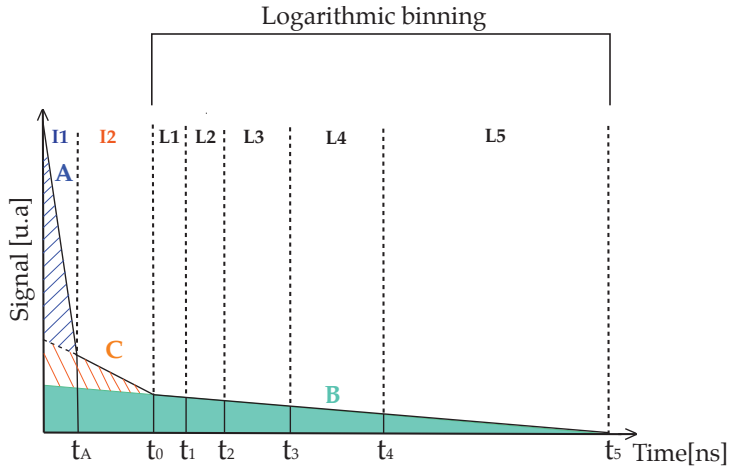

Figure 4.24: Scheme showing the principle of the logarithmic binning method with the contributions of the different population densities A, B and C.

expect the areas, defined by the logarithmic binning, are equals if the parameter τ_2 is well estimated. Therefore a calibration of τ_2 is possible file by file by fitting a linear function of the values of the bin content expressed in p.e. over the bin number. In the ideal case, the slope from the linear fit should be $m = 0$. In Fig. 4.25 a scan of τ_2 was performed file by file using variations of $+10$ %, $+5\%$, -5%, -10%, -20% and -30% of the value of τ_2 estimated from the average pulse shape. The best estimation of τ_2 is represented by the blue dashed line and is obtained from the intersection between the linear fit (red line) on the values of m for different τ_2 and the horizontal green dashed line showing $m = 0$. The results of τ_2 using this technique is in general $\sim$10-15% lower than the values extracted from the average pulse. Then the data are reprocessed with the correct value of τ_2 for each file event by event using the logarithmic binning method.

To extract the amount of the different population density, several steps are needed during the logarithmic binning method. The first step is to extract the population density B in the areas L_i starting from t_0,namely L.

This quantity is obtained by performing a weighted mean over the 5 bins and multiplying it by the total number of bins as illustrated by the general formula Eq. 4.20

$$L = (N+1) \times \frac{\sum_{\mathrm{i}=1}^{5} L_{\mathrm{i}} \cdot W_{\mathrm{i}}}{\sum_{\mathrm{i}=1}^{5} W_{\mathrm{i}}} \tag{4.20}$$

where $N = 5$ and W_{i} is the weighting factor given by the inverse square of the integration error denoted by σ_{i} for each bin i. The integration error is calculated according to the central theorem limit and multiplied by a factor 5. This factor is a proper characteristic of the PMTs and was determined by integrating the noise as a function of the number

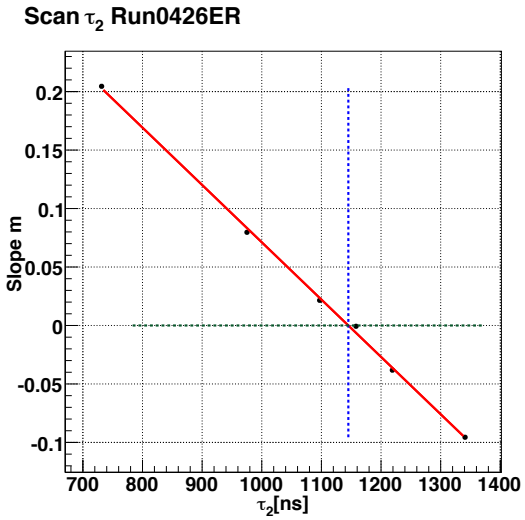

Figure 4.25: Scan of τ_2 for electron recoils (see text).

of integrated samples . Then the integration error is generalized for each bin i by the following formula Eq. 4.21

$$\sigma_{\mathrm{i}} = 5 \times \sigma_{ped} \times \sqrt{t_{\mathrm{i}} - t_{\mathrm{i-1}}} \qquad . \tag{4.21}$$

The integration over the intermediate state region, called I_2, doesn't contain only C but contains as well a part of B. The quantity of the triplet state to subtract in I_2 is defined by Eq. 4.22

$$C_B = \frac{\displaystyle\int_{t_A}^{t_0} \frac{B}{\tau_2} \mathrm{e}^{-\frac{t}{\tau_2}}}{\displaystyle\int_{t_0}^{+\infty} \frac{B}{\tau_2} \mathrm{e}^{-\frac{t}{\tau 2}}} \times L = \left(\frac{\mathrm{e}^{-\frac{t_A}{\tau_2}} - \mathrm{e}^{-\frac{t_0}{\tau_2}}}{\mathrm{e}^{-\frac{t_0}{\tau_2}}} \right) \times L \tag{4.22}$$

and then C_B is added to B. The same proceeding is applied to extract A in I_1, subtracting the part from C and B in this integral denoted by A_C and A_B respectively. Then the final densities population A, B and C are determined by the following equations:

$$\begin{aligned} A &= I_1 - A_C - A_B = I_1 - \frac{\displaystyle\int_0^{t_A} \frac{C}{\tau_3} \mathrm{e}^{-\frac{t}{\tau_3}}}{\displaystyle\int_{t_A}^{t_0} \frac{C}{\tau_3} \mathrm{e}^{-\frac{t}{\tau_3}}} \times (I_2 + C_B) - \frac{\displaystyle\int_0^{t_A} \frac{B}{\tau_2} \mathrm{e}^{-\frac{t}{\tau_2}}}{\displaystyle\int_{t_A}^{t_0} \frac{B}{\tau_2} \mathrm{e}^{-\frac{t}{\tau_2}}} \times (L + C_B) \\ &= I_1 - \left(\frac{1 - \mathrm{e}^{-\frac{t_A}{\tau_3}}}{\mathrm{e}^{-\frac{t_A}{\tau_3}} - \mathrm{e}^{-\frac{t_0}{\tau_3}}} \right) \times (I_2 - C_B) - \left(\frac{1 - \mathrm{e}^{-\frac{t_A}{\tau_2}}}{\mathrm{e}^{-\frac{t_A}{\tau_2}} - \mathrm{e}^{-\frac{t_0}{\tau_2}}} \right) \times (L + C_B) \qquad , \end{aligned} \tag{4.23}$$

$$C = I_2 - C_B + A_C \tag{4.24}$$

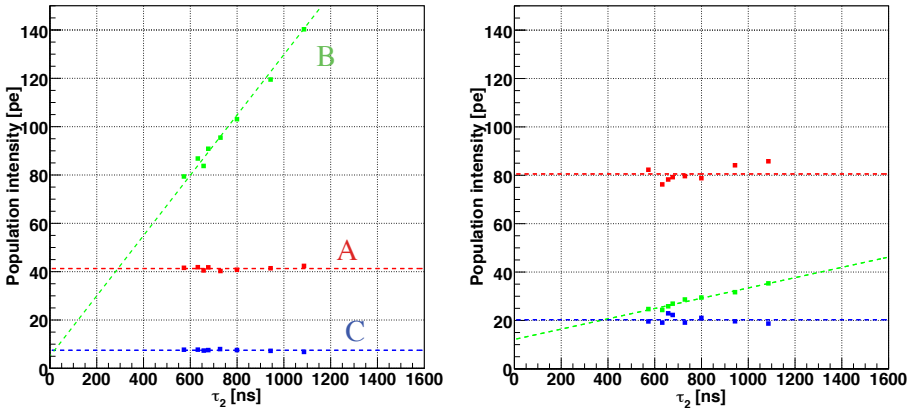

(a) (b)

Figure 4.26: Decomposition of the intensities of A, B, and C as a function of τ_2 using the logarithmic binning method for electron recoils (left) and for nuclear recoils (right).

and

$$B = L + C_B + A_B \quad . \tag{4.25}$$

A decomposition of the population intensities of these different states under different purity conditions has been performed using the logarithmic binning method as shown in Fig. 4.26. The graph on the left shows the mean value of A, B and C for the nuclear recoil while the same graph is represented for electron recoils on the right by selecting Bremsstrahlung X-rays events originated at the NG and not completely shielded. A clear population intensity dependence is observed on LAr purity is observed A and C and for both types of interactions while the intensity B is affected linearly by the impurity level. The corrected scintillation light from the triplet state is modeled by the expression

$$B_{cor} = A \cdot \frac{F_{B0}}{F_A} + \left(B - A \cdot \frac{F_{B0}}{F_A} \right) \cdot \frac{\tau^{max}}{\tau_2} \quad , \tag{4.26}$$

where $F_{B0} = 12.16$ p.e. and $F_A = 80.54$ p.e.. The offset observed on B in the graphs is scaled according to the value of A by introducing the factors F_{B0} and F_A which are determined by fitting a linear function over the values of B and A from the nuclear recoils events. For nuclear recoils, the contribution of C in the total scintillation light extrapolated to the maximum purity is 13% and for electron recoils 3%. A new parameter for n/γ discrimination, called Log Binning Separator (LBS), similar to the CR can be used and is defined as the ratio $A/(A+B_{cor}+C)$, where the different population densities are obtained using the logarithmic binning reconstruction method.

In Fig. 4.27, the black histogram shows the raw deposited energy distribution from the ^{241}Am radioactive source under different purity levels. The mix of data between different purity levels leads to a spread of the deposited energy distribution. When applying the log binning method to correct the spectrum, represented by the red histogram, the width

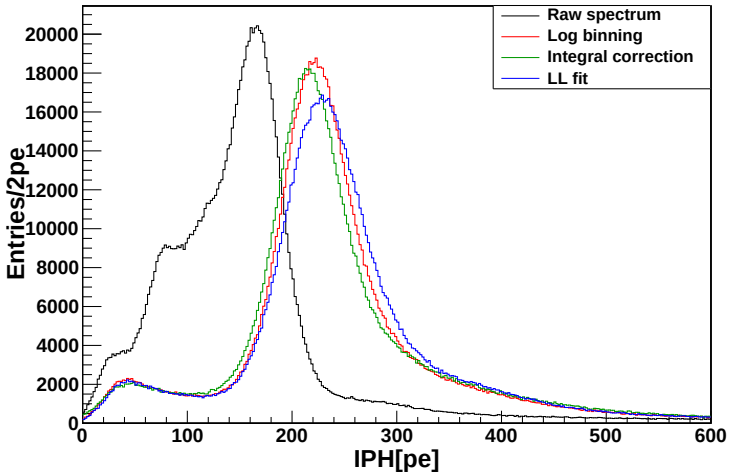

Figure 4.27: Data reconstruction comparison between the likelihood fit (blue), the logarithmic binning method (red) and the correction of the integration of the slow part (green).

of the distribution decreases dramatically and the spectrum is shifted for higher values of collected photoelectrons. A comparison has been performed between the spectrum obtained from the event by event likelihood fit, using a double exponential convoluted with Gauss distribution (blue histogram in Fig. 4.27) and the "normal" integrated pulse height obtained extrapolating the integration of the slow part of the signal (green histogram in Fig. 4.27). The underestimation of the triplet state lifetime determined by the likelihood fit leads to a strong correction of the density B, increasing the most probable value of the distribution by 3% (corresponding to a light yield of 3.87 p.e./keV$_{ee}$) compared to the one reconstructed from the logarithmic binning method. Whereas the most probable values inferred by the integrated pulse height, extrapolated to the maximum purity is 2% lower because the integral of the fast signal contains a part of the slow component which is not taken into account in the correction. The width of the spectrum obtained from the log binning method and from the corrected integrated pulse height are 15% smaller than the one inferred from the event by event likelihood fit. The light yield of the spectrum via the logarithmic binning method is obtained at 3.75 p.e./keV$_{ee}$, which is consistent with the one calculated from the fit on the meantrace.

4.8 Trigger efficiency

The low energy roll-off of the trigger efficiency can constitute a source of systematic uncertainty on the determination of $\mathcal{L}_{\text{eff}}$ and its understanding is essential especially for measurements at low energy. The trigger efficiency has been studied by using the ^{22}Na source, since at low energy the feature of the expected shape of the Compton spectrum is linear when assuming that the trigger efficiency is 100%, as illustrated by the red dashed rectangle that surrounds the linear part of the spectrum in Fig. 4.28(a). This latter curve

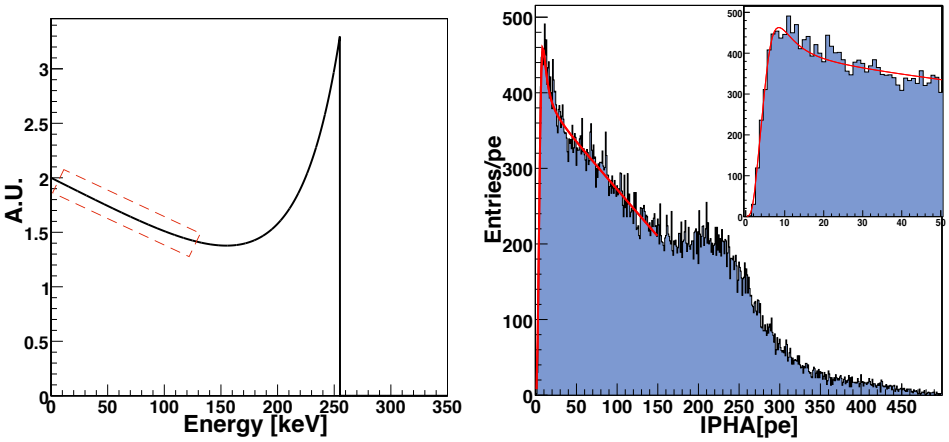

(a) (b)

Figure 4.28: (a) Compton spectrum from the 511 keV ^{22}Na source computed with the Klein-Nishina formula. The red box shows the linear part of the spectrum; (b) the integrated pulse height of the fast component ($IPHA$) is fitted using the function Eq. 4.27 (red curve).

was computed with the Klein-Nishina formula. In Fig. 4.28(b), the low energy part of the Compton spectrum was fitted using the following formula Eq. 4.27, where the S-function $(1 - \mathrm{e}^{-\frac{x}{B}})^C$ describes the response function of the trigger efficiency, $(D + E \cdot x)$ is the linear shape of the Compton spectra and a Landau function $L(A, \mu, \sigma)$ is used to describe the Čerenkov light from the γ-rays interaction occurring on the glass of the PMTs. Most of the Čerenkov events are located at $F_p \sim 1$. Fig. 4.29 shows the spectrum of the selected Čerenkov events for $F_p \geq 0.9$. A Landau function could describe this spectrum as illustrated by the blue curve since the expected Čerenkov light spectrum should be a Gauss function with a threshold effect due to the mean free path of electrons on the windows of the PMTs. The Čerenkov events cannot be removed completely, therefore the Landau function is implemented in Eq. 4.27 to determine the trigger efficiency.

$$\mathcal{F}(x) = (1 - e^{-\frac{x}{B}})^C \cdot \Big((D + E \cdot x) + L(A, \mu, \sigma) \Big) \quad . \tag{4.27}$$

The fit was performed in two steps: in the first step, the fit was only applied on the linear part of the spectrum, in the second step, the parameters of the linear function and the most probable value of the Landau function were fixed. Once the fit was applied with all the desired fixed parameters, the parameter C included into the power of the S-function which describes its asymmetry, may easily be determined. The measured trigger efficiency is then deduced from the values of the parameters of the S-function and is displayed in Fig. 4.30 through the green curve. According to the results, the efficiency at 8 p.e. is $\sim$100%, $\sim$96% at 4 p.e., $\sim$50% at 2 p.e. and $\sim$5% at 1 p.e. (December 2011). The roll-off of the trigger efficiency for the trigger settings using the programmable trigger logic in the oscilloscope during June 2011 is more significant due to a bad quality of the triggering

signal. In comparison to the results from the trigger settings during the data tacking in December 2011, the efficiency obtained during the data taken in June 2011 is ∼95% at 8 p.e., ∼55% at 4 p.e. and ∼6% at 2 p.e. for the logic trigger condition "OR" between the two signals of the PMTs. The roll-off is worse for the logic condition "AND", where the efficiency is ∼90% at 15 p.e., ∼42% at 8 p.e. and ∼4% at 4 p.e..

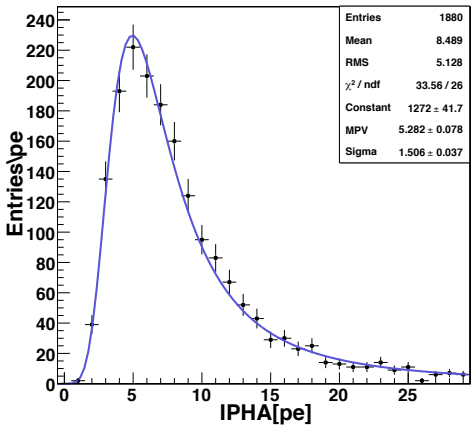

Figure 4.29: Spectrum of the selected Čerenkov events for $F_p \geq 0.9$ and fitted with a Landau function (blue curve).

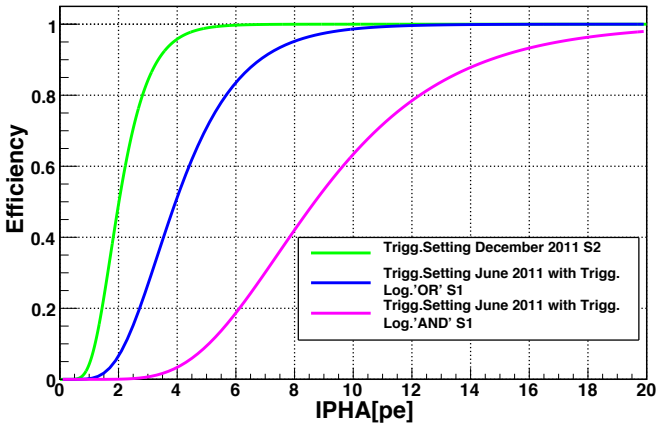

Figure 4.30: Trigger efficiency as a function of $IPHA$ obtained from the ^{22}Na source measurement for different trigger settings.

4.9 Time of flight calibration

The ^{22}Na external source is used to determine the TOF calibration. The radioactive

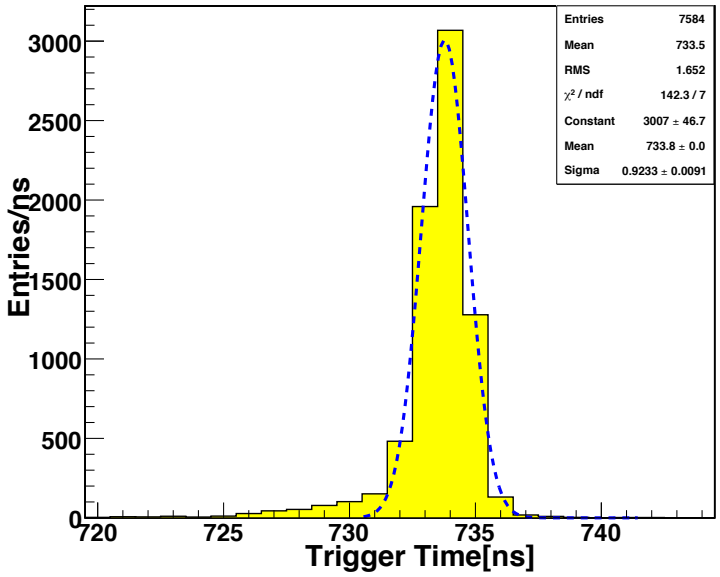

Figure 4.31: Time distribution of LAr events triggered by the 511 keV γ-rays from the ^{22}Na source, detected in the EJ-301 LSC.

source was placed equidistantly between the LAr cell and the LSC and on the same axis on the center of both detectors to ensure that the back-to-back pair of 511 keV γ-rays from the β^+ annihilation interacts at the same time in both detectors to determine the TOF = 0 ns.

A distribution of the trigger time from the coincidence photons is shown in Fig. 4.31. A cut on $IPHA$ above 100 p.e. is applied to determine precisely the reference time, because at lower energies the TOF was shifted. This effect, called time walk, is correlated to the trigger efficiency and leads to a time delay in the trigger of the LAr detector, which depends on the size of the signal in LAr. Fig. 4.32 shows the uncorrected TOF distribution due to the time walk as a function of the amplitude of the fast signal in LAr detector. The black dots represent the mean of each bin content of $IPHA$ with 1 p.e. of width and are fitted with the function Eq. 4.28 for signal smaller than 100 p.e. where the dots start deviating from the position of TOF = 0 ns. The blue dashed line is the result of the fit and the values of parameters are given in Tab. 4.2. The width of the same spectrum for energies lower than 100 p.e. decreases of 12% after the TOF correction using the Eq. 4.28 with the values listed in Tab. 4.2.

$$f(x) = k_1 + \frac{k_2}{1 + e^{-\frac{x}{k_3}}} + k_4 \cdot x \quad . \tag{4.28}$$

k_1	k_2	k_3	k_4
-1.72 ± 0.04	-13.32 ± 0.45	-3.77 ± 0.14	$1.59\cdot10^{-2} \pm 0.60 \cdot 10^{-2}$

Table 4.2: Values of the parameters obtained from the fit using Eq. 4.28.

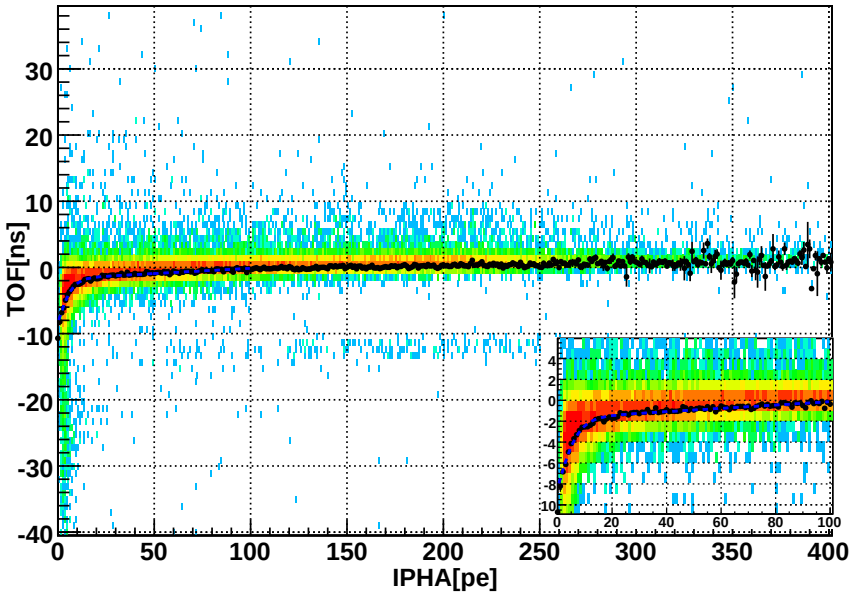

Figure 4.32: Shift on the TOF values as a function of $IPHA$ in LAr detector using ^{22}Na source for the TOF calibration.

Conclusions

The measured light yield of the LAr cell using the 59.5 keV γ-source are at 3.75 ± 0.08 p.e./keV$_{ee}$ for Season01 and 3.39 ± 0.7 p.e./keV$_{ee}$ for Season02. The study of the linearity of the energy using others external γ-sources and using the ^{83m}Kr shows no significant deviation from 32 keV$_{ee}$ up to 1060 keV$_{ee}$. A measurement of the $\mathcal{L}^{\alpha}_{\text{eff}}$ using an internal ^{210}Pb source is estimated to be 0.74 ± 0.04.

A correlation between $\mathrm{d}E/\mathrm{d}x$ and the relative intensity of the singlet and triplet states is observed for electron, Ar and α recoils. For energies above 40 keV$_{ee}$ the value of CR for α and Ar recoils are close to $\sim$0.75 while for the same energy range the CR for electron recoils is constant around 0.25. For nuclear recoils the rise of CR is estimated around 50% to 75% for energies between 20 and 200 keV$_{ee}$. At 10 keV$_{ee}$, the values of CR for electron and nuclear recoils converged.

The effect of impurities on the scintillation light in LAr has been studied, showing a linear decrease of the intensity of triplet state, whereas the intensity of the singlet state remains constant under a purity level $\tau_2 > 400$ ns. Methods have been investigated in

order to correct the reduced scintillation light for the data reconstruction. The logarithmic binning method is the most reliable technique for the correction of the luminescence quenching caused by impurities and takes into account a third component situated between 50 and 150 ns after the trigger signal. The contribution of the third component to the total scintillation light is 13% and 3% for nuclear and electron recoils respectively.

Chapter 5

Neutron scattering measurement in LAr

5.1 Data processing and data taking

In the context of the neutron scattering experiment, the data are processed by a dedicated software, as described in the previous chapter. The two waveforms from both PMTs are first corrected from the baseline, time shift and then combined. The data are also corrected for the impurities effect which affect the light yield as described in Section 4.6 and are also corrected for the trigger efficiency roll-off.

The LAr cell is placed at about 73 cm from the neutron emission point. A 1 m long arm rotating around the center of the LAr cell is used to set the 5" LSC at various scattering angles from the LAr cell. During the data taking, the distance between the LSC and the

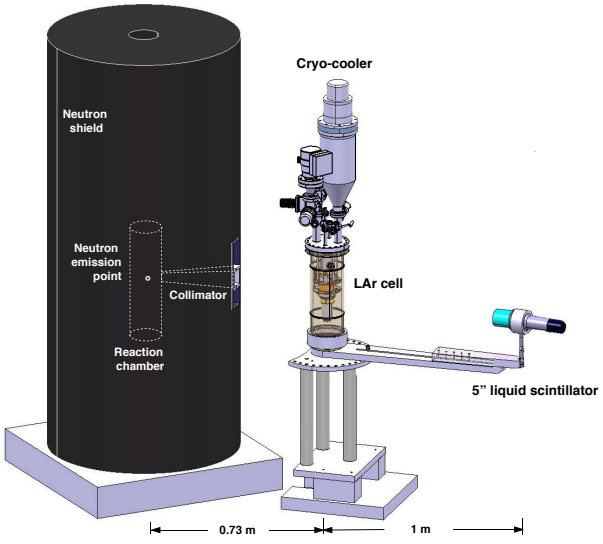

Figure 5.1: Experimental setup for the $\mathcal{L}_{\text{eff}}$ measurement in LAr.

LAr cell was set to 1 m for a suitable TOF measurement. The TOF is calculated from the time difference of the TAC output in the module MPD4 and the signal in LAr cell. The TOF is calibrated and corrected with the back-to-back coincidence of 511 keV γ-rays from the ^{22}Na source. A polyethylene collimator with square cross section restricts the emission of the neutron of about 0.2% of 4π, fully irradiating the fiducial volume of the LAr cell. To avoid neutrons passing directly in the LSC without interacting in the LAr cell, a square polyethylene plate 10 cm thick mounted on the tripod was placed close to the LAr cell.

Neutron scattering data were measured at 7 different angles: 20°, 25°, 30°, 40°, 50°, 60° and 90° corresponding respectively to 7.4 ± 2.7, 11.5 ± 2.8, 16.4 ± 3.9, 28.5 ± 5.2, 43.4 ± 6.0, 60.5 ± 7.1 and 119.5 ± 7.7 keV$_{nr}$. Errors on angles or mechanical misalignment were estimated to be below 0.5°. The angular acceptance of the LSC dominated the uncertainties in nuclear recoil energies and was determined from the results of the GEANT4 MC simulation described in Section 5.3. Data were separated into two periods in which data were taken with different trigger settings (see Section 4.1):

- **Season01** corresponding to the data taking during the summer 2011,
- **Season02** representing the data taking during winter 2011/12 with an improved trigger setting.

In most cases the neutron generator was operated at 80 kV and 10 mA corresponding to the emission of about 6.10^5 neutrons/s in 4π. The operation condition of the neutron generator was chosen in such a way that the accidental background induced by bremsstralhung (generated by the NG) was kept at an acceptable level (∼3-4/min). The total background rate was estimated at 5/min, caused mainly by two sources, cosmic muons saturating the LSC output and faking a neutron signal in the analog pulse shape discriminator MPD4, and accidental coincidences between diffusely scattered neutrons and X-rays from Bremsstrahlung. Whereas 1 neutron/min scattered off an argon nucleus in the sensitive volume and was detected in the LSC. Moreover, it has been observed during these operation conditions that the apparatus was more stable when producing little discharge called “mini-arcs" on the electrodes of the neutron generator. These mini-arcs occur especially during the initial running condition of the reaction chamber caused by the change of the gas plasma impedance. In addition to these constraints, the operating conditions of the neutron generator were adjusted in such a way that the temperature of the reaction chamber wall was not to exceed 100 C. A summary of the operating conditions for each measured scattering angle and for different periods of data taking are listed in the Tab. 5.1.

5.2 Event selection and measured nuclear spectrum

Examples of TOF measurements are shown in Fig. 5.2 for the scattering angle 25° (left side) and 30° (right side). The upper plot for each scattering angle shows the prompt

θ	Period	HV(kV)	Current(mA)	Running times(s)
20^0	Season01	82	9	312.8k
25^0	Season01	80	10	269.2k
25^0	Season02	80	10	381.8k
30^0	Season01	80	10	284.8k
30^0	Season02	80	10	234.2k
40^0	Season01	82	9	379.9k
40^0	Season02	80	10	219.2k
50^0	Season01	82	9	291.5k
60^0	Season01	80	10	288.8k
90^0	Season01	82	7	196.5k

Table 5.1: Neutron generator settings used for the seven scattering angle measurements. The live time and the period of each data taking are also mentioned.

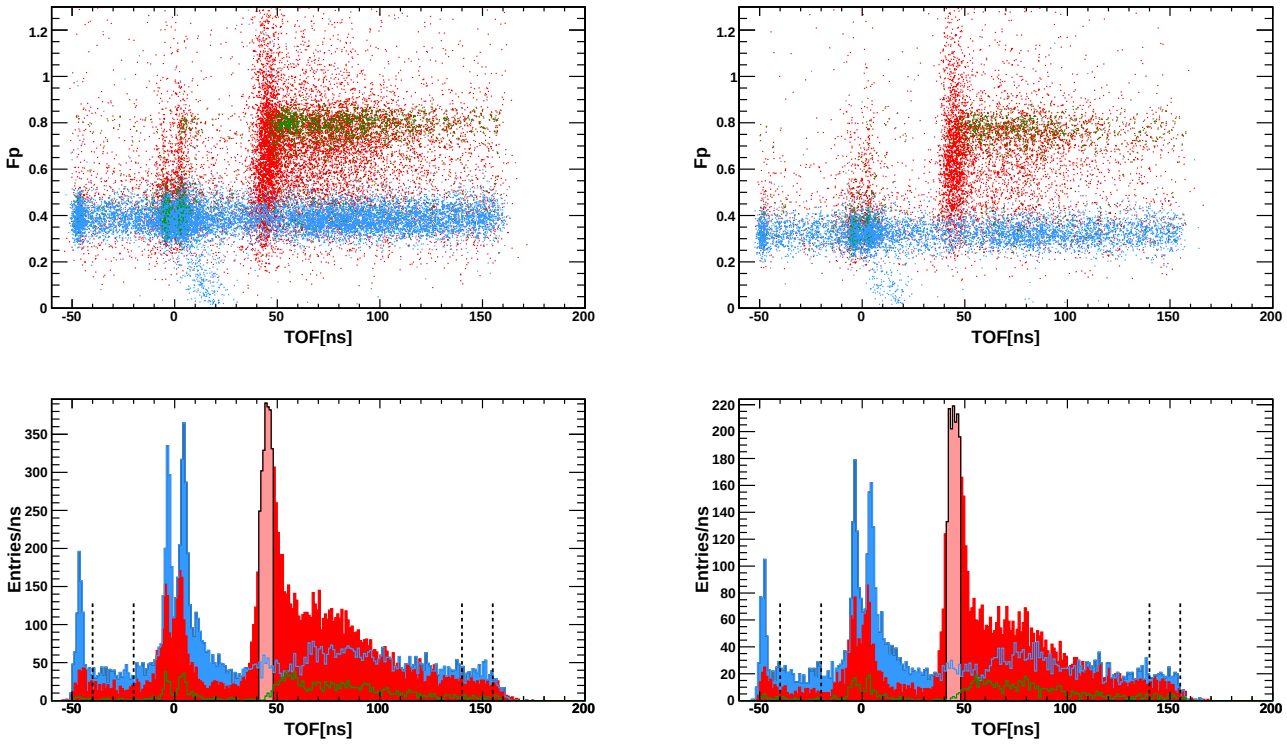

Figure 5.2: Prompt fraction vs TOF scatter plots between the LAr signals in the LAr cell and the LSC and the corresponding projection on the x-axis for the scattering angles 25° (left side) and 30° (right side). The events in red correspond to nuclear recoils selected by the two dimension cut, while the anti-cut is shown by the events in blue representing the electron-recoils. The events in green correspond to nuclear recoils at energies above 120 p.e..

light fraction F_p vs. the TOF and the histogram on the bottom is the projection over the X-axis corresponding to the TOF spectrum. The distributions of nuclear recoil signals are shown in red and are dominated by elastically scattered neutrons around the nominal time of flight, i.e. 46-48 ns. Nuclear recoils events are selected using a two dimensional cut which is explained in the next paragraph. A clear broad distribution is observed as well, caused by inelastic scatters. These events lose a substantial fraction of their energies. Neutron scattered with material outside the active volume are also responsible for the broadening of the spectrum. The TOF spectrum of the inelastic scattering events is in good agreement with the Monte Carlo expectation which the peak is ∼80 ns. The position in time of the elastic peak is consistent as well with the simulation. Neutrons may scatter off heavy materials after interacting in the active volume of the LAr cell loosing tens keV and traveling a longer distance before reaching the LSC. Hence the reason why neutrons from the elastic scatter are selected quite far away from the region after the elastic peak in the TOF spectrum. The blue histogram shows the events from the electron recoils band mainly due to accidental background between diffusely scattered neutrons and X-rays from Bremsstrahlung. The two clear peaks around TOF = 0 ns in the TOF spectrum are cosmic muon events arriving from both directions between the LAr cell and the LSC (the peak at -3.1 ns corresponding to the direction from the LSC to LAr and the one at 3.1 ns corresponding to the opposite direction) and are used to cross-check the reference TOF = 0 ns. Since the LAr detector trigger and the LSC trigger are not correlated, the accidental background is uniform and appears as a flat component in the TOF spectra. In the electronic recoil band a slight accumulation of events is observed after the elastic peak around 70-90 ns. These events correlated in time with inelastic scatters from the nuclear recoils band are inelastic scatters where neutrons scatters are also detected by the LSC. The peculiarity of these events is that they are induced by neutrons that interact inelastically in LAr outside the active LAr volume and the resulting photons produced from this interaction are detected in the active volume, hence their position in the electronic recoil band. The events shown in green are nuclear recoil events with an energy above 120 p.e. and include neutron multiple scatters and neutron inelastic scatters.

Two main cuts are applied to select neutron elastic scatters:

- A time cut of a typically 8 ns wide window −6 ns to the right of the most probable value of the elastic scatter peak and 2 ns to the left − represented by the pink area in the TOF spectra in Fig. 5.2, it serves as a main event selector. The values of the time cuts for each measured angle are shown in Tab. 5.2.

- A two dimensional cut using the following parameter IPH and LBS (defined in Section 4.7.2) removes very efficiently accidental coincidences with X-rays, γ's, inelastic scatters and cosmic muons as shown in Fig. 5.3.

The parameterization of the two dimensional cut is the same for each neutron scattering measurement: examples are displayed for low angle 25° in Fig. 5.3 and at higher angle 60° in Fig. 5.4, where the separation in 2D on the scatter plot illustrating LBS vs. IPH

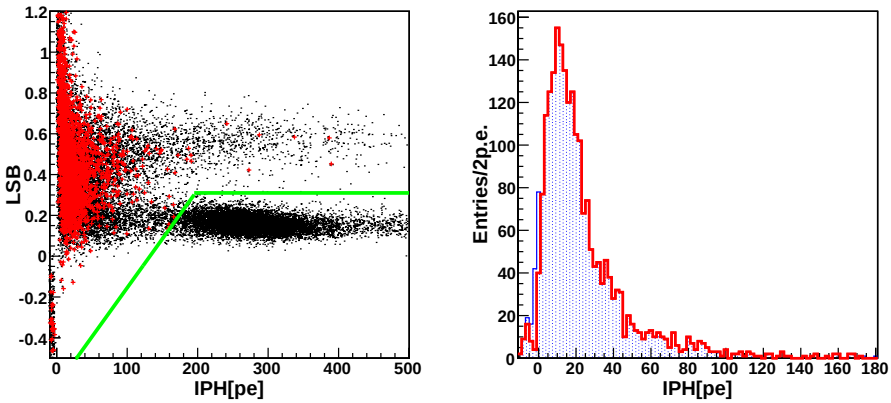

Figure 5.3: LBS vs. IPH on the left with the corresponding energy recoil spectrum on the right for the scattering angle 25°.

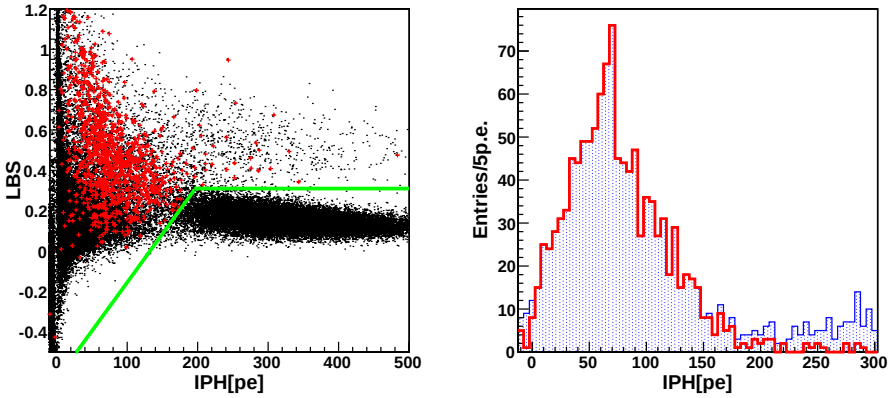

Figure 5.4: Same plots as Fig. 5.3 for the scattering angle 60°.

is represented by a green line. The red crosses on the scatter plot show the position of the events selected by the TOF cut and the two dimensional cut. The superimposed histograms on the right of the Fig. 5.3 and Fig. 5.4 show the events selected by the latest cut condition represented in red histogram while the blue histogram corresponds to the energy spectrum applied only to the TOF cut. As it can be noticed the 2D cut removes mainly the X-ray background without affecting the signal. The small signals situated on the negative part of the histograms are badly reconstructed.

The nuclear recoil energy spectra obtained from the integration of the fast signal $IPHA$ and the total integral IPH after the final selection are shown in Fig. 5.5 for the scattering angle 25° (top) and 30° (down). The residual neutron accidental background is also illustrated by the blue histogram for $IPHA$ and IPH. The time window taken for the expectation of this accidental background has been chosen far from the elastic peak and the broad part in the TOF spectra, as indicated in dashed black lines in Fig. 5.2 and their values are also listed in Tab. 5.2.

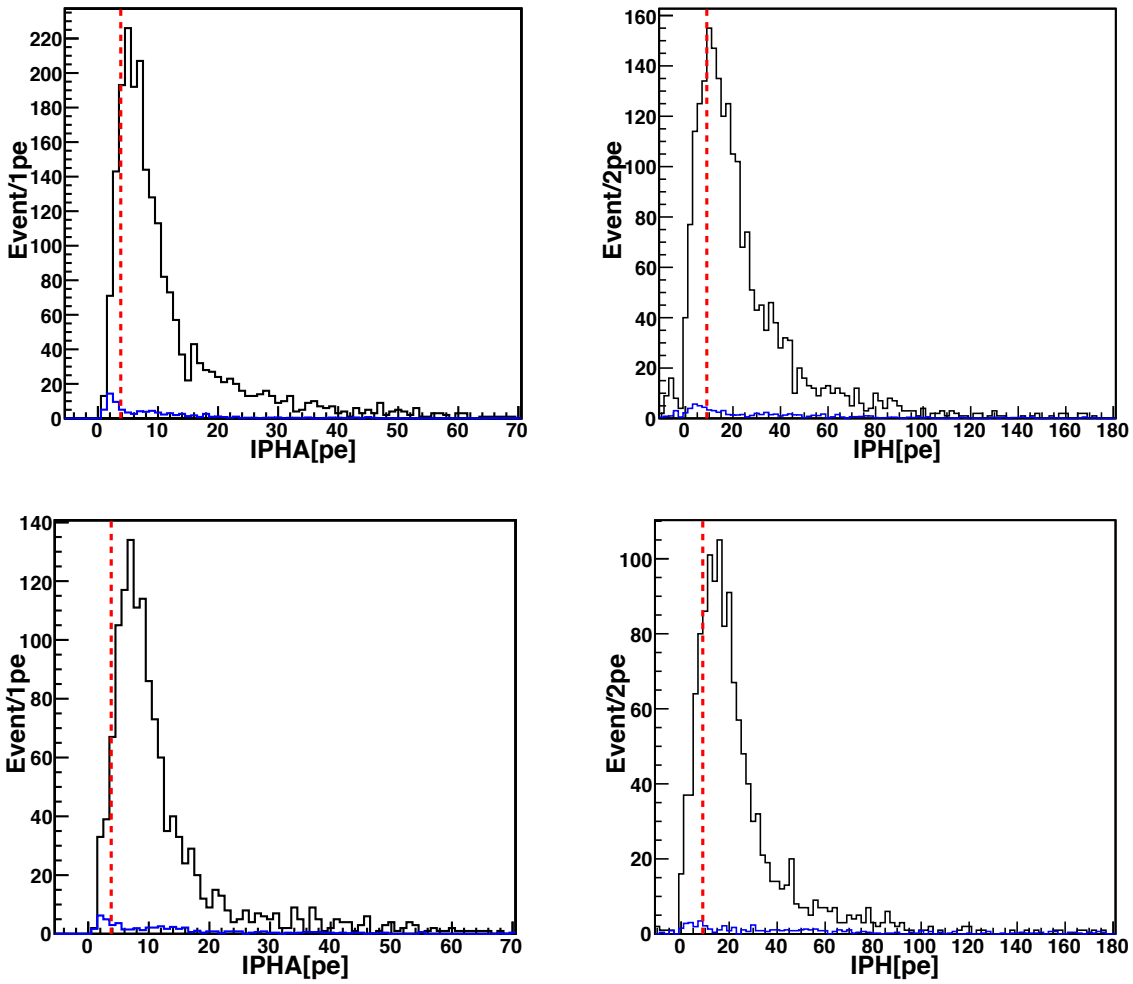

Figure 5.5: Energy recoil spectra of the selected events for $IPHA$ (left) and IPH (right). In black are the spectra obtained applying the final cuts for the angles 25° (top) and 30° (bottom); the superimposed accidental spectra are also reported in blue. The vertical red dashed line indicates the pulse height corresponding to 90% trigger efficiency.

θ	Elastic peak time window(ns)	Accidental background time window(ns)
20°	[41,48]	[-60,-20];[150,190]
25°	[41,48]	[-40,-20];[140,155]
30°	[41,48]	[-40,-20];[140,155]
40°	[41,48]	[-40,-20];[140,155]
50°	[41,48]	[-60,-20];[150,190]
60°	[42,49]	[-60,-20];[150,190]
90°	[42,52]	[-60,-20];[150,190]

Table 5.2: Time of flight windows to select neutrons that scatter elastically traveling between the LAr detector and the LSC and time of flight windows used to estimate the contamination of the accidental background of the LAr trigger and the LSC trigger in nuclear recoil spectra.

The residual background spectra selected before and after the neutron elastic peak in the TOF spectra, were compared with each other and were found to be compatible for a given scattering angle measurement. Therefore we can deduce that the accidental background is stationary in time for each neutron scattering angle measurement. The contamination of the nuclear recoil by the residual accidental background is estimated to be about 5% on average.

In addition to the peak in the nuclear recoil energy spectra due to the elastic scatter neutrons, there is a background due to neutrons that scatter in different materials outside the LAr detector, interacting before or after in the LAr active volume. This type of background, referred to as "material background", cannot be removed from the data spectrum and is included in the Monte Carlo spectrum.(see Section 5.3). The spread of the peak in the nuclear recoil spectrum is determined by the position and the finite size of the detectors. The intrinsic energy resolution of the LAr detector contributes as well to the spread of the measured nuclear recoil spectrum. The dashed red line indicates the position of 90% of the measured trigger efficiency affecting the distribution of the signal.

In [122] we estimated roughly the $\mathcal{L}_{\text{eff}}$ for nuclear recoils from the mean around the peak of the distribution of $IPHA$ and the value of the CR, determined by the average pulse of the selected events. In this preliminary study the light yields from nuclear recoils, were obtained using only $IPHA$, corrected for impurities using the Eq. 4.16 and were also corrected for the trigger efficiency roll-off, especially for low energies, as illustrated in Fig. 5.6 for the angles 20° (with a trigger setting from Season01) and for 25° (with a trigger setting from Season02). The dashed blue curve indicates the trigger efficiency as a function of $IPHA$, while the black and the dashed red histograms correspond to the raw nuclear spectrum and the nuclear recoil spectrum corrected for the trigger efficiency respectively. Results of $\mathcal{L}_{\text{eff}}$ for each measured angle using this method are listed in Tab. 5.3 with the values of CR and the values of the mean distribution of $IPHA$.

A cross-check of the $\mathcal{L}_{\text{eff}}$ measurement has been performed using the IPH corrected by the log binning method reconstruction (see Section 4.7.2). Results of $\mathcal{L}_{\text{eff}}$ obtained from

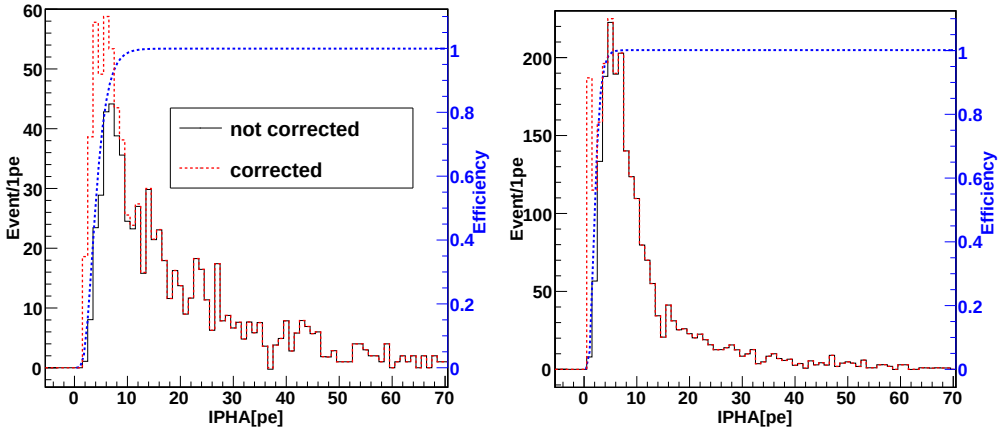

(a) (b)

Figure 5.6: $IPHA$ spectrum corrected for the trigger efficiency is shown in red for the angles 20° (a) and 25° (b). While the blue dashed curve shows the trigger efficiency as a function of $IPHA$ with the proper axis on the right of the histogram in blue.

θ	E_r (keV_{nr})	$\langle IPHA \rangle$ (p.e.)	CR corrected	$\mathcal{L}_{eff}$ (from $IPHA$)	$\mathcal{L}_{eff}$ (from IPH)
20°	7.4	4.8 ± 0.8	0.38 ± 0.06	0.456 ± 0.084	0.466 ± 0.089
25°	11.5	7.1 ± 1	0.42 ± 0.06	0.423 ± 0.070	0.427 ± 0.075
30°	16.4	8.5 ± 0.7	0.47 ± 0.05	0.318 ± 0.041	0.340 ± 0.046
40°	28.5	13.1 ± 1	0.49 ± 0.05	0.272 ± 0.030	0.269 ± 0.032
50°	43.4	26.0 ± 1	0.54 ± 0.05	0.290 ± 0.026	0.310 ± 0.029
60°	60.5	38.0 ± 2	0.59 ± 0.05	0.279 ± 0.024	0.275 ± 0.027
90°	119.5	87.0 ± 10	0.65 ± 0.05	0.295 ± 0.042	0.314 ± 0.048

Table 5.3: Table showing the $\mathcal{L}_{eff}$ results determined from the mean distribution of $IPHA$ and the CR corrected for impurities and obtained from the average pulse shape of the events selected. Also the $\mathcal{L}_{eff}$ results using IPH corrected by the log binning method reconstruction is shown.

the IPH spectra are consistent within the errors. For nuclear recoils at energies above 16.36 keV_{nr} or 6 keV_{ee}, the measurements are compatible with those obtained in [70], with a flat $\mathcal{L}_{eff}(\langle \mathcal{L}_{eff} \rangle = 0.291 \pm 0.033)$.

A more precise study was performed, consisting in comparing the measured distributions to the ones generated by GEANT4 MC simulation. The description of the simulation is detailed in the following section and the procedure used to determine $\mathcal{L}_{eff}$ from the measured and simulated recoil energy spectra is explained in Section 5.4.

5.3 Monte Carlo simulation

A comprehensive GEANT4 simulation was written for the neutron scattering in LAr to study the detector response. The main components of the setup were included in the simulation to get a realistic description of the experiment. In particular the simulation takes into account:

- **1.** the assembly of the neutron generator with its shielding and collimator,
- **2.** the vacuum cryostat and different components of the LAr detector (the vessel, the reflector foil, the PMTs, the support frame, etc.),
- **3.** the LSC.

A photograph of the LAr cell and a picture of the same detector used in the simulation are shown in Fig. 5.7.

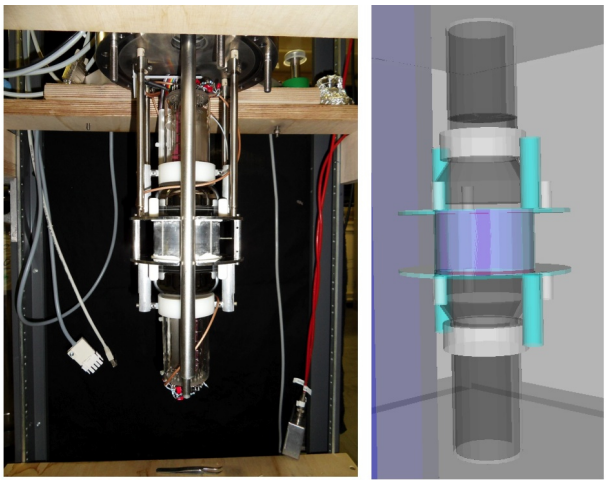

Figure 5.7: Left: picture of the LAr cell detector; right GEANT4 model.

Neutrons were emitted isotropically into 4π with a monochromatic energy of 2.45 MeV. 100 millions events were generated for each angle and an event was recorded when a particle interacted in the active volume. The simulation recorded the following information in the active volume of LAr:

- event number
- the number of incoming and outgoing particles with their names,
- the energy of the incoming and the outgoing particles and their directions,
- the number of interactions and the position of the interaction in the active volume,

- the type of primary particle (incident particle creating the interaction),
- the total energy deposited and the energy deposited in each interaction,
- the interaction time since the neutron was generated,
- the type of interaction: elastic, inelastic, annihilation, capture, Compton, etc,
- the type of process for the energy deposition: hadron ionization, electron ionization, photo absorption, etc,
- the number and type of secondary particles: ^{40}Ar,^{38}Ar,^{36}Ar, electron, γ, etc.

Most of the information can also be retrieved as well in the LSC volume: energy deposit, interaction time, number of interactions, 3D position, type of interaction.

Events can be classified in:

- elastic, inelastic scattering or both,
- single and multiple scatterings,
- scattering only in the active volume or scattering outside the active volume.

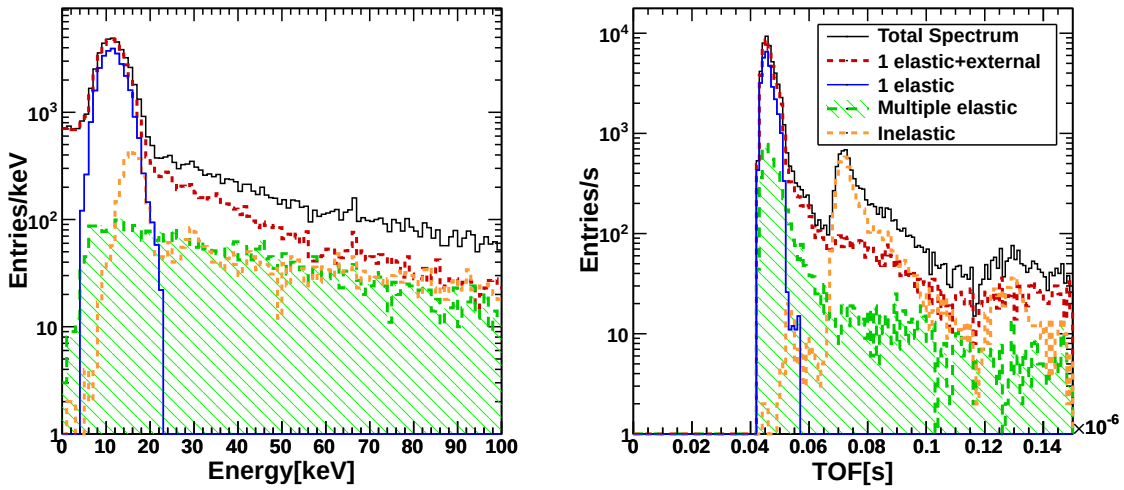

Figure 5.8: Example of the simulated recoil energy distribution at 25° (left) and the corresponding TOF spectrum (right).

Fig. 5.8 shows an example at 25° the contributions of the different classes of events in the simulated nuclear recoil energy spectrum (left) and in the TOF distribution (right). These spectra are obtained without implementing the resolution. For each measured scattering angle, the energy spectrum contains a clear peak for elastic scattering where the amplitude corresponds to the expected deposited energy and an exponential distribution related to

the material background. The black histogram is the spectrum of energies deposited in the active LAr volume from all the events. Neutrons that elastically scatter only once in the active LAr volume and nowhere else before being detected by the LSC are called pure (ideal) single elastic collision and their energy and TOF spectra are reported in blue in Fig. 5.8. The dashed red histogram is the sum of events between pure elastic scattering in the active volume and neurons that scatter only once in the active volume but might scatter somewhere else before or/and after the interaction with an argon atom in the active area. The multiple scatterings are illustrated in green and their contribution at small angles is ∼10%. Therefore the design of the detector demonstrates that the purpose of minimizing the multiple scattering is reached due to the small dimension of the active volume compared to the elastic neutron mean free path in LAr. Inelastic neutron scatters on argon are represented by a dashed orange histogram. In the case of inelastic scatters, the energy scale is not correct because there is a mixture between the energy deposited by an argon recoil and a photon from the deexcitation of an argon excited state. Therefore the effect of the γ-interaction on the total energy deposited would shift the inelastic scattering spectrum to higher energies compared to the region of interest for our study. Moreover, the same TOF cut used in the measured spectrum demonstrates that all the inelastic scatters are removed in the simulated energy deposited spectrum. The contributions of different classes of events are listed after the TOF cut the same used in the data in Tab. 5.4 and an example of the resulting spectrum at 25° is shown in Fig. 5.9. The black spectrum is used for the data-MC fit. The pure single

θ[°]	E_r[keV]	Pure single elastic scatt.[%]	External single elastic scatt.[%]	Multiple elastic scatt.[%]	Inelastic scatt.[%]
20	7.4±2.7	66.28	24.25	9.42	0.05
25	11.5±2.8	67.71	23.46	8.81	0.02
30	16.4±3.9	65.29	25.05	9.64	0.02
40	28.5±5.2	54.83	31.37	13.74	0.06
50	43.4±6.0	49.65	34.35	15.96	0.04
60	60.5±7.1	40.91	31.81	20.49	0.04
90	119.5±7.7	29	45.10	25.62	0.18

Table 5.4: Contributions to the deposited energy spectrum after TOF cut.

elastic scattering is the dominant process in the simulated recoil energy spectra for angles smaller than 40° and its contribution is decreasing as the angle increases. The decrease of the contribution of the pure single elastic scattering is well understood by looking at the differential elastic cross section for the 2.45 MeV neutrons with Ar shown in Fig. 5.10. This figure is obtained from ENDF/B-VII database. Since the 2.45 MeV neutrons are non relativistic the differential cross section in the center of mass and in the laboratory frame are similar. The smallest differential cross section is obtained around 80°, leading to the smallest event rate of neutrons for pure single elastic scattering.

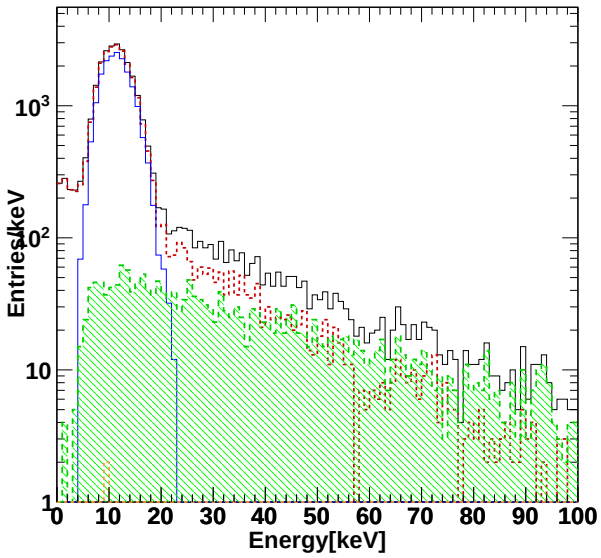

Figure 5.9: Example of the simulated recoil energy distribution at 25° after TOF cut. The color codes of the histograms are the same as in Fig. 5.8.

The position of the pure single elastic peak and its spread in the energy recoil distribution depends on the positions and sizes of the NG, the LSC and the LAr detector. The estimation of the uncertainties on recoil energies is determined by fitting a Gaussian function to the single elastic peak in the total spectrum over the energy range defined by the pure single elastic scatter spectrum. This procedure is applied for each scattering angle and their values are listed in Tab. 5.4.

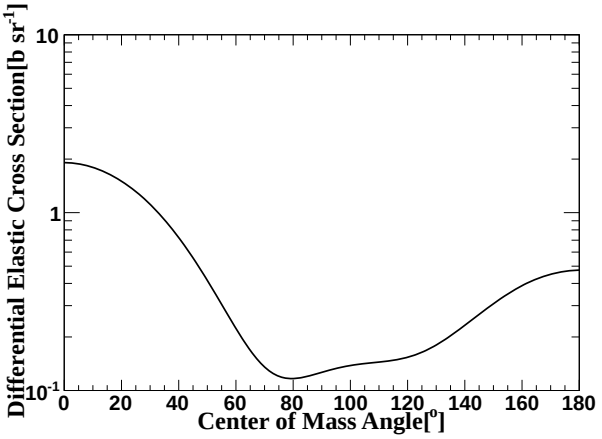

Figure 5.10: Neutron differential elastic scattering cross section on LAr as a function of the center-of-mass scattering angle for neutrons at 2.45 MeV (extracted from ENDF/B-VII database).

The measured TOF spectra are wider than the simulated distributions because the TOF calculated by the MC simulation only contains the geometrical resolution. Before applying a TOF cut to the energy recoil spectra, a finite TOF resolution was implemented by convoluting the simulated TOF values with a Gaussian function with a standard deviation of $\sigma_{exp} = 2.88$ ns. This value is determined by $\sigma_{exp} = \sqrt{\sigma_{tot}^2 - \sigma_{geo}^2}$, where σ_{tot} is the total resolution from the measured TOF spectra and σ_{geo} is the geometrical resolution from the MC distributions. The total and the geometrical resolution were deduced by fitting with the Gauss distribution the measured and simulated TOF spectrum respectively.

5.4 Procedure to extract $\mathcal{L}_{\text{eff}}$

A χ^2 minimization between the measured and the simulated spectrum has been performed to determine the energy dependence of the $\mathcal{L}_{\text{eff}}$. The χ^2 is computed as follows:

$$\chi^2(\mathcal{L}_{\text{eff},j}, R_j) = \frac{[h_i - h_{MC,i}(\mathcal{L}_{\text{eff},j}, R_j)]^2}{\sigma_i^2 + \sigma_{MC,i}^2} \tag{5.1}$$

where $\mathcal{L}_{\text{eff},j} \equiv \mathcal{L}_{\text{eff}}(E_{nr,j})$ and $R_j \equiv R(E_{nr,j})$, called resolution parameter are the free parameters. The measured and the simulated spectra are assigned by h_i and $h_{MC,i}$ for each bin i. Their corresponding uncertainties denoted by σ_i and $\sigma_{MC,i}$ are the square root of the entries for each bin i. The method developed in this work to extract $\mathcal{L}_{\text{eff}}$ is similar to the one used in [91]. The fit range has been chosen carefully for each angle in order to minimize the effect caused by the trigger efficiency and by higher energy in the tail of the energy recoil distribution. In general the trigger efficiency effect decrease $\mathcal{L}_{\text{eff}}$ while the high energy in the tail of the energy recoil distribution increase it. Fits were performed with different energy ranges and the fit ranges were selected when $\mathcal{L}_{\text{eff}}$ doesn't change significantly. The values of the fit range for the χ^2 computation are listed in Tab. 5.5. To obtain the simulated spectrum in photoelectron, the values of the deposited energy (in keV_{nr}) are first multiplied by $\mathcal{L}_{\text{eff}}$ under test and then by the light yield as describes in Eq. 5.2.

$$N_{p.e} = h_{MC,i} \times \mathcal{L}_{\text{eff}} \times Ly \quad . \tag{5.2}$$

A Poisson and a Gauss function are used to implement a smearing on the simulated spectrum: the number of photoelectrons $N_{p.e.}$ is allowed to fluctuate according to the Poisson distribution and the energy resolution is described by the standard deviation of the Gauss distribution defined as $R\sqrt{N_{p.e.}}$. The gain fluctuation from the PMTs is taken into account by convolving the nuclear recoil energy spectrum in photoelectrons with Gaussian distribution, which the standard deviation is defined as $R_{p.e.}\sqrt{N_{p.e.}}$. The parameter $R_{p.e.}$ is determined from the resolution of the measured mean single photoelectron distribution and found to be $R_{p.e.} = 0.4$ (Section 4.2.2.3). Then final simulated recoil energy spectrum is obtained by applying the measured trigger efficiency.

On the left side of Fig. 5.11 and Fig. 5.12, the χ^2 minimization map fit of the simulated to the measured recoil spectrum are shown for the scattering angles taken in Season02

and Season01 respectively.

θ[°]	E_r[keV]	χ^2 fit range [p.e.]	d.o.f	$\chi^2_{\min}$
25	11.5±2.8	[2, 38]	20	17.95
30	16.4±3.9	[2, 42]	22	19.76
40	28.5±5.2	[6, 48]	23	20.93
50	43.4±6.0	[22, 126]	28	36.76
60	60.5±7.1	[25, 135]	24	33.60
90	119.5±7.7	[30, 270]	14	15.42

Table 5.5: Fit Range used to compute the χ^2 map for each scattering angle with the corresponding number of degrees of freedom. The values $\chi^2_{\min}$ extracted from the rotated paraboloid fit are listed as well.

In order to extract the $\mathcal{L}_{\text{eff}}$ and R, a rotated paraboloid fit defined in Eq. 5.3 is used on the calculated χ^2 values map around the vicinity of its minimum denoted by χ^2_{min}.

$$\chi^2(\mathcal{L}_{\text{eff}}, R) = \chi^2_{min} + \left[\frac{(\mathcal{L}_{\text{eff}} - \mathcal{L}_{\text{eff},j})\,\cos\omega_j - (R - R_j)\,\sin\omega_j}{\mathcal{A}_j}\right]^2 + \left[\frac{(\mathcal{L}_{\text{eff}} - \mathcal{L}_{\text{eff},j})\,\sin\omega_j - (R - R_j)\,\cos\omega_j}{\mathcal{B}_j}\right]^2 \tag{5.3}$$

The paraboloid rotation angle is ω_j and the scaling parameters are $\mathcal{A}_{\text{j}}$ and $\mathcal{B}_{\text{j}}$. The advantage of this method is that the small variations on the χ^2 map are averaged out. The χ^2_{min}, determined by the rotated paraboloid fit, is indicated by the black dot in Fig. 5.11 and Fig. 5.12. The 1-σ and the 2-σ contour confidence level for $\mathcal{L}_{\text{eff},j}$ and R_j are also illustrated by the black and the yellow lines. The contours are obtained by setting on the left side of Eq. 5.3 $\chi^2_{min} + \Delta\chi^2_{\text{1-}\sigma}$ for 1-σ variation (with $\Delta\chi^2_{\text{1-}\sigma} = 2.30$) and $\chi^2_{min} + \Delta\chi^2_{\text{2-}\sigma}$ for 2-σ variation (with $\Delta\chi^2_{\text{2-}\sigma} = 6.18$). On the right side, the measured nuclear recoil spectrum is represented by the black dots with the corresponding superimposed best fit of MC generated recoil spectrum, being represented by the red histogram. The effect of 1-σ variation of $\mathcal{L}_{\text{eff}}$ and R around the best fit generated spectrum is represented by the purple band. The blue dashed line corresponds to the fit range used to compute the χ^2.

For the 20° scattering angle the procedure to extract $\mathcal{L}_{\text{eff}}$ is impossible since the mean of the energy recoil spectrum is in the region of the trigger efficiency roll-off. The two strongest anti-correlations are observed for the lowest energy recoil data taken with the improved trigger setting of Season02 (11.5 keV_{nr}) and for the lowest energy recoil data with the trigger setting Season01 (43.4 keV_{nr}), for which the effect of the roll-off being more pronounced. This effect can be explained by the fact that the resolution parameter R has to increase to match the measured recoil energy spectra because the probability to detect photons near the roll-off trigger efficiency region decreases, lowering down the value of $\mathcal{L}_{\text{eff}}$. This effect disappears progressively for energies of which the mean of the elastic peak is far from the region of the trigger efficiency roll-off.

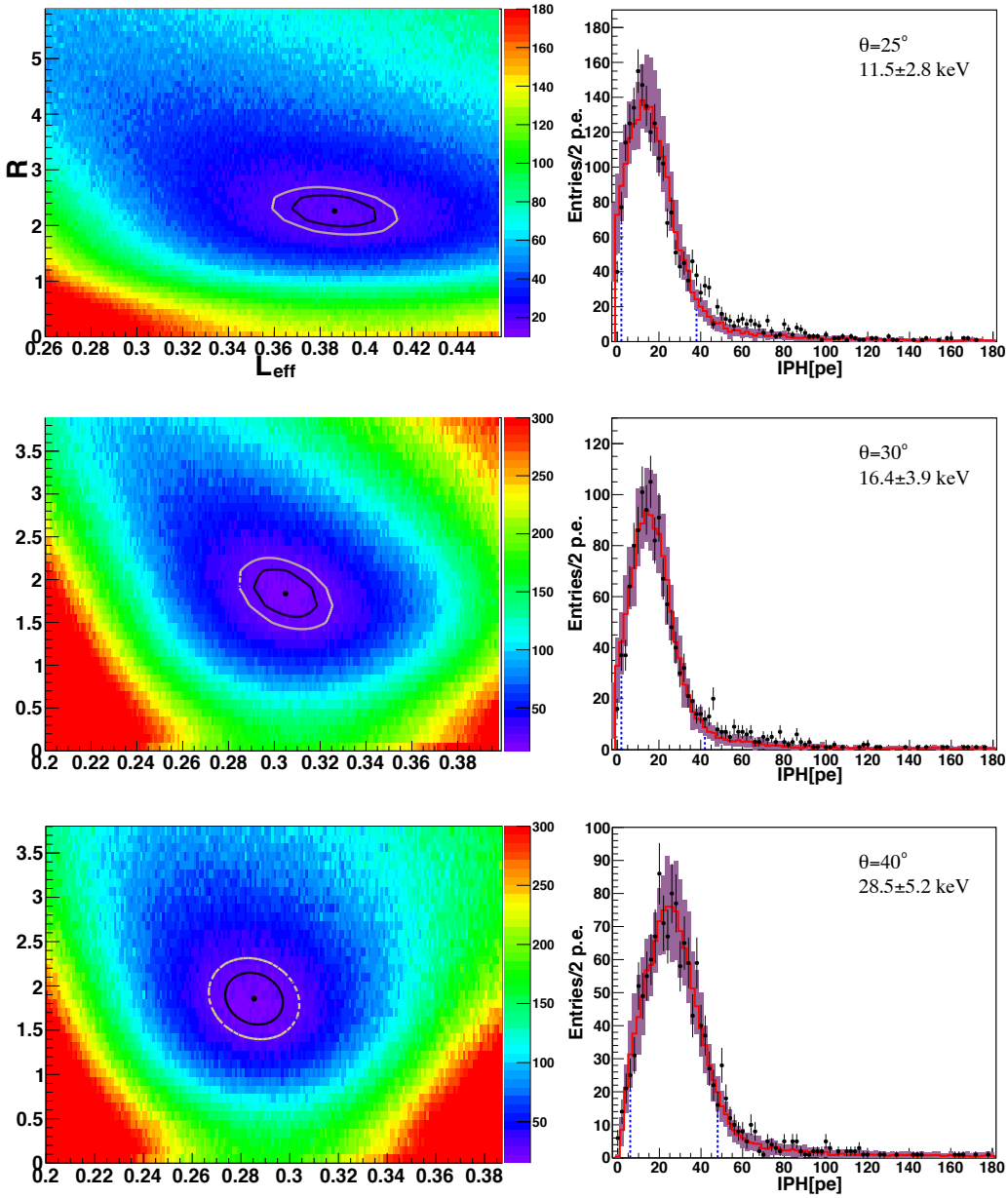

Figure 5.11: Left: χ^2 maps as a function of $\mathcal{L}_{\text{eff}}$ and R. Right: corresponding MC fits of the energy recoil spectra (red) to the data (black) for the scattering angles 25°, 30° and 40° (Season02).

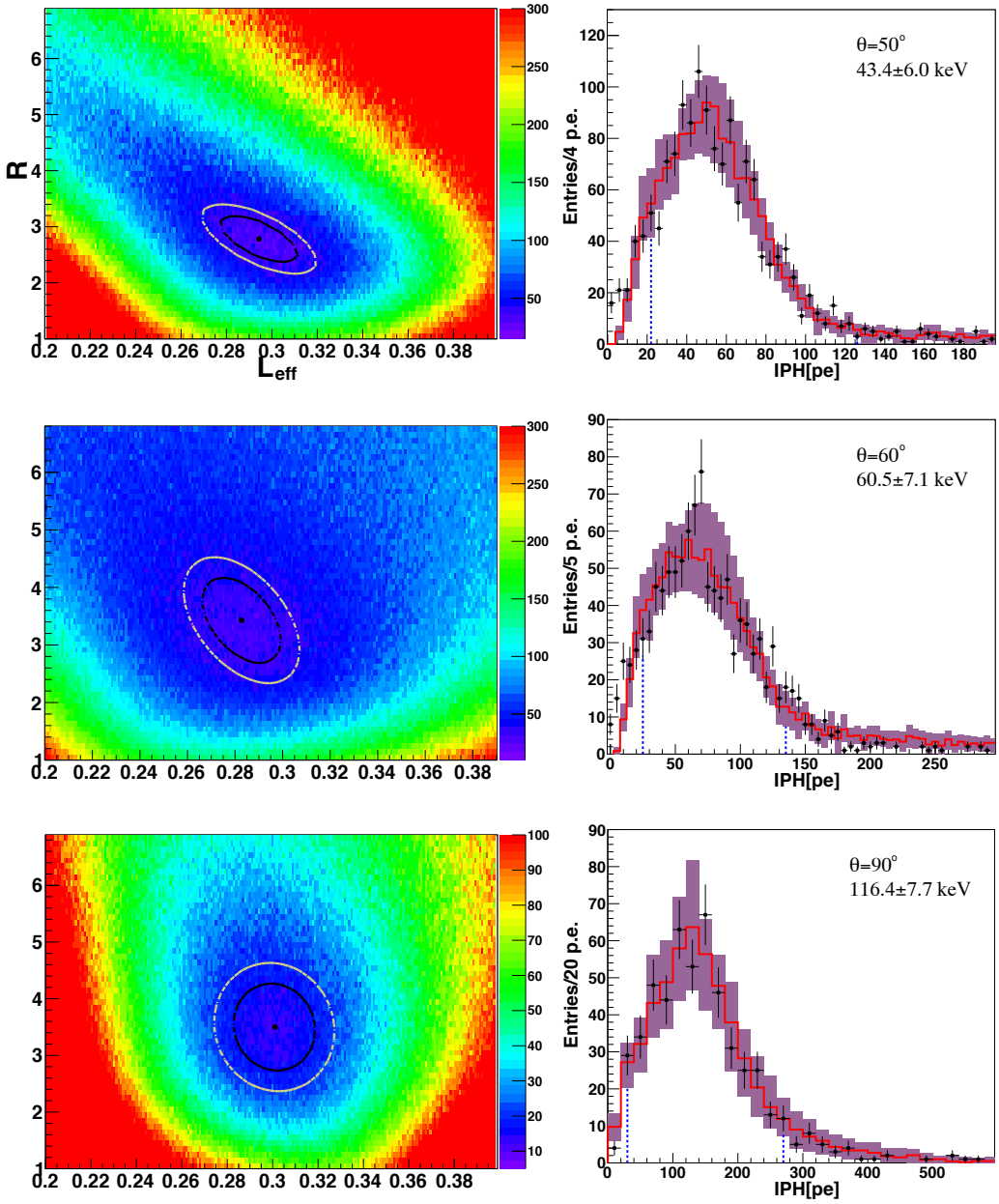

Figure 5.12: Left: χ^2 maps as a function of $\mathcal{L}_{\text{eff}}$ and R. Right: corresponding MC fits of the energy recoil spectra (red) to the data (black) for the scattering angles 50°, 60° and 90° (Season01).

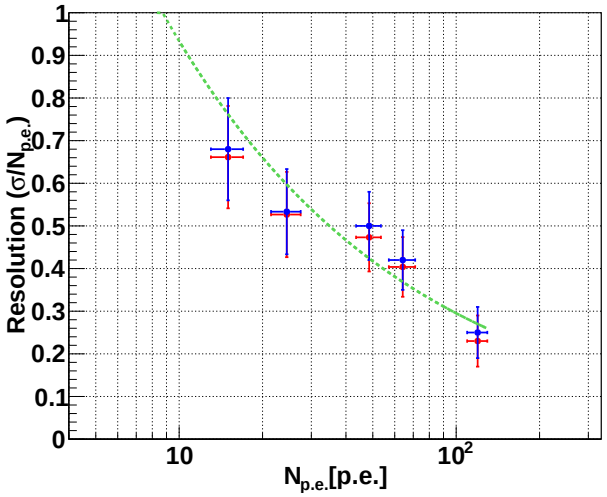

Figure 5.13: Energy resolution obtained by fitting the measured spectra of nuclear recoils above 11.5 keV$_{nr}$ with a Gaussian function are represented by blue circles and the ones determined by the χ^2 minimization are shown in red.

The reliability of the procedure to extract $\mathcal{L}_{\text{eff}}$ by including an additional parameter (the resolution parameter R) in the χ^2 minimization has already been discussed by J. Collar [126] and G.Plante [127]. In [126], the author suggested that the implementation of the resolution parameter as a free parameter in the fit for the comparison between the measured and the simulated energy recoil distributions risked to bias towards larger values and reduce the uncertainties. Instead of leaving the energy resolution as a free parameter, the simulated energy recoil distributions should be convoluted with an energy resolution function. An extensive study has been performed on the possible systematic effect on the values of $\mathcal{L}_{\text{eff}}$ by G.Plante. In this work [127], the analysis procedure has been repeated by fixing the energy dependence of the resolution with two models parameterized as $a\sqrt{E}$ and $a\sqrt{E} + bE$. No significant deviation has been observed between the resulting values of $\mathcal{L}_{\text{eff}}$ obtained from these two models and those determined by leaving the resolution as a free parameter. Moreover, the implementation of a parameter correlated to $\mathcal{L}_{\text{eff}}$ during the fit procedure should increase the uncertainty contrary to what was claimed in [126].

In order to verify this remark an independent test has been performed by repeating the analysis in the case where the resolution parameter is fixed by a function, in a similar way to G.Plante. Measured nuclear recoils spectra whose the elastic peak is above the trigger efficiency roll-off (11.5 keV$_{nr}$) were fitted with Gaussian functions. For each energy resolution defined as $\sigma/N_{p.e.}$, the contribution of the spread of the energy due to the finite size of the detector is subtracted quadratically. In Fig. 5.13 the energy resolutions, obtained by the Gaussian fit (blue data), are fitted using the model for the energy dependence of the energy resolution $\sigma = a\sqrt{N_{p.e.}}$ with $a = 2.75 \pm 0.25$. The green dashed line describing well the data, represents the model used to obtain the energy resolution. The red data shows

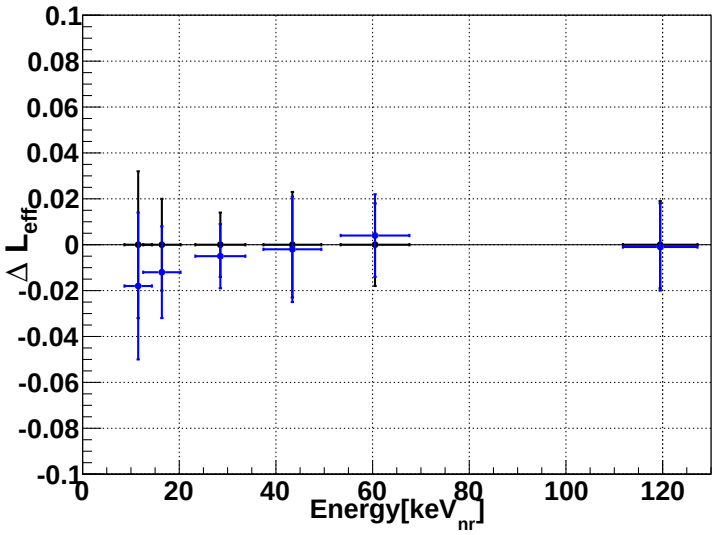

Figure 5.14: Effect in the $\mathcal{L}_{\text{eff}}$ of fixing the resolution parameter (blue data) instead of leaving it as a free parameter (black data) during the data-MC fit.

the energy resolution determined from the spectra obtained by the χ^2 minimization.

Fig. 5.14 shows the variation of the $\mathcal{L}_{\text{eff}}$ by fixing the resolution parameter (blue data) instead of leaving it as a free parameter (black data). The variation are within the errors bars and confirm there is no significant deviation between the determination of the $\mathcal{L}_{\text{eff}}$ by leaving the energy resolution as a free parameter and by fixing it by a function.

5.5 Systematic errors

This section treats the different possible systematic contributions leading to the uncertainties on $\mathcal{L}_{\text{eff}}$. The statistical uncertainty Δ_{stat} is given by the 1-σ contour of the rotated paraboloid fits to the χ^2 map. The sources of systematic uncertainties taken into account are as follows:

- The uncertainty on the light yield measured with the ^{241}Am source Δ_{LY} is determined by the error on the mean calibration constant which is estimated to 2.1% and 1.6% for the Season01 and Season02 runs respectively.
- For each measured scattering angle, the error on the angular position of the LSC Δ_θ is set at 0.5°.
- Δ_{trig} the effect of the trigger efficiency roll-off responsible for the uncertainty in the $\mathcal{L}_{\text{eff}}$. This uncertainty is determined by changing the values of parameters in Eq. 4.27 defining the trigger efficiency.

All the contributions from different sources of uncertainties mentioned above are listed in Tab. 5.6. The calibration errors Δ_{LY} leads to the largest contribution to the systematic

$\theta[^{\circ}]$	E_r[keV]	$\mathcal{L}_{\text{eff}}$	$\Delta_{\mathcal{L}_{\text{eff}}}$	Δ_{stat}	Δ_{LY}	Δ_{trig}	Δ_{θ}
25	11.5±2.8	0.386	0.032	0.0185	0.0068	0.0252	0.0028
30	16.4±3.9	0.305	0.020	0.0142	0.0054	0.0126	0.0010
40	28.5±5.2	0.285	0.014	0.0127	0.0051	0.0013	0.0007
50	43.4±6.0	0.294	0.023	0.0159	0.0064	0.0154	0.0006
60	60.5±7.1	0.283	0.018	0.0167	0.0062	0.0022	0.0004
90	119.5±7.7	0.301	0.019	0.0177	0.0064	0.0000	0.0000

Table 5.6: Contributions of various sources of uncertainties on $\mathcal{L}_{\text{eff}}$ at each scattering angle.

uncertainties except for the measured scattering angles for which the mean value of the peak is close to the trigger efficiency roll-off. In this case, the uncertainty caused by the trigger efficiency becomes the largest systematic uncertainty. A jump on the Δ_{trig} for measured angle 50^{o} can be explained due to the trigger settings of Season01 for which the effect of the roll-off being more pronounced. The total uncertainties on $\mathcal{L}_{\text{eff}}$ denoted by $\Delta_{\mathcal{L}_{\text{eff}}}$ is the squared sum of all the errors.

$$\Delta_{\mathcal{L}_{\text{eff}}} = \sqrt{\Delta^2_{stat} + \Delta^2_{LY} + \Delta^2_{trig} + \Delta^2_{\theta}} \tag{5.4}$$

The spread of the energy of the incoming neutrons is covered by Monte Carlo simulation since 100 millions of neutrons are generated in 4π with the exact geometry of the neutron generator, it's shielding, the LAr cell and the LSC. For each interaction in the LAr cell the energy and the direction of the incoming and outcoming neutrons are recorded. Therefore under these assumptions the spread of the incoming neutron energy is well known.

5.6 $\mathcal{L}_{\text{eff}}$ results

The results of the $\mathcal{L}_{\text{eff}}$ obtained by applying this method are listed in Tab. 5.7 with their uncertainties discussed in Section 5.5. The errors on the resolution parameter R contain only the statistical uncertainty. The corresponding plot of $\mathcal{L}_{\text{eff}}$ as a function of the energy recoil with the previous measurement from micro-CLEAN and WArP is shown in Fig. 5.15. The theoretical behaviour of luminescence quenching in LAr described in Section 2.5 by Mei's model is also represented by the blue dashed line.

These results are compatible with those obtained from $IPHA$ and the CR described in Section 5.2. As already mentioned, $\mathcal{L}_{\text{eff}}$ describes a flat behaviour for energies above 16.4 keV_{nr} with a mean value $\langle \mathcal{L}_{\text{eff}} \rangle = 0.296 \pm 0.019$. However, our $\mathcal{L}_{\text{eff}}$ values are systematically higher than those obtained by micro-CLEAN for the same energy range. This could be explained by the fact that interactions outside the active volume might not be well described in micro-CLEAN's work, hence the observation that the Monte Carlo simulation does not reproduce exactly the measured background shape [70]. This material background causes a decrease of the initial energy of the incoming neutron, producing

θ[°]	E_r[keV]	$\mathcal{L}_{eff}$	R
25	11.5±2.8	0.386±0.032	2.26±0.29
30	16.4±3.9	0.305±0.020	1.84±0.28
40	28.5±5.2	0.285±0.014	1.86±0.30
50	43.4±6.0	0.294±0.023	2.79±0.42
60	60.5±7.1	0.283±0.018	3.43±0.72
90	119.5±7.7	0.301±0.019	3.49±0.74

Table 5.7: Results of the $\mathcal{L}_{eff}$ as a function of scattering angle. The values of the resolution parameter R are also listed.

a bias in the $\mathcal{L}_{eff}$ values if it is not well reproduced by the simulation. Moreover, a detector consisting of 8" active volume (3.14 ℓ of LAr) might not be ideal to minimize the amount of the background produced by multiple scatterings and this process might not be negligible compared to the pure single neutron elastic scattering.

Our result below 16.4 keV_{nr} is consistent compared to the one obtained by micro-CLEAN within errors and confirms the observed upturn which is in contradiction with Mei's model. However, recently the NEST group has applied an ansatz model based on the work from F. Berzukov *et al.* in LXe [128] and showed the upturn at low energy. In this work [129], the authors considered various possible modifications of the electronic stopping powers of LXe, including a parameterization in such a way as to compare the resulting scintillation and ionization model with the experimental data in LXe. When

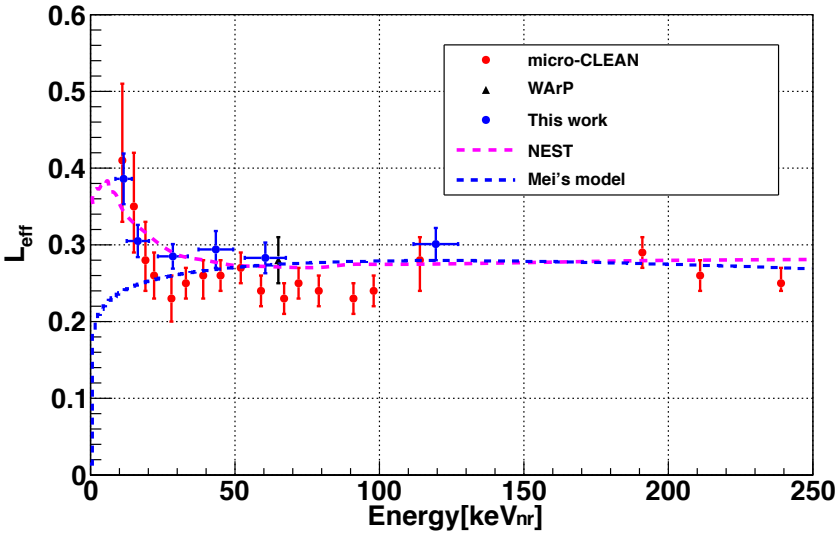

Figure 5.15: Measured $\mathcal{L}_{eff}$ values in LAr as a function of recoil energy (blue), compared to the previous measurements by micro-CLEAN (red) and WArP (black point) experiment. The blue and pink dashed lines are the $\mathcal{L}_{eff}$ values predicted by Mei and NEST models, respectively.

changing the atomic number Z and the atomic mass A on Berzukov's work, the empirical curve of $\mathcal{L}_{\text{eff}}$ in LAr represented by the pink dashed line is in agreement with our data and exhibits this upturn at low energy, in contrast to the case of LXe, for which the values of $\mathcal{L}_{\text{eff}}$ decrease at low energies.

Conclusions

Seven angles were recorded to measure the $\mathcal{L}_{\text{eff}}$ at zero electric field from 11.5 keV$_{nr}$ to 119.5 keV$_{nr}$ (the data recorded at 7.4 keV$_{nr}$ could not be analysed). A realistic Monte Carlo simulation has been developed to compare the simulated recoil energy spectra with those measured. Due to the design of the LAr detector and to the neutron differential elastic cross section, the results of the MC simulation showed that the pure single elastic scattering events are the main contribution in the recoil energy spectra after the TOF cut. For energies below 40 keV$_{nr}$ the contribution of pure single elastic scattering events is more than 50% while the contamination of multiple scattering events and neutron inelastic events are negligible for the same energy range.

A χ^2 minimization was performed leaving $\mathcal{L}_{\text{eff}}$ and R as free parameters. The results lead to a mean value $\langle \mathcal{L}_{\text{eff}} \rangle = 0.296 \pm 0.019$ for energies above 16.4 keV$_{nr}$. The result obtained at 11.5 keV$_{nr}$ confirmed the energy upturn as already observed by micro-CLEAN and as predicted by NEST, which is in disagreement with Mei's work. Another method, based simply on $IPHA$ and CR was used to measured $\mathcal{L}_{\text{eff}}$ which the results were consistent in between the errors.

The uncertainties in the extraction on the $\mathcal{L}_{\text{eff}}$ are dominated by the effect of the trigger efficiency roll-off at low energy. This contribution becomes smaller when the mean of the recoil energy spectra is far from this region. In this case the uncertainties on the $\mathcal{L}_{\text{eff}}$ is only limited to the statistical errors.

Conclusion and Outlook

A neutron scattering experiment facility has been designed with a small liquid argon (LAr) detector (0.2 ℓ) to obtain a precise measurement of the relative scintillation efficiency $\mathcal{L}_{\text{eff}}$. The light yield with the ^{241}Am source is found to be at 3.75 ± 0.08 photoelectrons (p.e.)/keV$_{ee}$. The LAr detector is calibrated with several radioactive source emitting γ-rays to investigate the linearity of the response to electronic recoils in LAr. For an energy range from 32 keV$_{ee}$ to 1060 keV$_{ee}$ (electron equivalent energy "ee") no significant deviation has been observed from linearity.

The relative population density in the singlet $^1\Sigma_u^-$ and the triplet $^3\Sigma_u^+$ argon excimer states has been studied for electron, nuclear and α recoils as a function of energy. At low energies the values of the component ratio CR (contribution of the singlet to the total scintillation light) converge to about 10 keV$_{ee}$ for electron and nuclear recoils and a positive correlation between the linear energy transfer (LET) and the CR is observed. For electron recoils, the values of the CR are close to the ones expected from statistically populated singlet and triplet states ($^1\Sigma_u^-$/ $(^1\Sigma_u^- + {}^3\Sigma_u^+) \sim 0.25$) in the region of the lowest ionization densities. For nuclear recoils, a rise of the CR is measured to be 50% to 75% between 20 and 200 keV$_{ee}$. The relative scintillation efficiency for α-particles $\mathcal{L}_{\text{eff}}^{\alpha}$ in the MeV range is determined to be 0.74 ± 0.04 and the values of the CR are slightly smaller compared to recoiling nuclei.

We confirm scintillation light quenching in liquid argon by the presence of impurities being of the same physical nature as the one observed in gaseous argon [125]. The relative intensity of the triplet state decreases linearly with impurities whereas that of the singlet state remains constant. Therefore a new technique is developed to correct the scintillation light yield for impurities and taking into account the third component around 100 ns in the distribution of the scintillation light. The contribution of the third component in the total scintillation light is 3% and 13% for electron and nuclear recoils respectively.

Thanks to the stability of the experimental setup, data were recorded, nearly without interruption during two run periods for the $\mathcal{L}_{\text{eff}}$ measurements at zero electric field. Data at several scattering angles were recorded, corresponding to recoil energies between $\sim$7 keV$_{nr}$ and $\sim$120 keV$_{nr}$ (nuclear recoil energy "nr") induced by monochromatic neutrons of 2.45 MeV. The $\mathcal{L}_{\text{eff}}$ values are determined by comparing the measured recoil energy spectra with those simulated by Monte Carlo, leaving $\mathcal{L}_{\text{eff}}$ and the energy resolution R as free parameters during the χ^2 minimization. For a realistic approach of the experiment the simulation includes several contributions: multiple scattering, interactions outside the

active volume and inelastic collisions.

The extraction of $\mathcal{L}_{\text{eff}}$ is quite challenging near the low energy trigger efficiency roll-off region where the measured signal is suppressed. The method used for the determination of $\mathcal{L}_{\text{eff}}$ is limited to angles above 20° because the average of the recoil energy is situated within the trigger efficiency roll-off region. Our result at low energies is the most precise measurement of $\mathcal{L}_{\text{eff}}$ in LAr. The $\mathcal{L}_{\text{eff}}$ values describes a flat behavior between 16 keV$_{nr}$ and 120 keV$_{nr}$ with a mean value $\langle\mathcal{L}_{\text{eff}}\rangle = 0.296 \pm 0.019$. The result obtained at 11 keV$_{nr}$ confirms the increase of $\mathcal{L}_{\text{eff}}$ at low energy observed by micro-CLEAN [70] but with higher precision. This tendency is in disagreement with the model of Mei [89] but agrees with the recent prediction from LXe, extrapolated to LAr by NEST [129]. At low energies the determination of $\mathcal{L}_{\text{eff}}$ is crucial for direct dark matter searches in LAr. A detailed understanding of the physical processes causing the energy upturn of $\mathcal{L}_{\text{eff}}$ in LAr would be desirable. The new result of the $\mathcal{L}_{\text{eff}}$ obtained in this thesis implies an increase of the WIMP detection sensitivity in argon at the energy region where the upturn is observed.

The $\mathcal{L}_{\text{eff}}$ measurement at low energy is mainly limited by the trigger efficiency roll-off near to the elastic peak. An improvement of the trigger setting and a better analysis of the energy dependence of the trigger efficiency is necessary to lower the threshold. In the future an upgrade of the neutron scattering experiment using PMTs with larger quantum efficiencies (∼30%) to increase the light yield, can also improve the $\mathcal{L}_{\text{eff}}$ measurement at low energy. An improvement of the cleaning system is also being planned to reduce the uncertainties in the determination of the light yield. An internal electric field will also be implemented to determine field and energy dependencies of light and charge yields in LAr at energies relevant to dark matter searches.

Bibliography

[1] J. Bekenstein and M. Milgrom, "Does the missing mass problem signal the breakdown of Newtonian gravity?", *Astrophys.J.* **286** (1984) 7–14. doi:10.1086/162570.

[2] V. C. Rubin and J. Ford, W. Kent, "Rotation of the Andromeda Nebula from a Spectroscopic Survey of Emission Regions", *Astrophys.J.* **159** (1970) 379–403. doi:10.1086/150317.

[3] K. Begeman, A. Broeils, and R. Sanders, "Extended rotation curves of spiral galaxies: Dark haloes and modified dynamics", *Mon.Not.Roy.Astron.Soc.* **249** (1991) 523.

[4] N. Benitez, T. Broadhurst, H. Ford et al., "Galaxy Cluster Abell 1689 Warps Space",.

[5] F. Zwicky, "Spectral displacement of extra galactic nebulae", *Helv.Phys.Acta* **6** (1933) 110–127.

[6] D. Walsh, R. Carswell, and R.Weymann, "0957+561-A, B - twin quasistellar objects or gravitational lens", *Nature* **279** (1979) 381–384. doi:10.1038/279381a0.

[7] J. A. Tyson, G. P. Kochanski, and I. P. Dell'Antonio, "Detailed Mass Map of CL 0024+1654 from Strong Lensing", *The Astrophysical Journal Letters* **498** (1998) L107.

[8] D. Clowe, M. Bradač, A. H. Gonzalez et al., "A Direct Empirical Proof of the Existence of Dark Matter", *The Astrophysical Journal Letters* **648** (2006) L109.

[9] Planck Collaboration, "Planck 2013 results. I. Overview of products and scientific results", arXiv:1303.5062.

[10] B. Fuchs, "Ngc2613, 3198, 6503, 7184: case studies against 'maximum' disks", arXiv:astro-ph/9812048.

[11] Y. Fukuda, T. Hayakawa, E. Ichihara et al., "Measurements of the Solar Neutrino Flux from Super-Kamiokande's First 300 Days", *Phys. Rev. Lett.* **81** (1998) 1158–1162. doi:10.1103/PhysRevLett.81.1158.

[12] G. Bertone, D. Hooper, and J. Silk, "Particle dark matter: Evidence, candidates and constraints", *Phys.Rept.* **405** (2005) 279–390, arXiv:hep-ph/0404175. doi:10.1016/j.physrep.2004.08.031.

[13] S. Dodelson, E. I. Gates, and M. S. Turner, "Cold dark matter models", *Science* **274** (1996) 69–75, arXiv:astro-ph/9603081. doi:10.1126/science.274.5284.69.

[14] M. Loewenstein, A. Kusenko, and P. L. Biermann, "New Limits on Sterile Neutrinos from Suzaku Observations of the Ursa Minor Dwarf Spheroidal Galaxy", *Astrophys.J.* **700** (2009) 426–435, arXiv:0812.2710. doi:10.1088/0004-637X/700/1/426.

[15] A. Kusenko and G. SegrÃ¨, "Neutral current induced neutrino oscillations in a supernova", *Physics Letters B* **396** (1997) 197 – 200. doi:http://dx.doi.org/10.1016/S0370-2693(97)00121-4.

[16] R. D. Peccei and H. R. Quinn, "Constraints imposed by CP conservation in the presence of pseudoparticles", *Phys. Rev. D* **16** (1977) 1791–1797. doi:10.1103/PhysRevD.16.1791.

[17] L. J. Rosenberg, "ADMX DarkMatter Axion Search", *AIP Conf. Proc.* **698** (2004) 332. doi:10.1063/1.1664252.

[18] H. Primakoff, "Photo-Production of Neutral Mesons in Nuclear Electric Fields and the Mean Life of the Neutral Meson", *Phys. Rev.* **81** (1951) 899–899. doi:10.1103/PhysRev.81.899.

[19] D. Autiero, B. Beltràn, J. M. Carmona et al., "The CAST time projection chamber", *New Journal of Physics* **9** (2007) 171.

[20] G. Jungman, M. Kamionkowski, and K. Griest, "Supersymmetric dark matter", *Phys.Rept.* **267** (1996) 195–373, arXiv:hep-ph/9506380. doi:10.1016/0370-1573(95)00058-5.

[21] E. W. Kolb and M. S. Turner, "The Early Universe: Frontiers in Physics". (Perseus Books, 1989).

[22] S. P. Martin, "A Supersymmetry primer", arXiv:hep-ph/9709356.

[23] G. Servant and T. M. Tait, "Is the lightest Kaluza-Klein particle a viable dark matter candidate?", *Nucl.Phys.* **B650** (2003) 391–419, arXiv:hep-ph/0206071. doi:10.1016/S0550-3213(02)01012-X.

[24] A. Birkedal, A. Noble, M. Perelstein et al., "Little Higgs dark matter", *Phys.Rev.* **D74** (2006) 035002, arXiv:hep-ph/0603077. doi:10.1103/PhysRevD.74.035002.

[25] PAMELA Collaboration, "An anomalous positron abundance in cosmic rays with energies 1.5-100 GeV", *Nature* **458** (2009) 607–609, arXiv:0810.4995. doi:10.1038/nature07942.

[26] A. Kounine, "Status of the AMS Experiment", arXiv:1009.5349.

[27] H.E.S.S. Collaboration, "Probing the ATIC peak in the cosmic-ray electron spectrum with H.E.S.S", *Astron.Astrophys.* **508** (2009) 561, arXiv:0905.0105.

[28] MAGIC Collaboration, "Performance of the MAGIC stereo system obtained with Crab Nebula data", *Astropart.Phys.* **35** (2012) 435–448, arXiv:1108.1477. doi:10.1016/j.astropartphys.2011.11.007.

[29] W. de Boer, C. Sander, V. Zhukov et al., "Egret excess of diffuse galactic gamma rays as tracer of dark matter", *Astron.Astrophys.* **444** (2005) 51, arXiv:astro-ph/0508617. doi:10.1051/0004-6361:20053726.

[30] Fermi LAT Collaboration, "Measurement of the Cosmic Ray e+ plus e- spectrum from 20 GeV to 1 TeV with the Fermi Large Area Telescope", *Phys.Rev.Lett.* **102** (2009) 181101, arXiv:0905.0025. doi:10.1103/PhysRevLett.102.181101.

[31] ANTARES Collaboration, "Time Calibration of the ANTARES Neutrino Telescope", *Astropart.Phys.* **34** (2011) 539–549, arXiv:1012.2204. doi:10.1016/j.astropartphys.2010.12.004.

[32] F. Halzen, "Astroparticle physics with high energy neutrinos: from amanda to icecube", *Eur.Phys.J.* **C46** (2006) 669–687, arXiv:astro-ph/0602132. doi:10.1140/epjc/s2006-02536-4.

[33] E. Tempel, A. Hektor, and M. Raidal, "Fermi 130 GeV gamma-ray excess and dark matter annihilation in sub-haloes and in the Galactic centre", *JCAP* **1209** (2012) 032, arXiv:1205.1045.

[34] C. Rott, "Review of Indirect WIMP Search Experiments", arXiv:1210.4161.

[35] A. K. Drukier, K. Freese, and D. N. Spergel, "Detecting cold dark-matter candidates", *Phys. Rev. D* **33** (Jun, 1986) 3495–3508. doi:10.1103/PhysRevD.33.3495.

[36] D. N. Spergel, "Motion of the Earth and the detection of weakly interacting massive particles", *Phys. Rev. D* **37** (Mar, 1988) 1353–1355. doi:10.1103/PhysRevD.37.1353.

[37] J. Lewin and P. Smith, "Review of mathematics, numerical factors, and corrections for dark matter experiments based on elastic nuclear recoil", *Astroparticle Physics* **6** (1996) 87 – 112. doi:http://dx.doi.org/10.1016/S0927-6505(96)00047-3.

[38] V. Chepel and H. AraÃºjo, "Liquid noble gas detectors for low energy particle physics", *Journal of Instrumentation* **8** (2013) R04001.

[39] S. Ahlen, F. A. III, R. Brodzinski et al., "Limits on cold dark matter candidates from an ultralow background germanium spectrometer", *Physics Letters B* **195** (1987) 603 – 608. doi:10.1016/0370-2693(87)91581-4.

[40] F. Pröbst, G. Angloher, M. Bruckmayer et al., "Results of CRESST phase I", *Nuclear Physics B - Proceedings Supplements* **110** (2002) 67 – 69. doi:10.1016/S0920-5632(02)01453-6.

[41] P. Gorla, R. Ardito, C. Arnaboldi et al., "Cuoricino and CUORE detectors: developing big arrays of large mass bolometers for rare events physics", *Nuclear Physics B - Proceedings Supplements* **150** (2006) 214 – 218. Proceedings of the 9th Topical Seminar on Innovative Particle and Radiation Detectors. doi:10.1016/j.nuclphysbps.2004.11.387.

[42] A. Broniatowski, X. Defay, E. Armengaud et al., "A new high-background-rejection dark matter Ge cryogenic detector", *Physics Letters B* **681** (2009) 305 – 309. doi:10.1016/j.physletb.2009.10.036.

[43] T. A. Perera, D. Abrams, D. S. Akerib et al., "Present results and future goals of the Cryogenic Dark Matter Search", *AIP Conf. Proc.* **605** (2002) 485. doi:10.1063/1.1457691.

[44] G. Angloher, C. Bucci, P. Christ et al., "Limits on WIMP dark matter using scintillating CaWO4 cryogenic detectors with active background suppression", *Astropart.Phys.* **23** (2005) 325–339, arXiv:astro-ph/0408006. doi:10.1016/j.astropartphys.2005.01.006.

[45] S. Cebriàn, N. Coron, G. Dambier et al., "The ROSEBUD experiment at Canfranc : 2001 report", *Nuclear Physics B - Proceedings Supplements* **110** (2002) 97 – 99. doi:10.1016/S0920-5632(02)01463-9.

[46] CoGeNT Collaboration, "Search for an Annual Modulation in a p-Type Point Contact Germanium Dark Matter Detector", *Phys. Rev. Lett.* **107** (2011) 141301. doi:10.1103/PhysRevLett.107.141301.

[47] DAMA Collaboration, "The DAMA/LIBRA apparatus", *Nucl.Instrum.Meth.* **A592** (2008) 297–315, arXiv:0804.2738. doi:10.1016/j.nima.2008.04.082.

[48] A. Hime, "DEAP & CLEAN detectors for low energy particle astrophysics", *AIP Conf. Proc.* **842** (2006) 852–854. doi:10.1063/1.2402618.

[49] G. Alner, H. Araujo, G. Arnison et al., "First limits on nuclear recoil events from the ZEPLIN I galactic dark matter detector", *Astroparticle Physics* **23** (2005) 444 – 462. doi:10.1016/j.astropartphys.2005.02.004.

[50] K. Abe and the XMASS Collaboration, "The XMASS experiment", *Journal of Physics: Conference Series* **120** (2008) 042022.

[51] A. Rubbia, "ArDM: a ton-scale liquid Argon experiment for direct detection of Dark Matter in the Universe", *Journal of Physics: Conference Series* **39** (2006) 129.

[52] E. Aprile, K. Giboni, P. Majewski et al., "The XENON dark matter search experiment", *New Astronomy Reviews* **49** (2005) 289–295. Sources and Detection of Dark Matter and Dark Energy in the Universe. 6th UCLA Symposium on Sources and Detection of Dark Matter and Dark Energy in the Universe. doi:10.1016/j.newar.2005.01.035.

[53] D. N. McKinsey, D. Akerib, S. Bedikian et al., "The LUX dark matter search", *Journal of Physics: Conference Series* **203** (2010) 012026.

[54] V. N. Lebedenko, H. M. Araùjo, E. J. Barnes et al., "Results from the first science run of the ZEPLIN-III dark matter search experiment", *Phys. Rev. D* **80** (2009) 052010. doi:10.1103/PhysRevD.80.052010.

[55] H. Gong, K. Giboni, X. Ji et al., "The Cryogenic System for the Panda-X Dark Matter Search Experiment", *JINST* **8** (2013) P01002, arXiv:1207.5100. doi:10.1088/1748-0221/8/01/P01002.

[56] N. Arkani-Hamed, S. Dimopoulos, and G. Dvali, "The hierarchy problem and new dimensions at a millimeter", *Physics Letters B* **429** (1998) 263 – 272. doi:http://dx.doi.org/10.1016/S0370-2693(98)00466-3.

[57] CMS Collaboration, "Search for Dark Matter and Large Extra Dimensions in pp Collisions Yielding a Photon and Missing Transverse Energy", *Phys.Rev.Lett.* **108** (2012) 261803, arXiv:1204.0821. doi:10.1103/PhysRevLett.108.261803.

[58] R. Bernabei, P. Belli, F. Cappella et al., "First results from DAMA/LIBRA", (2008). Proceedings of the 4th Patras Workshop on Axions, WIMPs and WISPs. doi:10.3204/DESY-PROC-2008-02/incicchitti_antonella.

[59] CoGeNT Collaboration, "CoGeNT: A Search for Low-Mass Dark Matter using p-type Point Contact Germanium Detectors", *Phys.Rev.* **D88** (2013) 012002, arXiv:1208.5737. doi:10.1103/PhysRevD.88.012002.

[60] G. Angloher, M. Bauer, I. Bavykina et al., "Results from 730 kg days of the CRESST-II Dark Matter search", *The European Physical Journal C* **72** (2012) 1–22. doi:10.1140/epjc/s10052-012-1971-8.

[61] T. C. I. Collaboration, "Dark matter search results from the CDMS-II experiment. Science", *Science* **327** (2010) 1619–1621. doi:10.1126/science.1186112.

[62] CDMS Collaboration, "Dark Matter Search Results Using the Silicon Detectors of CDMS II", *Phys.Rev.Lett.* (2013) arXiv:1304.4279.

[63] XENON100 Collaboration, "Dark Matter Results from 225 Live Days of XENON100 Data", *Phys.Rev.Lett.* **109** (2012) 181301, arXiv:1207.5988. doi:10.1103/PhysRevLett.109.181301.

[64] W. H. Lippincott, "Direct detection of dark matter with liquid argon and neon". PhD thesis, Yale U., Yale, 2010.

[65] E.Lemmon, M.McLinden, and D.Friend *NIST Chemistry WebBook, NIST Standard Reference Database Number 69, ch.* Thermophysical Properties of Fluid Systems (National Institute of Standards and Technology,Gaithersburg,MD, 2009), chap. Thermophysical Properties of Fluid Systems.

[66] C. Rubbia, M. Antonello, P. Aprili et al., "Underground operation of the ICARUS T600 LAr-TPC: first results", *Journal of Instrumentation* **6** (2011) P07011.

[67] V. Ashitkov, A. Barabash, S. Belogurov et al., "Liquid argon ionization detector for double beta decay studies", arXiv:nucl-ex/0309001.

[68] ATLAS Collaboration, "Readiness of the ATLAS Liquid Argon Calorimeter for LHC Collisions", *Eur. Phys. J.C* **70** (2010) 723–753. doi:10.1140/epjc/s10052-010-1354-y.

[69] GERDA Collaboration, "Status of the GERDA experiment aimed to search for neutrinoless double beta decay of 76Ge", arXiv:0812.4194.

[70] D. Gastler, E. Kearns, A. Hime et al., "Measurement of scintillation efficiency for nuclear recoils in liquid argon", *Phys. Rev. C* **85** (2012) 065811. doi:10.1103/PhysRevC.85.065811.

[71] R. Acciarri, N. Canci, F. Cavanna et al., "Neutron to Gamma Pulse Shape Discrimination in Liquid Argon Detectors with High Quantum Efficiency Photomultiplier Tubes", *Physics Procedia* **37** (2012) 1113 – 1121. Proceedings of the 2nd International Conference on Technology and Instrumentation in Particle Physics (TIPP 2011). doi:10.1016/j.phpro.2012.03.732.

[72] L. Kaufmann, "Detector performance and background studies for the ArDM experiment.PhD thesis, ETH Zurich". 2008.

[73] M. Berger, J. Hubbell, S. Seltzer et al. NIST, PML, Radiation and Biomolecular Physics Division.

[74] A. Gedanken, J. Jortner, B. Raz et al., "Electronic Energy Transfer Phenomena in Rare Gases", *The Journal of Chemical Physics* **57** (1972) 3456–3469. doi:10.1063/1.1678779.

[75] A. Hitachi, T. Doke, and A. Mozumder, "Luminescence quenching in liquid argon under charged-particle impact: Relative scintillation yield at different linear energy transfers", *Phys. Rev. B* **46** (1992) 11463–11470. doi:10.1103/PhysRevB.46.11463.

[76] A. Hitachi, T. Takahashi, N. Funayama et al., "Effect of ionization density on the time dependence of luminescence from liquid argon and xenon", *Phys. Rev. B* **27** (1983) 5279–5285. doi:10.1103/PhysRevB.27.5279.

[77] J. Lindhard, V. Nielsen, M. Scharff et al., "Integral equations governing radiation effects", *Mat. Fys. Medd. Dan. Vid. Selsk.* **33** (1963), no. 10, 1–42.

[78] EDELWEISS Collaboration, "Measurement of the response of heat-and-ionization germanium detectors to nuclear recoils", *Nucl.Instrum.Meth.* **A577** (2007) 558–568, arXiv:astro-ph/0607502. doi:10.1016/j.nima.2007.04.118.

[79] A. Bogaerts and R. Gijbels, "Modeling of metastable argon atoms in a direct-current glow discharge", *Phys. Rev. A* **52** (1995) 3743–3751. doi:10.1103/PhysRevA.52.3743.

[80] J. Keto, R. G. Jr., T. Bonifield et al., "Collisional mixing of the lowest bound molecular states in xenon and argon", *Chemical Physics Letters* **42** (1976) 125 – 128. doi:10.1016/0009-2614(76)80566-0.

[81] J. Lindhard, M. Scharff, and H. Schiott, "Range concepts and heavy ion ranges", *Mat. Fys. Medd. Dan. Vid. Selsk.* **33** (1963), no. 14, 1–42.

[82] J. Lewin and P. Smith, "Review of mathematics, numerical factors, and corrections for dark matter experiments based on elastic nuclear recoil", *Astroparticle Physics* **6** (1996) 87 – 112. doi:10.1016/S0927-6505(96)00047-3.

[83] J. A. LaVerne, A. Hitachi, J. J. Kolata et al., "Scintillation and ionization in allene-doped liquid argon irradiated with ^{18}O and ^{36}Ar ions of 30 MeV/u", *Phys. Rev. B* **54** (1996) 15724–15729. doi:10.1103/PhysRevB.54.15724.

[84] T. Doke, H. J. Crawford, C. R. Gruhn et al., "Scintillation yields by relativistic heavy ions and the relation between ionization and scintillation in liquid argon", *Nuclear Instruments and Methods in Physics Research Section A: Accelerators, Spectrometers, Detectors and Associated Equipment* **235** (1985) 136 – 141. doi:10.1016/0168-9002(85)90254-2.

[85] S. Himi, T. Takahashi, J. zhi Ruan(Gen) et al., "Liquid and solid argon, and nitrogen-doped liquid and solid argon scintillators", *Nuclear Instruments and Methods in Physics Research* **203** (1982) 153 – 157. doi:10.1016/0167-5087(82)90623-8.

[86] WArP Collaboration, "Effects of Nitrogen contamination in liquid Argon", *JINST* **5** (2010) P06003, arXiv:0804.1217. doi:10.1088/1748-0221/5/06/P06003.

[87] WArP Collaboration, "Oxygen contamination in liquid Argon: Combined effects on ionization electron charge and scintillation light", *JINST* **5** (2010) P05003, arXiv:0804.1222. doi:10.1088/1748-0221/5/05/P05003.

[88] R. Acciarri, M. Antonello, B. Baibussinov et al., "Effects of Nitrogen and Oxygen contamination in liquid Argon", *Nuclear Physics B - Proceedings Supplements* **197** (2009) 70 – 73. 11th Topical Seminar on Innovative Particle and Radiation Detectors (IPRD08). doi:10.1016/j.nuclphysbps.2009.10.037.

[89] D.-M. Mei, Z.-B. Yin, L. Stonehill et al., "A Model of Nuclear Recoil Scintillation Efficiency in Noble Liquids", *Astropart.Phys.* **30** (2008) 12–17, arXiv:0712.2470. doi:10.1016/j.astropartphys.2008.06.001.

[90] A. Manalaysay, "Towards an improved understanding of the relative scintillation efficiency of nuclear recoils in liquid xenon", arXiv:1007.3746.

[91] G. Plante, E. Aprile, R. Budnik et al., "New Measurement of the Scintillation Efficiency of Low-Energy Nuclear Recoils in Liquid Xenon", *Phys.Rev.* **C84** (2011) 045805, arXiv:1104.2587. doi:10.1103/PhysRevC.84.045805.

[92] R. Brunetti, E. Calligarich, M. Cambiaghi et al., "WARP liquid argon detector for dark matter survey", *New Astronomy Reviews* **49** (2005) 265 – 269. Sources and Detection of Dark Matter and Dark Energy in the Universe. 6th UCLA Symposium on Sources and Detection of Dark Matter and Dark Energy in the Universe. doi:10.1016/j.newar.2005.01.017.

[93] W. H. Lippincott, K. J. Coakley, D. Gastler et al., "Scintillation time dependence and pulse shape discrimination in liquid argon", *Phys. Rev. C* **78** (2008) 035801. doi:10.1103/PhysRevC.78.035801.

[94] L. Bollinger and G. Thomas, "Measurement of the Time Dependence of Scintillation Intensity by a Delayed?Coincidence Method", *Rev.Sci.Instrument* **32** (1961) 1044. doi:10.1063/1.1717610.

[95] P. Schotanus, "Recent developments in neutron detection with scintillators : some new data on liquid scintillators for neutron / gamma discrimination",. SCIONIX Holland B.V. Dedicated Scintilllation Detectors,Neutron workshop CIEMAT July 13-14 2006.

[96] G. F. Knoll, "Radiation detection and measurement". John Wiley & Sons Inc, 2000.

[97] J. Hopkins and G. Breit, "The 1H(n,n)1H scattering observables required for high-precision fast-neutron measurements", *Atomic Data and Nuclear Data Tables* **9** (1971) 137 – 145. doi:10.1016/S0092-640X(71)80038-4.

[98] National Nuclear Data Center (NNDC).

[99] R. L. Hirsch, "Inertial-Electrostatic Confinement of Ionized Fusion Gases", *J. Appl. Phys.* **38** 4522. doi:10.1063/1.1709162.

[100] J. Sved, "Neutron Generator System Design Report for CERN". 2008. NSDFusion Tech. Note NSD188 Issue 1 Version B 7122008.

[101] B. Technologies, "Neutron Probe LB 6411 for Measurement of the Ambient Dose Equivalent for Neutrons". 2007. 06-2007. 1000. ld. 82042PR2. Rev. 02 . 06-2007.

[102] C. Regenfus, C. Amsler, V. Boccone et al., "Operation of a DD-fusion neutron generator in building 15 R-018 for detector R&D in the ArDM project (RE18)".

[103] E. Brannen and G. L. Olde, "The Response of Organic Scintillators to Electron Energy Deposited in Them", *Radiation Research* **16** (1962) 1–6. doi:10.2307/3571123.

[104] V. Verbinski, W. Burrus, T. Love et al., "Calibration of an organic scintillator for neutron spectrometry", *Nuclear Instruments and Methods* **65** (1968) 8 – 25. doi:10.1016/0029-554X(68)90003-7.

[105] A. Naqvi, H. Al-Juwair, and K. Gul, "Energy resolution tests of 125 mm diameter cylindrical NE213 detector using monoenergetic gamma rays", *Nuclear Instruments and Methods in Physics Research Section A: Accelerators, Spectrometers, Detectors and Associated Equipment* **306** (1991) 267 – 271. doi:10.1016/0168-9002(91)90331-J.

[106] N. Hawkes, J. Adams, D. Bond et al., "Measurements of the proton light output function of the organic liquid scintillator NE213 in several detectors", *Nuclear Instruments and Methods in Physics Research Section A: Accelerators, Spectrometers, Detectors and Associated Equipment* **476** (2002) 190 – 194. Int. Workshop on Neutron Field Spectrometry in Science, Technolog y and Radiation ProtectioN. doi:10.1016/S0168-9002(01)01429-2.

[107] G. Dietze, "Energy calibration of NE-213 scintillation counters by γ-rays", *Nuclear Science, IEEE Transactions on* **26** (1979) 398–402. doi:10.1109/TNS.1979.4329665.

[108] G. Dietze and H. Klein, "Gamma-calibration of NE 213 scintillation counters", *Nuclear Instruments and Methods in Physics Research* **193** (1982) 549 – 556. doi:10.1016/0029-554X(82)90249-X.

[109] H. Schölermann and H. Klein, "Optimizing the energy resolution of scintillation counters at high energies", *Nuclear Instruments and Methods* **169** (1980) 25 – 31. doi:10.1016/0029-554X(80)90097-X.

[110] A. Naqvi, F. Z. Khiari, A. Coban et al., "Pulse height resolution of organic scintillators for monoenergetic gamma rays", in *Nuclear Science Symposium and Medical Imaging Conference, 1992., Conference Record of the 1992 IEEE*, pp. 4–6 vol.1. 1992. doi:10.1109/NSSMIC.1992.301166.

[111] M. Flaska and S. Pozzi, "Offline Pulse-Shape Discrimination Algorithms for Neutron Spectrum Unfolding", in *Nuclear Science Symposium Conference Record, 2006. IEEE*, volume 2, pp. 752–758. 2006. doi:10.1109/NSSMIC.2006.355962.

[112] J. Hong, W. Craig, P. Graham et al., "The scintillation efficiency of carbon and hydrogen recoils in an organic liquid scintillator for dark matter searches", *Astroparticle Physics* **16** (2002) 333 – 338. doi:10.1016/S0927-6505(01)00114-1.

[113] ArDM collaboration, "Development of wavelength shifter coated reflectors for the ArDM argon dark matter detector", *Journal of Instrumentation* **4** (2009) P06001.

[114] International Atomic Energy Agency, Nuclear data section.

[115] Sumitomo Cryogenics of America,INC. F-70H and F-70L Helium Compressors Operating Manual available from http://www.coldedgetech.com/uploads/files/267472A%20F-70%20Operating%20Manual%20Rev02.pdf.

[116] Technical data sheet Point-of-use Purifier OXISORB available from http://www.messergroup.com.

[117] ArDM Collaboration, "Towards a ton scale LAr WIMP detector", (2010) 130–134. Proceedings of the 6th Patras Workshop on Axions, WIMPs and WISPs. doi:10.3204/DESY-PROC-2010-03/regenfus_christian.

[118] MPD-4 data sheet V2.12 available from http://www.mesytec.com/datasheets/MPD-4.pdf.

[119] http://root.cern.ch.

[120] E. Bellamy, G. Bellettini, J. Budagov et al., "Absolute calibration and monitoring of a spectrometric channel using a photomultiplier", *Nuclear Instruments and Methods in Physics Research Section A: Accelerators, Spectrometers, Detectors and Associated Equipment* **339** (1994) 468 – 476. doi:http://dx.doi.org/10.1016/0168-9002(94)90183-X.

[121] http://www.srim.org,
http://physics.nist.gov/PhysRefData/Star/Text/ASTAR.html , ... /ESTAR.html.

[122] C. Regenfus, Y. Allkofer, C. Amsler et al., "Study of nuclear recoils in liquid argon with monoenergetic neutrons", *J.Phys.Conf.Ser.* **375** (2012) 012019, arXiv:1203.0849. doi:10.1088/1742-6596/375/1/012019.

[123] KATRIN Collaboration, "The KATRIN Experiment", *J.Phys.Conf.Ser.* **203** (2010) 012097, arXiv:0910.4862. doi:10.1088/1742-6596/203/1/012097.

[124] S.-C. WU, "Nuclear Data Sheets for A = 83", *Nuclear Data Sheets* **92** (2001) 893 – 1028. doi:10.1006/ndsh.2001.0010.

[125] C. Amsler, V. Boccone, A. Büchler et al., "Luminescence quenching of the triplet excimer state by air traces in gaseous argon", *Journal of Instrumentation* **3** (2008) P02001.

[126] J. Collar, "A Realistic Assessment of the Sensitivity of XENON10 and XENON100 to Light-Mass WIMPs", arXiv:1106.0653.

[127] G. Plante and E. Aprile, "The XENON100 Dark Matter Experiment: Design, Construction, Calibration and 2010 Search Results with Improved Measurement of the Scintillation Response of Liquid Xenon to Low-Energy Nuclear Recoils". PhD thesis, Columbia U., Columbia, 2012.

[128] F. Bezrukov, F. Kahlhoefer, M. Lindner et al., "Interplay between scintillation and ionization in liquid xenon Dark Matter searches", *Astropart.Phys.* **35** (2011) 119–127, arXiv:1011.3990. doi:10.1016/j.astropartphys.2011.06.008.

[129] M. Szydagis, N. Barry, K. Kazkaz et al., "NEST: A Comprehensive Model for Scintillation Yield in Liquid Xenon", arXiv:1106.1613.

Acknowledgments

First of all, I would like to thank to Prof. Dr. Claude Amsler for giving me the wonderful opportunity to do my PhD work in his group based at CERN and for his guidance during my four years of study.

I am very thankful to Dr. Christian Regenfus for his supervision, advices and patience. I have learned so much from him and his precious knowledge helped me to get a broad view of experimental physics. I am grateful as well to Dr. Vittorio Boccone, who introduced the R&D life in the laboratory at the beginning of my PhD and who clearly explained the principle of light detection in ArDM. Many thanks to Dr. Polina Otiougova for her useful radiation dose calculation in our laboratory. I would like to express my gratitude to Dr. Alfredo Davide Ferella for his support and development of the Monte Carlo simulation. I promise I will not tight the rope when I'm leading during climbing (also in life).

Thanks also to Dr. Yves Allkofer for the theoretical discussion on the model of the scintillation yield in liquid argon and for sharing his experience on data analysis, and to Jacky Rochet for introducing me to the cryogenic and the vacuum technology. His big effort in the workshop was very useful for the mechanical part of the experiment and I do not forget his philosophy which helped me to learn how to see the bright side of scientific life. Many thanks to Dr. Luca Scotto Lavina for being a great help on the development of the data analysis software and for his outstanding programming skill which changed my way to approach this painful language called C/C++. Thanks to the rest of the group for making the daily life easier and funnier. I appreciated the fact I could "squat" your office during the break time and I'm glad you could squat my office in return.

Special acknowledgements to my family for its support and encouragement during difficult moments. Thanks to my friends for sharing a part of my life with me in Geneva; I do not forget the italian community, especially "MarcAntonio" and, the e-mails translated from Italian to Italian by Cristina, and of course the climbing team with our usual PanDay.